TECHNISCHE UNIVERSITÄT WIEN
Vienna University of Technology

UNIVERSITÉ PARIS SUD

université PARIS-SACLAY

Dissertation

Ordered equilibrium structures in systems with long-range interactions

Ausgeführt zum Zwecke der Erlangung des akademischen Grades eines Doktors der technischen Wissenschaften unter der Leitung von

Univ. Prof. Dr. Gerhard Kahl
Institut für Theoretische Physik (E136)
Technische Universität Wien

und

Prof. Agrégé Dr. Martial Mazars
Laboratoire de Physique Théorique (UMR 8626)
Université Paris-Sud, Orsay

eingereicht an der Technischen Universität Wien
Fakultät für Physik

von

Moritz Antlanger
Matrikelnummer 0625685
Tigergasse 8/16, 1080 Wien

Wien, im September 2015

_____
Moritz Antlanger

This thesis was carried out in joint supervision between the

Technische Universität Wien

and the

Université Paris-Sud

as part of a *cotutelle de thèse*. To comply with regulations from both sides, a second title page has been added on the following page.

Thèse de doctorat

Soutenue le 12/10/2015 par

Moritz ANTLANGER

Structures ordonnées dans les systèmes avec des interactions á longue portée

Kurzfassung

Sogenannte *Metamaterialien* bieten einen vielversprechenden Ansatz für die Herstellung von neuartigen funktionalen Materialien. Das ihnen zugrundeliegende Konzept besagt, dass die Eigenschaften eines Materials in gewissen Fällen stärker von der geometrischen Anordnung seiner Bestandteile abhängen als von deren Beschaffenheit. Solche wohlgeordneten Teilchenstrukturen können sich wie akustische, elastische, oder elektromagnetische Wellenleiter verhalten, was eine Vielzahl von interessanten Anwendungen ermöglicht. Das zentrale Problem der Herstellung dieser Strukturen, beispielsweise durch *self-assembly*, ist in den letzten Jahren auf reges experimentelles und theoretisches Interesse gestoßen.

Die Wechselwirkungen zwischen Teilchen werden in theoretischen Studien durch Potentialfunktionen ausgedrückt, deren Form einen erheblichen Einfluss auf die gebildeten Strukturen hat. Häufig werden hierfür Potentiale verwendet, die mit dem Abstand schnell abfallen. In dieser Dissertation beschäftigen wir uns mit sogenannten *langreichweitigen* Wechselwirkungen, bei denen Teilchen über viele mittlere Teilchenabstände miteinander wechselwirken. Typische Beispiele für solche Potentiale sind Wechselwirkungen zwischen elektrischen Ladungen oder Multipolen. Unsere Vorgangsweise besteht zunächst darin, die Grundzustandsstruktur des Systems bei verschwindender Temperatur zu studieren, indem wir das relevante thermodynamische Potential – in diesem Fall die Energie – minimieren. Wir beobachten eine Vielzahl von Strukturen und neuartige Szenarien für Phasenübergänge. In einem weiteren Schritt verwenden wir Monte Carlo-Simulationen, um die Stabilität dieser Strukturen bei niedrigen Temperaturen zu untersuchen.

Abstract

The central paradigm in the emerging field of *metamaterials* is that the properties of a material are in certain cases governed rather by the well-ordered spatial arrangement of its constituent particles than by the properties of those particles themselves. Since such highly ordered patterns can act as waveguides for acoustic, elastic, or electromagnetic waves, they can give rise to novel material properties, opening up new avenues in materials design. The central problem of how to produce the required ordered particle arrangements, e.g., via self-assembly, has received significant attention both from the experimental and theoretical sides.

In theoretical studies, the interactions between particles are modeled via potential functions, whose shape and range have a profound impact on the formed structures. These potentials are often short-ranged, i.e., they are characterized by a rapid decay with distance. In this thesis, we focus on systems featuring *long-range* interactions, where particles interact over significantly larger distances than the mean inter-particle separation. Typical examples for such potentials are charged or multipolar interactions.

In our approach, we first determine the ordered structures formed by the particles at vanishing temperature by minimizing the relevant thermodynamic potential. We observe a surprising plethora of different structural archetypes as well as novel phase transition scenarios. Then, we investigate the stability of these structures at low temperatures using Monte Carlo simulations.

Résumé

L'un des concepts fondamentaux dans l'étude des *métamatériaux* est que, dans certains cas, les propriétés du milieu sont déterminés par l'arrangement structurel de ses composants plutôt que par les propriétés intrinsèques des particules. De telles structures hautement ordonnées peuvent servir de guide d'onde en acoustique, ainsi que pour des ondes élastiques ou électromagnétiques ; elles peuvent aussi induire de nouvelles propriétés, ouvrant ainsi de nouvelles perspectives dans la conception des matériaux. Dans ce champ de recherche, la question centrale est de trouver comment produire ces arrangements ordonnés de particules et de molécules ; par exemple, un grand nombre d'études expérimentales et théoriques s'appuient sur des mécanismes d'auto-assemblage.

Dans les études théoriques, ainsi que dans les simulations numériques, les interactions entre les constituants sont déterminées par des potentiels modèles ou effectifs dont la portée et la forme déterminent les structures collectives. Les potentiels utilisés sont souvent à courte portée, c'est-à-dire qu'ils ont une décroissance très rapide avec la distance ; typiquement, des molécules séparées de quelques diamètres moléculaires n'interagissent pas directement. Dans cette thèse, nous nous intéressons à ces structures ordonnées qu'il est possible d'obtenir, non pas avec des interactions à courte portée, mais avec des interactions à très longue portée (Coulomb, etc.).

Notre démarche consiste dans un premier temps à déterminer les structures optimales à température nulle (états fondamentaux) en minimisant le potentiel thermodynamique adéquat ; puis, nous étudions la stabilité thermique de ces structures à basse température à l'aide de simulations numériques de Monte-Carlo. Nous observons une pléthore de structures prototypes, ainsi que des transitions de phases entre elles.

Contents

1. Introduction

In recent years, materials design has attracted a considerable amount of attention. As suggested by its name, the focus in this field lies in designing materials with unconventional desired properties. A few examples for such properties are self-healing materials [1], which can repair damage over time, or photonic crystals [2, 3], which have unusual optical properties useful in a variety of applications.

Photonic crystals are part of the wider category known as *metamaterials* [4], which – although manufactured from conventional materials – exhibit novel properties due to their highly ordered structure. Metamaterials act as waveguides for acoustic [5], elastic [6], or electromagnetic waves; features on length-scales smaller than the wavelength result in unconventional or even exotic properties. Particularly illustrative examples are given by materials with negative refractive index [7] and by a proposed design for a metamaterial acting as a black hole for microwave radiation [8].

Especially for optical metamaterials – such as the photonic crystals mentioned above – the length-scale of interesting features ranges in the meso-scale, i.e., $\sim 100 - 1000$ nm. The traditional approach for synthesizing materials with features of this size is the *top-down* approach, i.e., controlling parameters on a *larger* length-scale; this can be done, e.g., with lithographic processes.

In the past few years, a diametrically different strategy – the so-called *bottom-up* approach – has gained rapidly increasing significance; in this approach, particles in a system that at first is disordered assemble into a well-ordered structure without any external guidance. This assembly process is thus governed by the interactions of particles with each other. The main challenge in this approach then lies in designing adequate "building blocks" that will self-assembly into a specific structure. Many different systems exhibit such a self-assembling behavior. In the following, we give just a few examples:

- A very elegant way of producing self-assembling particles is to exploit the selective binding mechanism of DNA-strands. By suitably designing a sequence of bases, strands self-assemble into complex structures such as scaffolds [9]. DNA can also be used to decorate the surface of colloids, making them self-assemble into a target lattice [10].
- Strongly directional interactions between particles are also found in anorganic systems. An example are so-called patchy particles [11–13], where the surface of colloids is decorated in such a way as to form attractive patches. Depending on the location of patches on the colloidal surface, particles then self-assemble into different lattices.
- Another example are magnetic particles, e.g., iron nanoparticles [14]. These are able to form intricate chain- and ring-like structures [15–18]. In addition to this self-assembling behavior, some properties of the particles can be tuned by applying an external magnetic

field, allowing for a guided formation of complex structures [19].

Some of the experimental systems listed above have also been studied extensively in simulations. The interaction potentials used in studies on DNA-functionalized particles [10], patchy particles [13, 20, 21], and magnetic particles [22–26] are often simplified – not only to make them computationally manageable, but also to gain further insight in the processes causing and governing self-assembly.

Self-assembly can also be observed in systems that are proposed in the literature and that are not directly related to experiments. In the following, we will list some examples of such systems:

- A very simple system forming intricate structures are particles interacting via the square-shoulder potential [27], which consists of a hard core and a soft shell. Depending on the ratio between core- and shell-diameter, a multitude of structures – and even cases of quasicrystals – have been observed [28, 29].
- Other theoretical studies have focussed more on optimizing the potential such that particles self-assemble into a desired structure [30, 31].
- Another interesting approach is based on the packing of hard polyhedra [32]; depending on the shape of the particles, a large variety of different structures can be observed.

A characteristic feature shared between many of the potentials employed in these theoretical studies are their anisotropy and their relatively short (spatial) range, i.e., particles only interact with other particles in their close proximity.

In this work, we focus on the formation of ordered structures in systems featuring *long-range* interactions, where particles interact over large distances, extending far beyond nearest-neighbor distances. As particle arrangements beyond nearest neighbors gain importance, such interactions may result in interesting lattices. Long-range interactions, as they typically occur between charged or dipolar particles, are very common in nature: charged systems such as dusty plasmas [33, 34] are not only important in astrophysics [35], but also for industrial applications. Examples for dipolar systems are given by magnetic nanoparticles [36] and even peculiarities such as magnetotactic bacteria [37].

In fact, almost all particles in experimental systems feature an internal charge distribution, which can be expanded in terms of multipole moments: the higher the order of the multipole, the shorter the range of the interaction.

In the following, we will give a short overview of commonly studied models that carry multipole moments, featuring terms up to the second order:

- The monopole term specifies the interaction between the net charges of particles. In three dimensions, this interaction is given by the Coulomb potential, which is proportional to the inverse distance between the particles.
  The simplest model featuring the Coulomb interaction is the *one-component plasma* (OCP) [38–40], which consists of a set of point charges immersed in a uniform neutralizing back-

ground. This system can be described by a single coupling constant Γ and crystallizes – for sufficiently strong coupling – in the BCC lattice [41].

Another common charged model is the *restricted primitive model of electrolytes* (RPM) [42, 43], where charges are embedded in hard spheres, preventing them from approaching too close to each other.

- The dipole term is anisotropic and decays as $\sim r^{-3}$, r being the distance between the particles.

  The simplest model featuring dipolar interactions is the *dipolar hard sphere* (DHS) model [22, 44, 45], where point dipole moments are embedded in hard spheres. At low densities, these particles form (branched) chains or rings.

  In recent years, a variation of the DHS model has also received a significant amount of attention, where the point dipole moment is shifted slightly from the center of the sphere [46, 47]. Apart from the structural mechnisms observed in the DHS model, more complicated cluster geometries have been observed.

  Another common model is the *Stockmayer potential* [48], where point dipole moments are embedded in spheres interacting via the Lennard-Jones potential; it is repulsive at short distances and attractive at intermediate distances. This system crystallizes for sufficiently low temperature in either the body-centered orthorhombic (BCO) lattice, the body-centered tetragonal (BCT) lattice, or a hexagonally close-packed (HCP) lattice [49].

- The quadrupole term is anisotropic and decays as $\sim r^{-5}$. It is common to study special cases of quadrupole moments, such as *linear* or *square* quadrupoles [50], where the two inverted dipoles making up the quadrupole are aligned head-to-head or side-by-side, respectively. An additional short-range repulsive potential, e.g., the Lennard-Jones-type potential, is necessary to prevent point quadrupole moments from overlapping.

In this work, we will search for ordered equilibrium structures in systems featuring some of the interactions described above. In the following, we outline our general strategy for identifying equilibrium structures. The particular models studied in this work will be discussed later.

A given system is governed by the related thermodynamic potential, which assumes its minimum value when the system is in equilibrium. For a system under NVT-conditions (where particle number N, volume V, and temperature T are kept constant), the relevant thermodynamic potential, i.e., the Helmholtz free energy F, is given by

$$F(N, V, T) \;=\; E - TS, \tag{1.1}$$

where E is the energy and S is the entropy. Under NPT-conditions (where N, external pressure P, and T are kept constant), the relevant thermodynamic potential is the Gibbs free energy

$$G(N, P, T) \;=\; E + PV - TS. \tag{1.2}$$

While the energy E can be computed analytically with high accuracy, the entropy S can

only be obtained with more elaborate (and less accurate) approaches such as thermodynamic integration [51].

Our approach for finding ordered equilibrium structures is based on two steps:

(i) We first study the systems at vanishing temperature, where the free energy reduces to the energy E or to the enthalpy $H = E + PV$, respectively, thereby avoiding the calculation of the entropy, which is required at finite temperature. Still, obtaining the configurations with the lowest energy or enthalpy is not trivial either, as it represents a global minimization problem in a high-dimensional search space.

In order to solve this global minimization problem, we present and employ an optimization tool based on ideas of evolutionary algorithms (EAs).

Often, knowledge of the ground state configurations is of importance as it can give an overview of relevant regions in the parameter space; the set of observed configurations can also help with the construction of phase diagrams [52].

(ii) In the second step of our investigations we perform simulations at low temperature in order to study the mechanical and thermodynamic stability of the obtained structures. Here, we use either Monte Carlo (MC) or Molecular Dynamics (MD) simulations.

The structures observed at $T = 0$ are not only useful for initializing simulations carried out at finite temperature, but can also serve as reference points for the interpretation of snapshots and order parameters, i.e., comparison to the defect-free ground state can help us understand the underlying structure at finite temperature. For methods trying to directly calculate the free energy, e.g., the multi-histogram reweighting approach [53, 54], having an independent reference value for the energy can also be very useful.

In addition, having an independent reference value can be very useful for methods trying to directly calculate the free energy, e.g., the Multi-Histogram Reweighting approach [53, 54].

In this work, we will investigate four different systems featuring long-range interactions:

(i) The first system is based on classical point charges confined to a planar geometry. These charges interact via the $1/r$-Coulomb potential; electro-neutrality is guaranteed via a uniform, planar, neutralizing background. We will investigate an equimolar binary mixture of charges of the same sign, leading to non-trivial particle arrangements.

(ii) For the second system, we will investigate how a monolayer system of charges interacting via the Coulomb potential transforms into a dilute bilayer; electro-neutrality is again guaranteed via a uniform, planar, neutralizing background. We will study the structural changes the particle arrangement in the remaining monolayer undergoes as a single charge is vertically displaced.

(iii) The third system is based on classical point charges in a bilayer geometry. In the simplest case, the neutralizing background is the same for both layers and the formed structure depends solely on the distance separating the two plates. We will then study the effects of introducing an asymmetry in the background charges – making the background on one plate stronger than on the other – on the particle arrangements in both layers. The interplay of the separation distance between the plates and the charge asymmetry between the neutralizing background densities results in a remarkably complex phase diagram.

(iv) For the fourth system, we will investigate a system of ellipsoidal particles with an embedded linear quadrupole moment [1]. The ellipsoidal shape of the particles is modelled via a soft repulsive potential with short spatial range. The formed structures are governed by the competition between the relatively long-range and the short-range interactions.

This work is organized as follows:

- In **Chapter 2**, we give an overview of the methods we use in this work.
- In **Chapter 3**, we present the different systems studied in this thesis: once each system has been introduced, we develop a suitable theoretical model and define quantities that can help us characterize the properties of the system. We then present and interpret the obtained results.
- In **Chapter 4**, we conclude and provide an outlook on possible future investigations.
- Supplementary information is given in **Appendix A**.

---

[1]. A *linear* quadrupole moment is a special case wherein two dipole moments of opposite orientation are superimposed such that their positive "charges" overlap.

2. Methods

In this chapter, we present the methods used to obtain the results presented in the subsequent chapter. We first discuss issues with the calculation of the potential energy arising from the long-ranged nature of the interactions (see Section 2.1). Then, we focus on the two main components of our approach presented in the preceding section:

(i) We are first interested in obtaining the ground state configuration for a given system; we thus have to globally minimize its energy at vanishing temperature (see Section 2.2).

(ii) In a second step, we perform Monte Carlo simulations at low temperatures (see Section 2.3) to verify the results obtained at zero temperature.

We then proceed to the presentation of supplementary methods that help us in obtaining further information on the system. We start with an overview of bond-orientational order parameters that can be used to quantify and classify ordered structures (see Section 2.4); we also provide some details on how these quantities can be calculated accurately. Finally, we also present the nudged elastic band method (see Section 2.5), i.e., an approach to studying transition paths in rugged energy landscapes.

2.1. Long-range interactions: Ewald summation

In this section, we specify the term "long-ranged interactions" and discuss what difficulties they entail (see Subsections 2.1.1 and 2.1.2). We then proceed to present the formalism of Ewald summation (see Subsection 2.1.3), which allows us to accurately and efficiently calculate the potential energy of long-ranged systems. In an effort to provide a better understanding of this method, we derive its basic expressions for the simple system of Coulomb interactions in two dimensions. In addition, we discuss important aspects of the implementation of Ewald sums and their convergence (see Subsection 2.1.4).

2.1.1. Long-ranged interactions: definition and problems

When calculating the potential energy of a system in computational physics, we always have to carefully put into relation expectations in numerical accuracy, computational cost, and difficulties related to the implementation of the method. Often, interactions between particles decay rather quickly with increasing distance, i.e., particles either do not interact with distant particles, or these interactions are negligible compared to those between close-by particles.

In the following we study the interaction energy of a particle (located at the origin) with $(N-1)$ other particles in a macroscopic volume V. The number particle density is given by

$$\rho(\boldsymbol{r}) \;=\; \delta(\boldsymbol{r}) + \sum_{i=2}^{N} \delta(\boldsymbol{r} - \boldsymbol{r}_i), \tag{2.1}$$

where $\boldsymbol{r}_i$ denotes the position of particle i. Particles i and j interact with a potential $V(\boldsymbol{r}_i - \boldsymbol{r}_j)$, thus the energy of the entire system is given by

$$
\begin{aligned}
E \;&=\; \frac{1}{2} \int_V d\boldsymbol{r} \int_V d\boldsymbol{r}' \rho(\boldsymbol{r}) V(\boldsymbol{r}-\boldsymbol{r}') \rho(\boldsymbol{r}') \\
&=\; \frac{1}{2} \int_V d\boldsymbol{r} \int_V d\boldsymbol{r}' \left[\delta(\boldsymbol{r}) + \sum_{i=2}^{N} \delta(\boldsymbol{r}-\boldsymbol{r}_i) \right] V(\boldsymbol{r}-\boldsymbol{r}') \left[\delta(\boldsymbol{r}') + \sum_{j=2}^{N} \delta(\boldsymbol{r}'-\boldsymbol{r}_j) \right].
\end{aligned} \tag{2.2}
$$

The integrals are carried out over the macroscopic volume of the sample.

The expression for the energy can be split into three contributions. We are at the moment only interested in the interaction of particle 1 with the other particles. We obtain this interaction by considering the terms $(i=1, j \neq 1)$ and $(i \neq 1, j=1)$

$$E_1 \;=\; \frac{2}{2} \int_V d\boldsymbol{r} \int_V d\boldsymbol{r}' \sum_{i=2}^{N} \delta(\boldsymbol{r}-\boldsymbol{r}_i) V(\boldsymbol{r}-\boldsymbol{r}') \delta(\boldsymbol{r}'). \tag{2.3}$$

We disregard the self-interaction obtained for $i=j$

$$E_{\text{self}} \;=\; \frac{1}{2} \int_V d\boldsymbol{r} \int_V d\boldsymbol{r}' \sum_{i=1}^{N} \delta(\boldsymbol{r}-\boldsymbol{r}_i) V(\boldsymbol{r}-\boldsymbol{r}') \delta(\boldsymbol{r}'-\boldsymbol{r}_i) \tag{2.4}$$

and the interactions of the other particles with each other

$$E_{\text{other}} \;=\; \frac{1}{2} \int_V d\boldsymbol{r} \int_V d\boldsymbol{r}' \sum_{i=2}^{N} \delta(\boldsymbol{r}-\boldsymbol{r}_i) V(\boldsymbol{r}-\boldsymbol{r}') \sum_{j=2}^{N} \delta(\boldsymbol{r}'-\boldsymbol{r}_j). \tag{2.5}$$

We carry out the integration over $\boldsymbol{r}'$ for the first term of E_1 in Equation 2.3 and obtain

$$E_1 \;=\; \int_V d\boldsymbol{r} \sum_{i=2}^{N} \delta(\boldsymbol{r}-\boldsymbol{r}_i) V(\boldsymbol{r}). \tag{2.6}$$

The volume in the integration (which we may consider equivalent to the sample size in experimental systems) may be *macroscopically* small, but can be considered *microscopically* large. The same is true for the number of particles N in the system, which is on the order of magnitude of the Avogadro constant $N_{\text{A}} \approx 6 \times 10^{23} \text{mol}^{-1}$. For computational purposes, we approximate the finite (macroscopic) system by an infinite system (characterized by a

microscopic unit cell), which we usually presume to be periodic. We justify this by the huge discrepancy between macroscopic sample size and microscopic distances between particles. For simplicity, we further assume an isotropic potential

$$V(\boldsymbol{r}) \quad = \quad V(r). \tag{2.7}$$

We can transform the integral in Equation 2.6 and obtain

$$E_1 \quad = \quad \int_0^\infty 4\pi r^2 dr \rho(r) V(r), \tag{2.8}$$

where we define the radial number particle density of the system $\rho(r)$ as

$$\begin{aligned} \rho(r) \quad &= \quad \frac{1}{4\pi r^2} \int_0^{2\pi} d\phi \int_0^\pi \sin\theta d\theta \rho(\boldsymbol{r}) \\ &= \quad \sum_{i=2}^N \frac{1}{4\pi r_i^2} \delta(r_i). \end{aligned} \tag{2.9}$$

In practice, the infinite integral in Equation 2.8 is numerically evaluated by including contributions only up to a certain cutoff radius R_{cut}

$$E_1 \quad \approx \quad \int_0^{R_{\text{cut}}} 4\pi r^2 dr \rho(r) V(r). \tag{2.10}$$

The above approximation causes a relative error δ in the energy evaluation, which we can estimate for a monotonic interaction potential via

$$\delta \quad = \quad \frac{\int_{R_{\text{cut}}}^\infty 4\pi r^2 \rho(r) V(r) dr}{\int_0^\infty 4\pi r^2 \rho(r) V(r) dr}. \tag{2.11}$$

If $V(r)$ decays sufficiently fast with distance, we can use this relation to fix R_{cut} such that we can achieve any desired accuracy δ. This is a common practice in computational physics.

Problems start to arise when $V(r)$ does not decay sufficiently quickly with distance; in this case the cutoff radius R_{cut} can become very large and the computational cost to calculate E_1 can be very high, making high-accuracy studies prohibitively time-consuming. This issue becomes a serious problem if the energy differences between competing structures are very small compared to the total interaction energy.

Finally, there are interactions where the above relations (see Equations 2.8 and 2.11) are no longer applicable, i.e., where the involved integrals do not converge. A simple example is the Coulomb interaction

$$V_{\text{Coulomb}}(r) \quad \sim \quad \frac{1}{r}. \tag{2.12}$$

This problem can also occur for inverse-power law (IPL) interactions with an exponent n

$$V_{\text{IPL}}(r) \quad \sim \quad \frac{1}{r^n}; \tag{2.13}$$

if the dimension of the system d fulfills the relation $n \leq d$, the interaction doesn't decay sufficiently fast for the potential energy to converge. Interactions with such a behavior at $r \to \infty$ are considered *long-ranged*. Apart from the non-convergence of the total interaction energy (see Equation 2.6), we also make an inestimable relative error when using a cutoff radius (see Equation 2.11).

2.1.2. Long-ranged interactions: background and boundary conditions

Returning to the example of Coulomb interactions introduced in Subsection 2.1.1, we know that basic laws of electrostatics suggest that an infinitely large system needs to be electroneutral as a whole, guaranteeing that the energy per particle is finite. For a system of point charges Q_i, this electro-neutrality can either be achieved via charges of opposite sign

$$\sum_i Q_i \quad = \quad 0, \tag{2.14}$$

or by adding a neutralizing background to the system, such that the total charge contained in the system is zero

$$\int_{\boldsymbol{r}} \sigma(\boldsymbol{r}) d\boldsymbol{r} + \sum_i Q_i \quad = \quad 0; \tag{2.15}$$

here, $\sigma(\boldsymbol{r})$ is a neutralizing background charge density, which may sometimes even be uniform. A similar concept can be applied to non-electrostatic interactions: we consider the particle "charge" density $\rho(\boldsymbol{r})$ a sum of delta peaks and the background "charge" density $\sigma(\boldsymbol{r})$ a continuous function.

The integral in the energy calculation (see Equation 2.6) is conditionally convergent as some of the terms depend on the chosen macroscopic boundary conditions [55–61], such as the shape of the sample and the surrounding medium (see Figure 2.1). Defining the macroscopic system alone is, however, still insufficient: only after adding a neutralizing background does the integral converge. Nevertheless, we still cannot calculate the system's energy by using a simple direct lattice sum.

At this points we want to emphasize that for dipolar systems, the properties of the medium surrounding the macroscopic system can have particularly illustrative effects: they can favor or suppress ferromagnetism [56, 60]. In addition, the macroscopic shape may also influence the energy calculation and proper treatment starting from the Maxwell equations would be necessary [62].
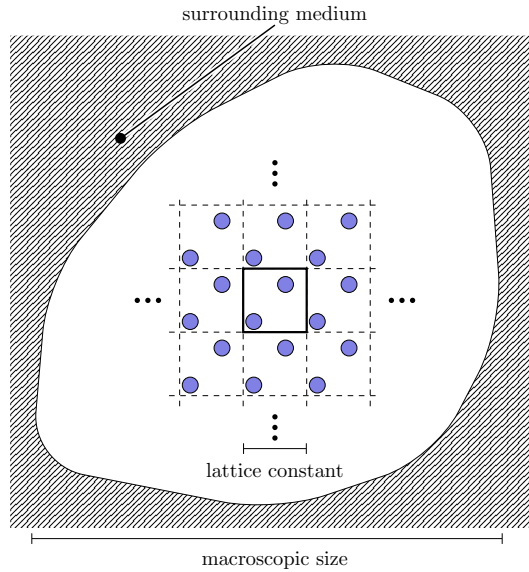
Figure 2.1.: Schematic view of the lattice constant of a crystal (related to its microscopic periodicity) and the macroscopic size of the sample. The two length scales are not drawn to size as they differ by many orders of magnitude. In systems with electrostatic interactions, the medium surrounding the macroscopic object and even the shape of the boundary may have a profound effect on the microscopic behavior.

In this work, we assume *metallic* boundary conditions, i.e., that the macroscopic system is surrounded by a medium with a dielectric constant $\epsilon_r = \infty$. This choice is useful as some energy terms introduced by the macroscopic boundary disappear [63][1].

2.1.3. Ewald summation: basic idea and derivation

We now turn our attention to the actual energy calculation of a system with long-ranged interactions. As mentioned in Subsection 2.1.2, we cannot calculate the energy per particle of such a system via a simple lattice sum. However, in order to cope with this problem, several mathematical methods have been proposed: among these are modified sums in real and reciprocal space, such as Ewald summations [65] and Lekner sums [66]; adaptations of these based on discretization and Fast Fourier Transforms have also been developed to efficiently deal with large systems, e.g., the particle-mesh Ewald method [67, 68] or the particle-particle-particle-mesh Ewald method [69–72]. Other approaches try to directly solve the Laplace equation on the surface of a hypersphere [73, 74]. Additional methods, such as the Nijboer-de Wette and the fast multipole approaches, are discussed in [75]. In this work, we exclusively use the method of Ewald summation.

---

1. The stress tensor, however, retains its dependence on the macroscopic sample shape even for metallic boundary conditions [64].

The formalism behind Ewald summation was originally developed for computing the Madelung constant in ionic systems [65, 76]. It can mathematically be described by the Poisson-Jacobi formula, which allows us to split an infinite real space summation into infinite summations in real and reciprocal space. It can be shown that both of these sums converge and do so quickly; we can thus calculate the system's potential energy. This procedure can be interpreted as splitting the interaction into a short-range part, computed in real space (see left panel of Figure 2.2), and a long-range part, computed in reciprocal space (see right panel of Figure 2.2). Small k-vectors in reciprocal space correspond to large distances in real space; the two sums are thus to some extent complementary.
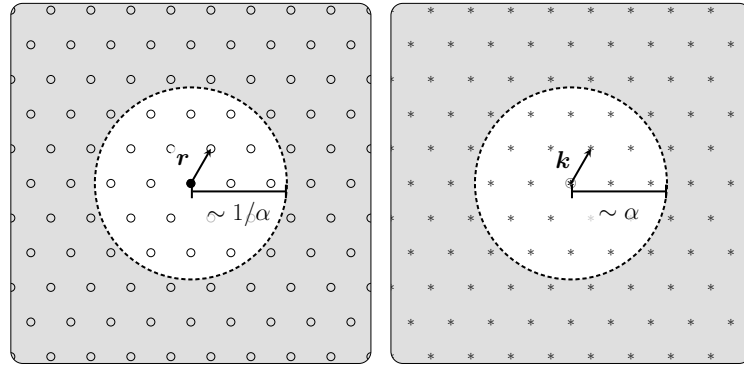

Figure 2.2.: Schematic view of the mathematical interpretation of Ewald summation. Left panel: summation in real space. Particle positions are indicated by circles. For long-ranged interactions, we are required to carry out the infinite sum in order to obtain an estimable accuracy. In the formalism of Ewald summation, the real space interaction decays at a length scale proportional to $\sim 1/\alpha$ (α being an arbitrary parameter of the summation introduced in Equation 2.22). This allows us to neglect terms for large distances (large r-vectors). If the minimum image convention is used, this cutoff should be on the order of the box size. For small cells, we need to sum over several periodic images. Right panel: summation in reciprocal space. Position of reciprocal lattice vectors is indicated by asterisks. The reciprocal space interaction decays at a length scale proportional to $\sim \alpha$. Small k-vectors correspond to large real space distances.

Some textbooks also offer an easily accessible physical interpretation of Ewald summation: first the interaction range in real space is reduced by adding a screening background of convenient shape; then the background is subtracted again (see Figure 2.3). The screened interaction is treated in real space while the background is subtracted in reciprocal space, where it is easily manageable due to its convenient shape.

We now present the mathematically rigorous derivation of the Ewald summation technique [75] based on the Poisson-Jacobi formula. For this, we choose a simple long-ranged system,
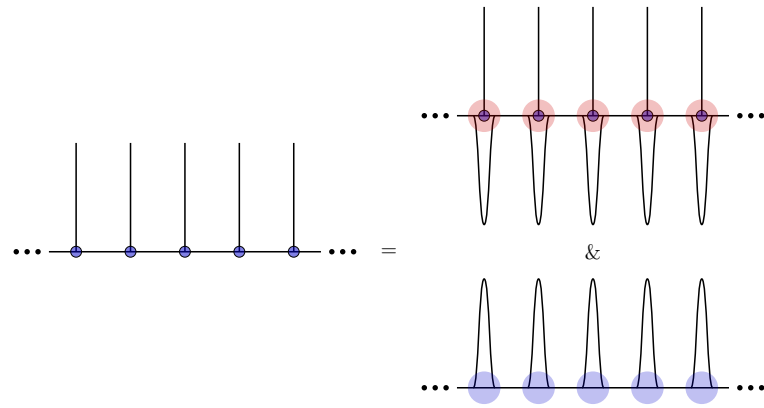
Figure 2.3.: Schematic view of the physical interpretation of Ewald summation used in some textbooks. Left panel: actual physical system, which consists of an infinite arrangement of point-like interaction sites, i.e., the distribution is delta-like. Right panel: introduction and consequent subtraction of a screening distribution, which makes the interaction manageable. The interactions in the top panel are calculated in real space while those in the bottom panel is treated in reciprocal space. This may be significantly easier to accomplish if the shape of the screening distribution is convenient, e.g., if its Fourier transform decays quickly with increasing k.

namely the $1/r$-Coulomb interaction in two dimensions[2] using a uniform neutralizing background. We note that the formalism is only defined for periodic systems. We thus assume that the system can be characterized by a unit cell containing N particles. The shape of the unit cell is defined by the lattice vectors $\boldsymbol{a}$ and $\boldsymbol{b}$, such that the origin of any of its periodic images is located at

$$\boldsymbol{R} \;=\; n_a\boldsymbol{a} + n_b\boldsymbol{b}, \tag{2.16}$$

where n_a and n_b are integers. We can write the interaction energy per particle as the sum of three terms, i.e., *particle-particle* ("pp"), *particle-background* ("pb"), and *background-background* ("bb"), leading to

$$\frac{E}{N} \;=\; \frac{1}{N}\left(E_{\mathrm{pp}} + E_{\mathrm{pb}} + E_{\mathrm{bb}}\right) \tag{2.17}$$

$$E_{\mathrm{pp}} \;=\; \frac{1}{2}\sum_{i=1}^{N}\sum_{j=1}^{N}\sum_{\boldsymbol{R}}{}' \frac{Q_iQ_j}{|\boldsymbol{r}_i - \boldsymbol{r}_j + \boldsymbol{R}|} \tag{2.18}$$

$$E_{\mathrm{pb}} \;=\; \sum_{i=1}^{N}\int_{L}\sum_{\boldsymbol{R}} \frac{Q_i\sigma(\boldsymbol{r})d\boldsymbol{r}}{|\boldsymbol{r}_i - \boldsymbol{r} + \boldsymbol{R}|} \tag{2.19}$$

$$E_{\mathrm{bb}} \;=\; \frac{1}{2}\sum_{\boldsymbol{R}}\int_{L}\int_{L} \frac{\sigma(\boldsymbol{r})\sigma(\boldsymbol{r}')d\boldsymbol{r}d\boldsymbol{r}'}{|\boldsymbol{r} - \boldsymbol{r}' + \boldsymbol{R}|}. \tag{2.20}$$

The primed sum indicates the omission of the term $i = j$ for $\boldsymbol{R} = 0$ and L indicates an integral over the entire unit cell.

We now use a mathematical identity to transform these terms, namely an integral representation of the Γ-function [77]

$$\frac{1}{r} \;=\; \frac{1}{\sqrt{\pi}}\int_{0}^{\infty}\frac{dt}{\sqrt{t}}\exp(-r^2 t). \tag{2.21}$$

---

2. Note that in a *truly* two-dimensional systems, point charges interact with a logarithmic potential $V_{\mathrm{2D}}(r) = \log(r)$, which is the solution to the two-dimensional Poisson equation. The system we assume is implicitly three-dimensional, though all charges are confined to the plane $z = 0$.

With this relation, we obtain

$$
\begin{aligned}
E_{\mathrm{pp}} &= \frac{1}{2\sqrt{\pi}} \sum_{i=1}^{N} Q_i \sum_{j=1}^{N} Q_j \sum_{\mathbf{R}}{}' \lim_{\epsilon\to 0} \int_{\epsilon}^{\infty} \frac{dt}{\sqrt{t}} \exp\left(-\left|\mathbf{r}_i - \mathbf{r}_j + \mathbf{R}\right|^2 t\right) \\
&= \frac{1}{2\sqrt{\pi}} \sum_{i=1}^{N} Q_i \sum_{j=1}^{N} Q_j \sum_{\mathbf{R}}{}' \left[\lim_{\epsilon\to 0} \int_{\epsilon}^{\alpha^2} \frac{dt}{\sqrt{t}} \exp\left(-\left|\mathbf{r}_i - \mathbf{r}_j + \mathbf{R}\right|^2 t\right) \right. \quad (2.22) \\
&\qquad \left. + \int_{\alpha^2}^{\infty} \frac{dt}{\sqrt{t}} \exp\left(-\left|\mathbf{r}_i - \mathbf{r}_j + \mathbf{R}\right|^2 t\right) \right] \\
E_{\mathrm{pb}} &= \frac{\sigma}{\sqrt{\pi}} \sum_{i=1}^{N} Q_i \int_{L} \sum_{\mathbf{R}} \lim_{\epsilon\to 0} \int_{\epsilon}^{\infty} \frac{dt}{\sqrt{t}} \exp\left(-r^2 t\right) \\
&= \frac{\sigma}{\sqrt{\pi}} \sum_{i=1}^{N} Q_i \int_{0}^{\infty} 2\pi r\, dr \lim_{\epsilon\to 0} \int_{\epsilon}^{\infty} \frac{dt}{\sqrt{t}} \exp\left(-r^2 t\right) \quad (2.23) \\
E_{\mathrm{bb}} &= \frac{\sigma^2}{2\sqrt{\pi}} \int_{L} \int_{L} \sum_{\mathbf{R}} \lim_{\epsilon\to 0} \int_{\epsilon}^{\infty} \frac{dt}{\sqrt{t}} \exp\left(-r^2 t\right) \\
&= \frac{\sigma^2}{2\sqrt{\pi}} \int_{L} \int_{0}^{\infty} 2\pi r\, dr \lim_{\epsilon\to 0} \int_{\epsilon}^{\infty} \frac{dt}{\sqrt{t}} \exp\left(-r^2 t\right), \quad (2.24)
\end{aligned}
$$

introducing $\alpha > 0$ as an arbitrary parameter of the summation, i.e., the result is independent of α when the infinite sums are carried out. We can carry out the integration over r in the expressions for E_{pb} and E_{bb}:

$$
\begin{aligned}
E_{\mathrm{pb}} &= \frac{\sigma}{\sqrt{\pi}} \left[\sum_{i=1}^{N} Q_i \right] \lim_{\epsilon\to 0} \int_{\epsilon}^{\infty} \frac{dt}{\sqrt{t}} \int_{0}^{\infty} 2\pi r \exp\left(-r^2 t\right) \\
&= \sigma\sqrt{\pi} \left[\sum_{i=1}^{N} Q_i \right] \lim_{\epsilon\to 0} \int_{\epsilon}^{\infty} \frac{dt}{t^{3/2}} \\
&= 2\sqrt{\pi} \left[\sum_{i=1}^{N} Q_i \right] \sigma \lim_{\epsilon\to 0} \frac{1}{\sqrt{\epsilon}} \quad (2.25) \\
E_{\mathrm{bb}} &= \frac{\sigma^2}{2\sqrt{\pi}} \int_{L} \lim_{\epsilon\to 0} \int_{\epsilon}^{\infty} \frac{dt}{\sqrt{t}} \int_{0}^{\infty} 2\pi r \exp\left(-r^2 t\right) dr \\
&= \frac{\sigma^2 \sqrt{\pi}}{2} S_0 \lim_{\epsilon\to 0} \int_{\epsilon}^{\infty} \frac{dt}{t^{3/2}} \\
&= \sqrt{\pi}\sigma^2 S_0 \lim_{\epsilon\to 0} \frac{1}{\sqrt{\epsilon}}, \quad (2.26)
\end{aligned}
$$

where S_0 is the area of the unit cell.

We can see that the terms for E_{pb} and E_{bb} are divergent, so they have to cancel out with other terms obtained from E_{pp}. Since we can only carry out the second integral in the

expression for E_{pp} (see Equation 2.22), we use the Poisson-Jacobi formula

$$\sum_{\boldsymbol{R}} \exp\left(-\left|\boldsymbol{r}_i - \boldsymbol{r}_j + \boldsymbol{R}\right|^2 t\right) = \frac{1}{S_0}\frac{\pi}{t}\sum_{\boldsymbol{G}} \exp\left(-\frac{G^2}{4t}\right)\exp\left[\imath\boldsymbol{G}\cdot(\boldsymbol{r}_i - \boldsymbol{r}_j)\right], \quad (2.27)$$

where $\boldsymbol{G}$ represents the reciprocal lattice vectors, including the vector $\boldsymbol{0}$. We now use this expression for the first integral (by completing the primed sum) and carry out the second integral

$$
\begin{aligned}
E_{\text{pp}} &= \frac{1}{2\sqrt{\pi}}\sum_{i=1}^{N}Q_i\sum_{j=1}^{N}Q_j\lim_{\epsilon\to 0}\int_{\epsilon}^{\alpha^2}\frac{dt}{\sqrt{t}}\sum_{\boldsymbol{R}}\exp\left(-\left|\boldsymbol{r}_i - \boldsymbol{r}_j + \boldsymbol{R}\right|^2 t\right)\\
&\quad -\sum_{i=j}^{N}Q_i^2\lim_{\epsilon\to 0}\int_{\epsilon}^{\alpha^2}\frac{dt}{\sqrt{t}} + \frac{1}{2}\sum_{i=1}^{N}Q_i\sum_{j=1}^{N}Q_j\sum_{\boldsymbol{R}}{}'\frac{1}{r}\operatorname{erfc}\left(\alpha r\right)\\
&= \frac{1}{2\sqrt{\pi}}\sum_{i=1}^{N}Q_i\sum_{j=1}^{N}Q_j\lim_{\epsilon\to 0}\int_{\epsilon}^{\alpha^2}\frac{dt}{\sqrt{t}}\frac{\pi}{S_0 t}\sum_{\boldsymbol{G}}\exp\left(-\frac{G^2}{4t}\right)\exp\left[\imath\boldsymbol{G}\cdot(\boldsymbol{r}_i - \boldsymbol{r}_j)\right]\\
&\quad -\frac{\alpha}{\sqrt{\pi}}\left[\sum_{i=1}^{N}Q_i^2\right] + \frac{1}{2}\sum_{i=1}^{N}Q_i\sum_{j=1}^{N}Q_j\sum_{\boldsymbol{R}}{}'\frac{1}{r}\operatorname{erfc}\left(\alpha r\right)\\
&= \frac{\sqrt{\pi}}{2S_0}\left[\sum_{i=1}^{N}Q_i\right]\left[\sum_{j=1}^{N}Q_j\right]\lim_{\epsilon\to 0}\int_{\epsilon}^{\alpha^2}\frac{dt}{t^{3/2}}\\
&\quad +\frac{\sqrt{\pi}}{2S_0}\sum_{\boldsymbol{G}\neq 0}\left[\sum_{i=1}^{N}Q_i\exp\left(\imath\boldsymbol{G}\cdot\boldsymbol{r}_i\right)\right]\left[\sum_{j=1}^{N}Q_j\exp\left(-\imath\boldsymbol{G}\cdot\boldsymbol{r}_j\right)\right]\lim_{\epsilon\to 0}\int_{\epsilon}^{\alpha^2}\frac{dt}{t^{3/2}}\exp\left(-\frac{G^2}{4t}\right)\\
&\quad -\frac{\alpha}{\sqrt{\pi}}\left[\sum_{i=1}^{N}Q_i^2\right] + \frac{1}{2}\sum_{i=1}^{N}Q_i\sum_{j=1}^{N}Q_j\sum_{\boldsymbol{R}}{}'\frac{1}{r}\operatorname{erfc}\left(\alpha r\right)\\
&= -\frac{\sqrt{\pi}}{\alpha S_0}\left[\sum_{i=1}^{N}Q_i\right]^2 + \frac{\sqrt{\pi}}{S_0}\left[\sum_{i=1}^{N}Q_i\right]^2\lim_{\epsilon\to 0}\frac{1}{\sqrt{\epsilon}} \qquad (2.28)\\
&\quad +\frac{\pi}{S_0}\sum_{\boldsymbol{G}\neq 0}\left\|\sum_{i=1}^{N}Q_i\exp\left(\imath\boldsymbol{G}\cdot\boldsymbol{r}_i\right)\right\|^2\frac{1}{G}\operatorname{erfc}\left(\frac{G}{2\alpha}\right)\\
&\quad -\frac{\alpha}{\sqrt{\pi}}\left[\sum_{i=1}^{N}Q_i^2\right] + \frac{1}{2}\sum_{i=1}^{N}Q_i\sum_{j=1}^{N}Q_j\sum_{\boldsymbol{R}}{}'\frac{1}{r}\operatorname{erfc}\left(\alpha r\right).
\end{aligned}
$$

We can now reorganize the obtained expressions into four contributions: a real space summation $E^{(r)}$, a reciprocal space summation $E^{(k)}$, constant terms $E^{(c)}$ that are independent of the positions of particles or the lattice periodicity, and divergent terms $E^{(\text{div})}$. The real

space summation is simply given by

$$E^{(r)} \quad = \quad \frac{1}{2} \sum_{i=1}^{N} Q_i \sum_{j=1}^{N} Q_j \sum_{\boldsymbol{R}}{}' \frac{1}{r} \mathrm{erfc}\left(\alpha r\right).$$ (2.29)

The function to be summed over decays much faster than the original $1/r$-dependent term in V_{Coulomb} such that the sum converges quickly and unconditionally. Note that in the limit $\alpha \to 0$, we recover the original expression for the Coulomb interaction, i.e., the entire summation is carried out in real space.

The reciprocal space summation is given by

$$E^{(k)} \quad = \quad \frac{\pi}{S_0} \sum_{\boldsymbol{G} \neq 0} \left\| \sum_{i=1}^{N} Q_i \exp\left(\imath \boldsymbol{G} \cdot \boldsymbol{r}_i\right) \right\|^2 \frac{1}{G} \mathrm{erfc}\left(\frac{G}{2\alpha}\right).$$ (2.30)

Again, this summation converges rapidly and can thus be handled numerically. The constant terms are given by

$$E^{(c)} \quad = \quad -\frac{\sqrt{\pi}}{\alpha S_0} \left[\sum_{i=1}^{N} Q_i\right]^2 - \frac{\alpha}{\sqrt{\pi}} \left[\sum_{i=1}^{N} Q_i^2\right].$$ (2.31)

Even though these terms are independent of the lattice, they are very important, since they often represent the main contribution to the total energy of the system. Finally, the divergent terms add up to

$$
\begin{aligned}
E^{(\mathrm{div})} \quad &= \quad 2\sqrt{\pi}\sigma \left[\sum_{i=1}^{N} Q_i\right] \lim_{\epsilon \to 0} \frac{1}{\sqrt{\epsilon}} + \sqrt{\pi}\sigma^2 S_0 \lim_{\epsilon \to 0} \frac{1}{\sqrt{\epsilon}} + \frac{\sqrt{\pi}}{S_0} \left[\sum_{i=1}^{N} Q_i\right]^2 \lim_{\epsilon \to 0} \frac{1}{\sqrt{\epsilon}} \\
&= \quad \frac{1}{S_0} \left(\sigma S_0 + \left[\sum_{i=1}^{N} Q_i\right]\right)^2 \sqrt{\pi} \lim_{\epsilon \to 0} \frac{1}{\sqrt{\epsilon}} \\
&= \quad (0) \lim_{\epsilon \to 0} \frac{1}{\sqrt{\epsilon}},
\end{aligned}
$$ (2.32)

i.e., the divergent terms cancel as long as global electro-neutrality $\left(\sigma S_0 + \left[\sum_{i=1}^{N} Q_i\right] = 0\right)$ is satisfied.

In principle, the derivation of Ewald summation presented above can be performed for any form of the interaction potential. However, the success of this method critically depends on the knowledge of certain integrals such as Equation 2.21.

2.1.4. Ewald summation: implementation and convergence

Even though the particular form of an Ewald summation varies with the considered interaction potential, its basic features remain the same as presented in Subsection 2.1.3: there are terms related to the real space summation, to the reciprocal space summation, constant terms, and divergent terms; the latter have to cancel in order for the summation to converge. As mentioned before, the summations still contain an infinite number of terms, since the expression is *mathematically* exact. However, the Ewald summation formalism is much more manageable *numerically* since the sums converge quickly.

Thus, we can introduce cutoff distances in real and reciprocal space, R_{cut} and G_{cut}, respectively, beyond which we neglect all contributions in $E^{(r)}$ (see Equation 2.29) and $E^{(k)}$ (see Equation 2.30). In our effort to obtain a desired numerical accuracy δ, we need to optimize these cutoff distances, as well as the Ewald summation parameter α introduced above. On its own, α does not have a direct physical meaning. It can to some extent be considered the inverse length scale at which we switch from the real space summation to the reciprocal space summation (see Figure 2.2). Small values of α shift most of the summation to real space, while large values do so for reciprocal space (see Figure 2.2). During the derivation presented above, we have not considered any specific numerical value of α. While the result is independent of this value if the infinite sums are carried out, this is no longer true for the truncated summation we use (for an example, see left panel of Figure 2.4). Obviously, such an effect has to be avoided. Therefore, we have to carefully choose compatible values of R_{cut}, G_{cut}, and α, such that the total energy calculation is independent of α (at least within a reasonably large range of α). Such a plateau region in the energy calculation indeed exists if the cutoff distances are sufficiently large and increases in width as the cutoff distances increase. In order to obtain numerically accurate results for the potential energy, we thus have to test our summation for several different configurations and check that α is chosen from an interval where the final result does not depend on α, i.e., where $dE/d\alpha \approx 0$ (see right panel of Figure 2.4).

Depending on the interaction potential and on the geometry of the system, the actual numerical cost of Ewald sums can be substantial. Note that in Equation 2.30 we have factorized the double sum into two separate single sums. While this may only offer a moderate improvement for a small number N of particles per cell, it is essential for the simulation of large boxes, e.g. in Monte Carlo simulations. Certain geometries, e.g., a quasi-2D slab system, do not permit the factorization of double sums in the reciprocal space contribution and the associated numerical cost thus becomes prohibitively large (see also Appendix A.1.3).
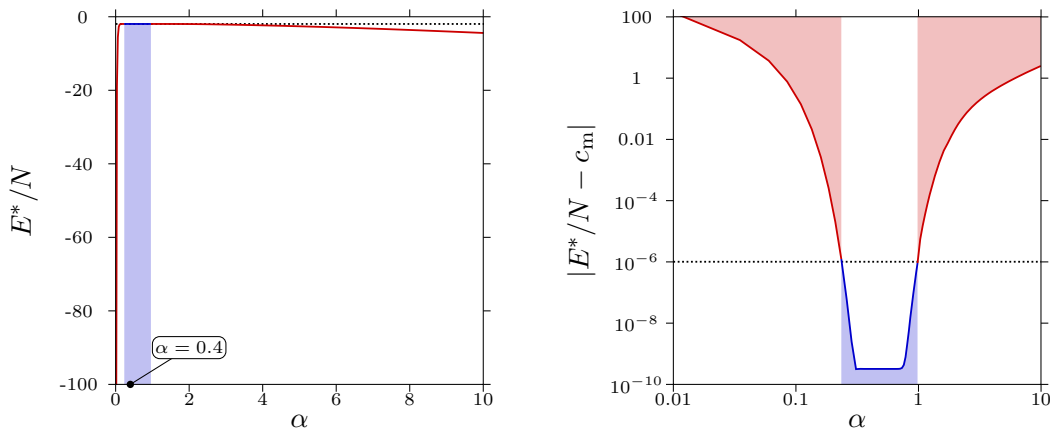
Figure 2.4.: α-dependence of the Ewald summation for the hexagonal Wigner monolayer, i.e., a hexagonal (equilateral triangular) arrangement of point charges on a uniform neutralizing background (see text). The exact energy is known to be $E^*_{\mathrm{hex}}/N = c_{\mathrm{m}} = -1.960515789$. Left panel: the energy calculation E^*/N diverges for small and large values of α (indicated by red line color). If α is chosen in a plateau region (shaded blue), E^*/N is constant for a certain interval. The correct energy c_{m} is indicated by a dotted line. The size of the interval increases with increasing cutoff distances R_{cut} and G_{cut}. Right panel: double-logarithmic plot of the error $|E^*/N - c_{\mathrm{m}}|$ giving an estimate of the attainable accuracy. The desired accuracy $\delta \approx 10^{-6}$ is indicated by a dotted line.

2.2. Global energy minimization: evolutionary algorithms

In this section, we introduce the term "energy landscapes" and discuss the problems we face in our search for global minima (see Subsection 2.2.1). We present an overview over possible strategies to approach this particular problem (see Subsection 2.2.2) and then focus on the specific method we employ in this work for solving it, namely evolutionary algorithms (see Subsection 2.2.3). After explaining their underlying concepts, we describe our implementation of these algorithms and modifications we have introduced to satisfy our requirements (see Subsection 2.2.4). Finally, we discuss in detail the different relevant operators of our evolutionary algorithm implementation (see Subsection 2.2.5).

2.2.1. Complex energy landscapes

In this work, we are interested in – possibly complicated – crystal lattices formed by particles interacting via long-ranged potentials. As mentioned in Chapter **??**, we first intend to determine the ground state – the structure formed at vanishing temperature – of such a system. A three-dimensional periodic lattice can be parametrized by its lattice vectors – $\boldsymbol{a}$, $\boldsymbol{b}$, and $\boldsymbol{c}$ – and the positions $\boldsymbol{r}_i$ and orientations $\boldsymbol{u}_i$ ($i = 1, ..., N$) of the N particles populating the unit cell. Due to symmetry considerations, not all of these parameters are independent, but even for a moderately large value of N, the number of parameters that need to be considered might reach up to several hundred.

The target function we seek to optimize – the enthalpy per particle, H/N, or the energy per particle, E/N, in the NVT or in the NPT ensembles, respectively – are complicated, though analytic, functions of these parameters

$$\frac{H}{N} \;=\; \frac{H}{N}\left(\boldsymbol{a}, \boldsymbol{b}, \boldsymbol{c}; \boldsymbol{r}_1, ..., \boldsymbol{r}_N; \boldsymbol{u}_1, ..., \boldsymbol{u}_N\right) \to \min \tag{2.33}$$

or

$$\frac{E}{N} \;=\; \frac{E}{N}\left(\boldsymbol{a}, \boldsymbol{b}, \boldsymbol{c}; \boldsymbol{r}_1, ..., \boldsymbol{r}_N; \boldsymbol{u}_1, ..., \boldsymbol{u}_N\right) \to \min. \tag{2.34}$$

These target functions are functions in the high-dimensional space of the parameters; their overall shape is called the *energy landscape*. Figure 2.5 shows two different examples for a simplistic one-dimensional energy landscape. In some very simple cases, the energy landscape exhibits only a single minimum over the entire parameter space (being then by default the *global* minimum), which makes the minimization problem easily solvable (see left panel of Figure 2.5). However, most energy landscapes have several – more or less pronounced – *local* minima, complicating thus the solution of the optimization problem (see right panel of Figure 2.5). As long as the number of local minima is relatively small, it is still rather easy to find the *global* minimum. However, we cannot assume this for the systems we plan to investigate in this work. In addition, these systems are characterized by a large number of

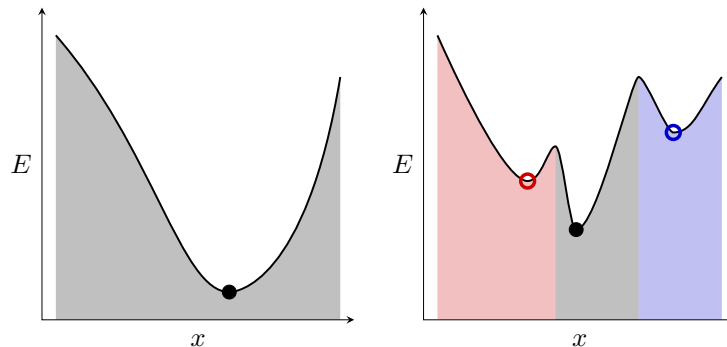parameters, resulting in a so-called *rough* energy landscape, which can be exceedingly hard to deal with.

Figure 2.5.: Simple examples of one-dimensional energy landscapes within a limited parameter range. The target function E depends on the parameter x. *Local* minima are marked by empty circles, the *global* minimum by a filled circle. The attraction basin for each minimum is shaded in its respective color. Left panel: the *global* optimization problem is easily solvable if there is only a single (or very few) minima. Right panel: rough energy landscapes have a large number of local minima, a fact which complicates the search for the global minimum.

In addition, some systems investigated in this work show a competition between two different interactions. This competition can lead to frustration in the ground state configuration, i.e., minimizing the contribution to the total energy stemming from one interaction may increase the contribution from another interaction.

2.2.2. Global minimization strategies

Complex energy landscapes emerge in a large variety of scientific fields, such as protein folding [78–80], chemical engineering [81, 82], and many others. Not surprisingly, an equally large number of approaches has been developed over the years to solve the associated global optimization problems. These approaches can roughly be classified into three categories: deterministic, stochastic, and heuristic.

Deterministic minimization strategies try to solve the optimization problem in an exact and reproducible manner. They are based on mathematical treatment of the solution space and analytical determination of possible solutions [83–85]. In some cases, an educated guess for the general shape and symmetry of the solution can be made, considering inner symmetries of the problem. If the general shape of the solution is known, it is sometimes possible to calculate the global energy minimum by *locally* optimizing this candidate solution with a suitable gradient descent algorithm. The region surrounding a local minimum is denoted the *attraction basin* and following the gradient from any point in the basin leads to the local minimum.

Stochastic minimization strategies are based on a sampling of the parameter space via random events. For example, the energy landscape can be explored using a simple direct Monte Carlo simulation at a suitably low temperature. While on the one hand such a simulation may get stuck in local minima, it is on the other hand also able to cross energy barriers due to the finite temperature. However, careful attention has to be paid to the barrier heights, to the relative energy depths of local minima and to the temperature of the system. This general approach can be improved upon by introducing mechanisms to better sample the parameter space, e.g., by stochastic tunneling [86, 87]. This method improves the sampling rate by transforming the parameter space in a non-linear way, allowing for easier movement between different local minima. Other Monte Carlo-based approaches include simulated annealing [88, 89], where simulations start at a high temperature and the system is then gradually cooled down, and parallel tempering (also called replica exchange) [90], where several systems are run in parallel at different temperatures and configurations can be exchanged between two temperatures with a certain probability.

Finally, heuristic minimization strategies try to explore the search space in a more intelligent way, making use of already obtained knowledge on the target function, such as symmetries, boundaries, etc. With algorithms of this kind, it is of particular importance to tailor them to the problem at hand. In general, we cannot assume that an algorithm that has been optimized to solve problems of one kind will be appropriate at solving problems of a different kind; this is known as the infamous *no free lunch* theorem [91]. One kind of heuristic minimization strategies are swarm-based algorithms [92, 93]. The "swarm" considered here consists of several points in search space which are considered as an ensemble. These points can be located in different basins of the energy landscape and the interplay between the different members of a swarm may give further information concerning the overall shape of the energy landscape. Another heuristic approach is reactive search [94], which employs elements of machine learning to make use of underlying mechanisms which may be difficult to extract analytically. A different possible approach is graduated optimization [95]. Here, the actual problem is in a first step strongly simplified such that it becomes easily solvable. Starting from this basic solution, more and more of the problem's original complexity is iteratively added, all the while tweaking the previously obtained solution, until a hopefully good solution to the original problem is found. Another possible approach is differential evolution [96], where the initial problem is broken in many different sub-problems and a solution is iteratively optimized for each sub-problem separately. In this work, we use the method of evolutionary algorithms [97, 98], which tries to iteratively combine or modify different previously obtained solutions by making use of evolutionary principles. This approach can also be combined with local optimization techniques, e.g., gradient descent algorithms [99–104], in order to improve performance and convergence speed; algorithms combining both global and local search strategies are called memetic algorithms [105].

2.2.3. Evolutionary algorithms: principles

Darwinian theory of evolution

In this work, the main optimization strategy we employ to study global energy minima is based on concepts of evolutionary algorithms (EAs) [98, 106]. EAs are derived from the Darwinian theory of evolution [107] in biological systems. The theory of evolution explains the gradual adaptation of a population of individuals to its environment in order to increase its chances of survival and implicitly of passing on its genetic material. It is based on the following three assumptions:

- Different individuals have different traits, i.e., there are different *genotypes* (genetic material) and associated *phenotypes* (physical traits determined by genetic material).
- Different traits imply different adaptation to the environment and a different probability to create offspring.
- Traits can be passed on to the next generation.

Since it is more likely for well-adapted individuals to create offspring, "good" traits have a higher chance for being passed on to subsequent generations; over time the population selects for individuals which are better adapted to the environment (the degree of adaptation is quantified as the *fitness*). In addition, random changes in traits occur with a small probability, introducing thereby new traits; this process is called mutation.

Principles of evolutionary algorithms

In biology, the environment is a highly complex system and how well an individual is adapted to it depends on many factors: it may depend on the rest of the population and may also change over time. Therefore, we cannot specify any deterministic quantification of the degree of adaptation.

For the development of an algorithm incorporating some of the underlying concepts of evolution, we need to radically simplify and quantify both the environment and the degree of adaptation. Our sole interest lies in optimizing a certain analytically known target function such as a particle configuration's energy. In most implementations of EAs, this target function remains unchanged over time and also doesn't depend on the rest of the population (in the following, we denote members of the population *candidates* to distinguish them from their biological counterparts). We can thus use the value of the target function to numerically quantify the degree of adaptation to the environment. This quantity is denoted the *fitness* of a candidate; a lower target function value equals a higher fitness value.

The biological processes of procreation and mutation can also be used as inspiration for algorithmic operators. The operator associated with procreation is denoted *crossover*. Its purpose is to statistically extract and combine information from good solution strategies. The *mutation* operator on the other hand serves to introduce completely new solution strategies.

Both crossover and mutation only lead to a significant improvement if a sufficient number of iterations is performed.

The aim of the crossover operator lies in combining good traits from two candidates without actually knowing what these good traits are. This fact is very important, since the systems we plan to study can be quite complex (see Subsection 2.2.1). We can select for good traits by preferring good candidates (with high fitness) as source material for crossover. If this process is repeated many times, good traits have a higher chance of being passed on and thus they accumulate. The left panel of Figure 2.8 shows a simple example of the crossover operator, where good traits of two candidates are combined at random. The crossover operator is described in more detail in Subsection 2.2.5.

However, the crossover operator alone is to some extent limited by the good traits already existing in the population as it is difficult to introduce completely new solution strategies via this process. To compensate for this shortcoming, EAs employ a second genetic operator, mutation. The mutation operator's goal is to introduce random new traits to the population. Since these traits are random, they in most cases have negative consequences for a candidate's fitness, but may nevertheless cause a better exploration of the search space. Mutation is used only sparsely, i.e., the crossover operator is used much more often for the creation of a new candidate. The different mutation operators are explained in more detail in Subsection 2.2.5.

2.2.4. Evolutionary algorithms: implementation

Parametrization

As mentioned before, we try to keep our algorithm as flexible as computationally possible. In the ideal case, the algorithm should be able to explore and consider all possible solutions. In practice, this *ergodicity* is restrained to some extent for computational reasons. The systems we are going to investigate are periodic crystals, i.e., they can be characterized by a unit cell, which is repeated periodically in accordance with the geometry of the system. The unit cell's shape and size is defined by the lattice vectors $\boldsymbol{a}$, $\boldsymbol{b}$, and $\boldsymbol{c}$. Without loss of generality, we assume in a three-dimensional (3D) system that vector $\boldsymbol{a}$ is aligned along the x-axis and

that vector $\boldsymbol{b}$ lies in the xy-plane, i.e.,

$$\boldsymbol{a} \;=\; \begin{pmatrix} a_x \\ 0 \\ 0 \end{pmatrix} \tag{2.35}$$

$$\boldsymbol{b} \;=\; \begin{pmatrix} b_x \\ b_y \\ 0 \end{pmatrix} \tag{2.36}$$

$$\boldsymbol{c} \;=\; \begin{pmatrix} c_x \\ c_y \\ c_z \end{pmatrix}. \tag{2.37}$$

The unit cell volume V_{c} is then simply given by

$$V_{\mathrm{c}} \;=\; |(\boldsymbol{a} \times \boldsymbol{b}) \cdot \boldsymbol{c}| = |a_x b_y c_z|\,, \tag{2.38}$$

whereas in two-dimensional (2D) systems, the corresponding interesting quantity is the unit cell area $S_0 = |a_x b_y|$. When investigating systems at constant density, we can fix in a three-dimensional system the unit cell volume by setting

$$a_x \;=\; \frac{V_{\mathrm{c}}}{b_y c_z}. \tag{2.39}$$

In 2D systems, we use $a_x = S_0/b_y$. In 3D systems, we thus have six independent parameters that describe the shape of the unit cell (five in NVT), while in 2D we only have three (two in NVT).

The particle positions within the unit cell can be specified either in Cartesian coordinates $\boldsymbol{r}_i$ or, preferably, in *fractional* coordinates $\boldsymbol{r}_i^{\mathrm{f}}$

$$\boldsymbol{r}_i \;=\; x_i^{\mathrm{f}}\boldsymbol{a} + y_i^{\mathrm{f}}\boldsymbol{b} + z_i^{\mathrm{f}}\boldsymbol{c}, \tag{2.40}$$

such that the range of each component of $\boldsymbol{r}_i^{\mathrm{f}}$ can be confined to the interval $[0,1)$. The use of fractional coordinates also simplifies certain genetic operators, in particular crossover. Particle orientations are specified by a three-component vector following the formalism described by Chakrabarti [108], wherein the rotation axis is given by the vector's director and the rotation angle by its length such that any orientation of a rigid body in 3D space can be described. Depending on the system, the number of orientation parameters per particle ranges between zero (isotropic particles) and three (three-dimensional rigid bodies).

For computational reasons, we keep the number of particles per cell, N, fixed during a run. On the one hand, this greatly simplifies all genetic operators; on the other hand, however, we have to perform runs for several different values of N to cover all relevant unit cell sizes. Typical system sizes range between $N = 1$ and $N = 40$ particles per cell, but can reach a

few hundred.

The set of parameters listed above – consisting of lattice vectors, particle positions and particle orientations – is called a candidate's *phenotype*. They determine its physical characteristics (in our case the crystal lattice) and are used for the evaluation of the target function. In traditional EAs, these properties are encoded as a sequence of binary numbers, similar to a genetic code [98], which is called the *genotype* of the candidate. The biological counterparts of phenotype and genotype are the actual individual and its DNA, respectively. EAs can be implemented either in phenotype formalism (which we use in this work and where a candidate is described by a set of parameters), or in genotype formalism (where the parameters are converted into a single string of binary numbers). While most genetic operators can be more directly related to their biological counterparts in the genotype formalism, the phenotype implementation allows for more flexibility and for an easier exploitation of the optimization problem's physical interpretation.

Fitness

As mentioned in Subsection 2.2.3, a candidate's adaptation to the environment is related to its chances of producing offspring and passing on its genetic material. This level of adaptation is quantified in the *fitness* of a candidate. For our purposes, a candidate (i.e., a crystal lattice) is well-adapted when its energy E is low, since this is the quantity we seek to minimize. The fitness F should thus be high for a low energy configuration and vice versa. The functional form of the fitness function $F(E)$ is a key ingredient of the algorithm's implementation. A commonly used function [98, 106, 109, 110] is

$$F(E) \quad = \quad \exp\left(-s\frac{E - E_{\min}}{E_{\max} - E_{\min}}\right) \tag{2.41}$$

$$\exp(-s) \leq \quad F(E) \quad \leq 1, \tag{2.42}$$

where $E_{\min}$ and $E_{\max}$ are the minimum and maximum energies within the population, respectively. The parameter s specifies how much more likely it is for fitter candidates to reproduce, since a large value of s basically excludes weak candidates from reproduction. We commonly use $s = 3$, such that the ratio between the minimum and maximum fitness is

$$\frac{F(E_{\max})}{F(E_{\min})} \quad = \quad \exp(-s) \approx 0.05. \tag{2.43}$$

There are several different methods to pick candidates for reproduction. In this work, we employ the so-called *roulette wheel* method [106, 109, 111], where a re-scaled fitness function is used to calculate the probability for a candidate to be picked. The re-scaled fitness $f(E)$ can be calculated after sorting the N_{ind} candidates by their fitness $F(E)$ in descending order

$(F_{i+1} < F_i$, where $i = 1, ..., N_{\text{ind}})$

$$f(E_i) = \frac{\sum_{j \leq i} F(E_j)}{\sum_{j=1}^{N_{\text{ind}}} F(E_j)}. \tag{2.44}$$

In order to pick a candidate for reproduction, we can generate a random number $0 \leq r \leq 1$ and pick the candidate with the smallest index i such that $f(E_i) \geq r$. Figure 2.6 shows an illustration of the relation between energy, fitness, re-scaled fitness, and the probability of being picked.
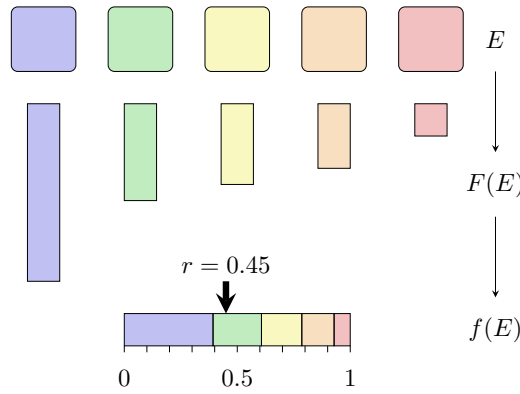

Figure 2.6.: Illustration of the relation between energy E, fitness $F(E)$, re-scaled fitness $f(E)$, and the probability of being picked for reproduction (when picking at random by generating $0 \leq r \leq 1$; shown here is $r = 0.45$). Candidates with low energy (colored blue or green) have a high fitness and are thus more likely to be chosen for reproduction.

Local optimization

For most problems, it is useful to combine global and local approaches, i.e., to use a memetic approach. The idea here is to first find the attraction basin of the global minimum with a global search algorithm and then to rapidly converge to the minimum with a local search algorithm. There are various ways to balance the computational effort allocated to global and local optimization, ranging from purely global (e.g., early EAs [98, 110]) to purely local (local optimization of candidate structures).

In our implementation of EAs, we use an approach based on basin hopping [112], i.e., we combine a global evolutionary search algorithm with a subsequent local optimization until all forces vanish. The energy landscape thus reduces to a set of attraction basins and the associated local minima. This improves performance of the algorithm since the energy differences between a local minimum and other regions in its attraction basin can range over several orders of magnitude. In traditional EAs, the creation of a new configuration requires only a single evaluation of its energy. In basin hopping, fully *relaxing* a configuration

(optimizing it locally until all forces are below a certain threshold) can require hundreds or thousands of energy evaluations.

For the local optimization, we employ the linearized Broyden-Fletcher-Greenfarb-Shanno algorithm in its bounded variant (L-BFGS-B) [99–104], which is based on an approximation of the inverse Hessian matrix of the energy function. This approximation is updated iteratively after each step. The term *linearized* refers to an implementation based on a limited amount of memory, i.e., the matrix is stored only implicitly and only a limited number of previous updates is kept. This is particularly efficient in systems with a large number of variables.

Parallelization

As mentioned before, a candidate's fitness is only meaningful in comparison to the fitness values of the other candidates in the population, since it quantifies the competition for producing offspring. In traditional implementations of EAs, the creation of new candidates is organized via *generations*, i.e., the entire population is replaced by new candidates in each iteration (see left panel of Figure 2.7). In order to reach convergence, a large number of iterations may be necessary. For computational reasons, it is thus more appropriate to develop a parallelized implementation. One possible way of achieving this is by abandoning the concept of generations [106] and introducing instead a *pool* of candidates, containing the entire population. New candidates are created one at a time and replace one of the old candidates in the pool (see right panel of Figure 2.7). The respective fitness of each candidate is then recalculated and the process is repeated until a certain number of iterations has been reached.
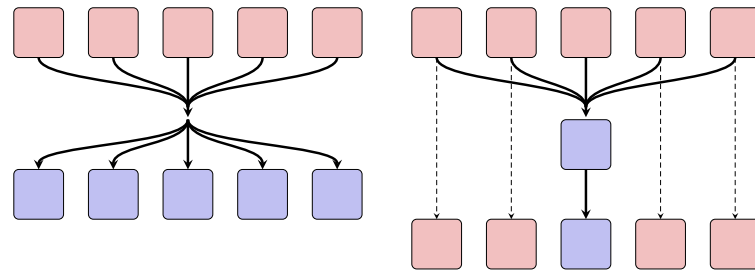

Figure 2.7.: Schematic view of different implementations of evolutionary algorithms (EAs). Left panel: traditional implementation based on generations. In each iteration, the entire old population (colored red) is replaced by newly created candidates (colored blue). Right panel: implementation geared towards parallelization, in which the concept of generations is abandoned. New candidates are created one at a time and gradually replace old candidates.

It is a simple process to parallelize such iterative updates to a pool of candidates: a master node keeps track of the current pool and the fitness of each candidate. A new candidate is created by the master node using the crossover and mutation operators and is handed

to a worker node for local optimization. Once optimization is achieved, the new candidate is passed back to the master node and replaces a randomly picked candidate in the pool. The master node then recalculates the fitness of each candidate. All computational tasks performed by the master node require very little time avoiding thus the formation of a bottleneck. The time required to locally optimize a candidate using the L-BFGS-B algorithm can vary significantly and the different worker nodes thus do not work in sync. The number of worker nodes is to some extent related to the pool size N_{ind} and we commonly keep them approximately equal. Our implementation of parallelization uses the MPI framework [113].

Elitism and nicheing

In biological systems, all candidates in a population are replaced when a new generation is formed. In EAs, the best few candidates are usually carried over from one generation to the next in a method called *elitism* [106]. This prevents the population from losing good traits and ensures that the best obtained energy decreases monotonically. However, the degree of elitism should not be too high, otherwise the best few candidates dominate the rest of the population which then may be trapped in a few local minima.

The possibility that all candidates in the population converge to the same local minimum can indeed pose a risk as it precludes further useful crossovers. To prevent this from happening, we may employ a practice called *nicheing* [106, 114]. The niches here usually refer to energy niches, i.e., we discard a new candidate if its energy is identical to that of an old candidate already available in the pool. All candidates thus have to occupy different basins and their associated local minima. However, we have to be careful when dealing with systems where different but equivalent structures can exhibit the same energy and especially when the ground state may be degenerate. In this case, niches have to incorporate a quantification of a configuration's structure, e.g., the order parameters.

2.2.5. Evolutionary algorithms: operators

We now discuss our implementation of the different evolutionary operators and their relative probabilities. For the initial population, all candidates are initialized using the *random* operator, which creates a completely random candidate.

Crossover operator

The aim of the crossover operator is to combine good traits from two candidates (called *parents*) into a new candidate (called *child*). It stands apart from all other operators due to how often it is used (approximately 53-80% of all iterations) and that it uses two candidates as input. In genotype implementations, crossover is achieved by directly cutting and merging the genetic code of the two parents. In phenotype implementations, such as the one we

employ, it makes sense to use the physical interpretation of the system and to try to preserve to some extent good local structures.

For a crossover (see the left panel of Figure 2.8), the two parents are first chosen from the pool. The probability of a candidate to be chosen as a parent is determined by its fitness (see Subsection 2.2.4). We insists on two different candidates for the choice of parents. In order to create the child, we now randomly choose one parent that passes on its lattice vectors. Fractional particle positions and orientations are passed on in a more complicated manner called *cut-and-splice* [115]. First, we randomly choose how many particle positions N_1 and N_2 are passed on from each of the parents. We then determine a fractional coordinate axis $\hat{\boldsymbol{a}} \in \{x_\mathrm{f}, y_\mathrm{f}, z_\mathrm{f}\}$ orthogonal to the plane that cuts the two parents. Before cutting, we shift the fractional coordinates of both parents along the chosen axis $\hat{\boldsymbol{a}}$ by a random interval [116–118]; with a low probability, the shift occurs orthogonal to $\hat{\boldsymbol{a}}$. Then, we take the N_1 particles with the lowest fractional coordinate $\hat{\boldsymbol{a}}$ from the first parent and the N_2 particles with the highest fractional coordinate $\hat{\boldsymbol{a}}$ from the second parent and add them to the child. The associated particle orientations are also passed on. The rationale behind this is that the local relative structure is preserved, even though the actual positions depend on the lattice vectors, which may differ between parent and child. Without subsequent local optimization, the resulting configuration has most likely a rather high energy.

Move mutation operator

Like all other mutation operators, the *move* mutation operator (see right panel of Figure 2.8) seeks to introduce new information to the population by hopping to different basins. In genotype implementations, mutation occurs by randomly changing the genetic code. In phenotype implementations, we can directly interpret mutations, allowing us to tailor the operators to the problem at hand. For all systems studied in this work, randomly displacing a single particle is always useful. The move operator is thus used rather frequently, with a probability of 10-20%.

In a first step, we pick one candidate at random from the pool, which serves as the starting point. We then pick a single particle in this candidate and displace it by a random distance along a random direction. With a probability of 10-20%, this process is repeated, such that multiple particles can be displaced in a single mutation. The configuration is then optimized locally.

Strain mutation operator

If the unit cell contains only a few particles, the number of accessible crystal structures strongly depends on the lattice vectors, i.e., on the periodicity. We thus use the *strain* mutation operator (see left panel of Figure 2.9) to randomly change the shape (and in the NPT ensemble also the volume or area) of the unit cell allowing thereby the formation of
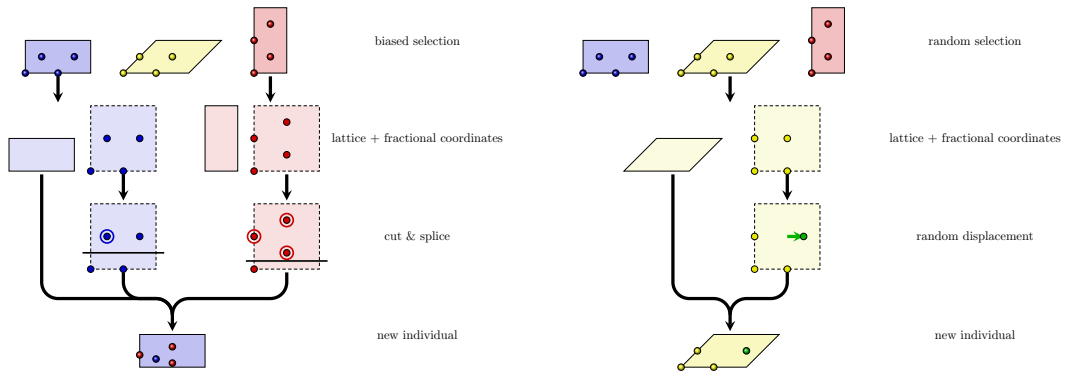
Figure 2.8.: Left panel: illustration of the *crossover* operator. Two parents with $N = 4$ particles are selected in a draw biased towards high fitness. One of them passes on its lattice vectors and the fractional coordinates of both parents are shifted along a random axis (see text). The (here) $N_1 = 1$ particles with the lowest new fractional coordinate are passed on from the first parent, complemented with the $N_2 = N - N_1 = 3$ with the highest new fractional coordinate from the second parent. Right panel: illustration of the *move* mutation operator. A candidate is picked at random and one (or more) particles are randomly displaced.

completely different lattices [116, 119]. The strain operator is used with a probability of 3-7%.

Again, we first pick a candidate at random from the pool. We then construct the strain matrix [116, 119]

$$M \;=\; \begin{pmatrix} 1 + \epsilon_{11} & \frac{\epsilon_{12}}{2} & \frac{\epsilon_{13}}{2} \\ \frac{\epsilon_{12}}{2} & 1 + \epsilon_{22} & \frac{\epsilon_{23}}{2} \\ \frac{\epsilon_{13}}{2} & \frac{\epsilon_{23}}{2} & 1 + \epsilon_{33} \end{pmatrix}, \tag{2.45}$$

where ϵ_{ij} are zero-mean random Gaussian variables. Finally, we obtain the mutated lattice vectors using

$$\begin{pmatrix} a'_x & 0 & 0 \\ b'_x & b'_y & 0 \\ c'_x & c'_y & c'_z \end{pmatrix} \;=\; M \cdot \begin{pmatrix} a_x & 0 & 0 \\ b_x & b_y & 0 \\ c_x & c_y & c_z \end{pmatrix}. \tag{2.46}$$

Depending on the used ensemble, the volume can either change or be kept constant.

Swap mutation operator

In systems with more than one component, the relative positions of the different species become important. It is thus useful to construct a *swap* mutation operator (see right panel

of Figure 2.9), which exchanges the species of two particles. When studying mixtures, we use a probability of 3-6% for this operator.

After picking a candidate at random, two particles are selected and their species are interchanged, leaving their positions and orientations untouched. This operator is especially useful when the two species are similar in their properties, as most other evolutionary operators would not be able to escape certain local minima. After the operator has been applied, the configuration is locally optimized.
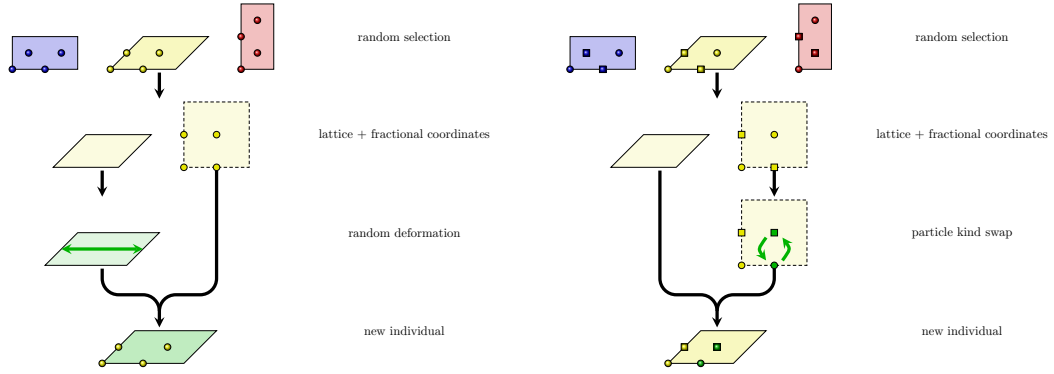
Figure 2.9.: Left panel: illustration of the *strain* mutation operator. A candidate is picked at random and its lattice vectors are randomly deformed. Right panel: illustration of the *swap* mutation operator. A candidate is picked at random and the species of two particles is interchanged.

Rotation mutation operator

In systems with anisotropic interactions, particle orientations are of equal importance as particle positions. In addition, local minima due to certain collective particle orientations may be strongly pronounced. We thus use the *rotation* mutation operator to randomly change the orientation of a single particle. It is used with a probability of 10-17%.

One particle in a randomly picked candidate is chosen and its orientation is changed by a small angle. The configuration is then locally optimized.

Random mutation operator

Finally, we also introduce a mutation operator, which simply creates a random new candidate. Our intention here is to add completely new combinations of traits to the population. However, this operator is only used in 3-7% of all cases. Random candidates are initialized with a fixed, pre-defined volume. The lattice vectors are generated such that the angles between them are equally distributed between $\pi/6$ and $\pi/3$ ($\pi/3$ and $2\pi/3$ in 2D) and the

ratios between their lengths are chosen randomly to be between 0 and 1. Fractional particle positions within the unit cell are equally distributed, as are the particle orientations.

2.3. Monte Carlo simulations

In this section, we describe the algorithm implemented for our finite temperature Monte Carlo (MC) simulations; these allow us to study both the stability of structures observed at zero temperature. We first describe the general employed algorithm (see Subsection 2.3.1) and then give details on our implementation (see Subsection 2.3.2).

2.3.1. Metropolis-Hastings algorithm

We employ standard Monte Carlo (MC) simulations using the Metropolis-Hastings algorithm [120, 121]. The box is defined by the lattice vectors $\boldsymbol{a}$ and $\boldsymbol{b}$ and contains N particles. We denote a *cycle* of the simulation as N attempted particle displacements and one attempt to change the shape of the box. The step sizes are chosen such that the acceptance ratio is 30-50%.

As usual, our Monte Carlo simulation runs have three phases:

Initialization: For the results presented in this work, we usually make use of information obtained with the EA by positioning the particles according to a zero temperature configuration. This strategy is particularly useful for complicated structures. Since unit cells in EA are usually rather small (on the order of a few dozen), we replicate this cell several times in all directions and obtain thus a simulation cell containing several thousand particles.

Equilibration: When the system is initialized, it is usually not yet in thermodynamical equilibrium, i.e., its free energy is not yet minimized. We therefore have to let the system *equilibrate* by performing a certain number of cycles during which the system adapts to the temperature and other parameters. This can involve a transformation of the lattice, the formation of defects, melting, etc.

Quantities measured during equilibration can not be used for averages since the system is not in equilibrium; however, their change over time can indicate how close we are to equilibrium.

Averages: In the subsequent production run, we store the positions of particles in intervals of a few hundred cycles and use this information to calculate relevant properties of the equilibrated system.

The numerical values for the system size N and the number of cycles performed for equilibration and averages are specified in the respective sections of Chapter 3.

2.3.2. Details on the implementation

The accurate treatment of long-ranged interactions in MC simulations with Ewald summation can be a costly endeavour for unit cells containing a large number of particles. Therefore, it is essential to improve the efficiency of the energy calculation as much as possible. In our implementation, we employ cell lists [122] and factorize sums in the Ewald summation (see Section 2.1 and Appendix A.1) whenever possible.

2.4. Voronoi construction and bond-orientational order parameters

In this section, we explain the concept of order parameters and how we can use them to quantify our results for an easier comparison and classification of observed structures (see Subsections 2.4.1 and 2.4.2). We focus on bond-orientational order parameters and discuss their meaning and how we can calculate them (see Subsection 2.4.4). We also treat the method of Voronoi construction, which is essential for a correct implementation of these order parameters (see Subsection 2.4.3); some important details on the implementation are also discussed (see Subsection 2.4.5). Appropriate order parameters have to be chosen specifically for each system and we therefore introduce and discuss them separately for the different studied systems in Chapter 3.

2.4.1. Motivation for order parameters

For any kind of simulation or calculation, the configurations and energies alone only contain a very limited amount of information. Even though we may be able to look at snapshots of configurations, a deeper understanding of what *exactly* we see may be difficult. In addition – since we also plan to construct phase diagrams – it can be difficult to manually evaluate hundreds of snapshots. We thus have a strong interest in some numerical parameters that can classify different structures and *quantify* what we see.

The concept of order parameters is built on this premise. Order parameters should allow us to detect phase transitions between different structures and provide information on the transition process between them. While the optimized quantity (the energy or enthalpy of the system) itself can provide this information to some degree, it can be insufficient for identifying structures. In some cases, order parameters can also provide additional, quantitative information on the structure of our system.

2.4.2. Definition of order parameters

From a thermodynamic point of view, order parameters are defined [123] as quantities that describe a transition between two phases: they commonly vanish in one phase and are equal to unity in the other. The choice of order parameters is not unique and depends on the system. The order of the phase transition is reflected in the behavior of the order parameter at the transition, i.e., the order parameter changes abruptly for a first order phase transition and changes continuously for a second order phase transition. Order parameters describing a phase transition are an essential element of Landau theory [124].

In addition, it is possible to extract further information on the phase transition from the first derivative of the order parameter [123, 125–127] – in particular on the critical exponents in second order phase transitions.

2.4.3. Neighborhoods and Voronoi construction

Order parameters are usually defined as sums over all particles in the system

$$\Psi \ \sim \ \sum_{i=1}^{N} \psi_i \left(\boldsymbol{r}_1, ..., \boldsymbol{r}_N; \boldsymbol{u}_1, ..., \boldsymbol{u}_N \right), \tag{2.47}$$

where $\boldsymbol{u}_i$ is the orientation of particle i. The *local* value of the order parameter, ψ_i, can depend either only on particle i or also on its neighbors. A simple example for the former case is the magnetization M of a system of N moments $\boldsymbol{m}_i$ (assuming that $|\boldsymbol{m}_i| = m$)

$$M \ = \ \frac{1}{Nm} \left| \sum_{i=1}^{N} \boldsymbol{m}_i \right|. \tag{2.48}$$

We give further details on order parameters of this type in the respective sections of Chapter 3 and focus in the following on order parameters depending on the entire neighborhood of a particle.

The local order parameter is a function depending on the nearest neighbors of particle i, i.e., the $\mathcal{N}_i$ particles closer to particle i than any others. We can thus roughly write the local order parameter ψ_i as a sum

$$\psi_i \left(\boldsymbol{r}_1, ..., \boldsymbol{r}_N; \boldsymbol{u}_1, ..., \boldsymbol{u}_N \right) \ \sim \ \sum_{j \in \mathcal{N}_i} \psi \left(\boldsymbol{r}_i, \boldsymbol{r}_j; \boldsymbol{u}_i, \boldsymbol{u}_j \right); \tag{2.49}$$

thus the global order parameter Ψ is given by

$$\Psi \ \sim \ \sum_{i=1}^{N} \sum_{j \in \mathcal{N}_i} \psi \left(\boldsymbol{r}_i, \boldsymbol{r}_j; \boldsymbol{u}_i, \boldsymbol{u}_j \right). \tag{2.50}$$

The evaluation of local order parameters strongly depends on the method we use for identifying "neighbors", i.e., on our definition of "proximity".

In this work, we use the well-defined method of Voronoi construction for determining neighborhoods of particles [128, 129] in two or three dimensions. In the following, we illustrate this algorithm for the two-dimensional case; differences in the algorithm for the three-dimensional case are outlined at the end of the subsection.

Mathematically, the Voronoi construction is based on an area containing a set of seeds, which correspond to our particle positions. We now try to find in this area those polygons associated with each particle such that any point within a polygon is closer to its central particle than to any other particle.

We can construct these polygons geometrically by picking one particle at position $\boldsymbol{r}_i$ (which we dub the "central" particle) and drawing equidistant lines between the position $\boldsymbol{r}_i$ and the positions $\boldsymbol{r}_j$ of all other particles. These lines are given – for particles i and j – via the following equation

$$g : \left[\boldsymbol{r} - \frac{1}{2} \left(\boldsymbol{r}_i + \boldsymbol{r}_j \right) \right] \cdot \hat{\boldsymbol{r}}_{ij}^{\perp} \;\; = \;\; 0, \tag{2.51}$$

where $\hat{\boldsymbol{r}}_{ij}^{\perp}$ is the normalized director perpendicular to the vector connecting particles i and j. The smallest polygon formed around the central particle i is then the Voronoi polygon (see bottom left panel of Figure 2.10). Repeating this process for all other particles yields the Voronoi construction of the lattice; the sum of all Voronoi polygons completely fills the entire space.

Mathematically, we construct Voronoi polygons by determining each vertex separately. Each possible vertex is determined by two particles j and k. We draw the lines equidistant from them and the central particle i and find their intersection point, i.e., a point $\boldsymbol{r}_{\mathrm{v}}$ which satisfies

$$\left[\boldsymbol{r}_{\mathrm{v}} - \frac{1}{2} \left(\boldsymbol{r}_i + \boldsymbol{r}_j \right) \right] \cdot \hat{\boldsymbol{r}}_{ij}^{\perp} \;\; = \;\; 0 \tag{2.52}$$

$$\left[\boldsymbol{r}_{\mathrm{v}} - \frac{1}{2} \left(\boldsymbol{r}_i + \boldsymbol{r}_k \right) \right] \cdot \hat{\boldsymbol{r}}_{ik}^{\perp} \;\; = \;\; 0. \tag{2.53}$$

In order to check whether this intersection point is an actual vertex of the Voronoi polygon, we have to verify that it is closer to the central particle than the equidistant line generated by any other particle m (see top left and right panels of Figure 2.10)

$$\frac{\boldsymbol{r}_{\mathrm{v}} - \boldsymbol{r}_i}{|\boldsymbol{r}_{\mathrm{v}} - \boldsymbol{r}_i|} \cdot \hat{\boldsymbol{r}}_{im} \leq \frac{1}{2}. \tag{2.54}$$

We define two particles sharing an edge of their polygons as neighbors of each other. Depending on the local geometry the distances between neighbors may vary widely. Also note that some lattices may have degenerate polygon edges, i.e., where an edge reduces to a single
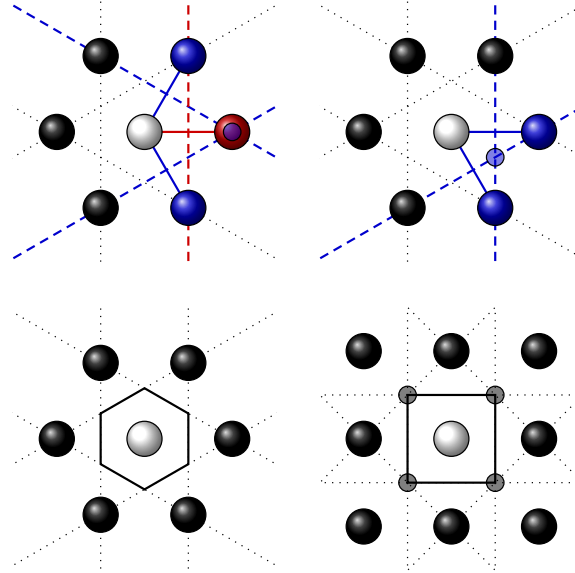
Figure 2.10.: Principles of a Voronoi construction. Dotted lines mark points equidistant from the central particle (colored white) and the respective neighbor candidate. The Voronoi polygon is defined as the area around the central particle that is void of any such lines. **Top row:** left panel: choice of two neighbor candidates (colored blue) that *doesn't* result in a valid vertex due to the presence of another particle (colored red). The produced intersection point (blue dot at the crossing of the dashed blue lines) is beyond the dashed red line. Right panel: choice of two neighbor candidates (colored blue) that results in a valid vertex (blue dot at the crossing of the dashed blue lines). The two candidates can now be considered neighbors of the central particle. **Bottom row:** left panel: completed Voronoi polygon for the central particle in the presented hexagonal lattice. All points within the polygon are closer to the central particle than to any others. Right panel: example of a square lattice with degenerate vertices. Diagonal neighbors only share a single point of the polygon (black dots). Without modifications, this system is very susceptible to numerical instabilities.

point; such a case may pose a numerical problem (see bottom right panel of Figure 2.10).

Voronoi construction can also be performed for three-dimensional systems; the underlying principle of the algorithm remains the same. However, three-dimensional calculations carry a significantly higher computational cost since intersection points of the now poly*hedra* have to be calculated by intersecting three planes instead of two lines. This leads to an increase in the number of intersection points and thus the required computational effort grows by a factor $\approx N$.

2.4.4. Bond-orientational order parameters: principles

Once we have correctly determined the neighbors of each particle, we can calculate order parameters that quantify the local geometry of a particle's neighborhood. In two-dimensional systems, we follow the formalism of bond-orientational order parameters (BOOPs) [130, 131], in which the order parameters depend only on the relative angles between the neighbors, i.e., between their *bonds* with the central particle. We define the bond angle ϕ_{ij} between a reference axis $\hat{e}_{\mathrm{ref}}$ and the line connecting the central particle i and its neighbor j as

$$\phi_{ij} \quad = \quad \mathrm{acos}\left(\hat{r}_{ij} \cdot \hat{e}_{\mathrm{ref}}\right), \tag{2.55}$$

where $\hat{r}_{ij}$ is the director of the vector connecting particles i and j (see Figure 2.11). We choose the x-axis as the reference axis $\hat{e}_{\mathrm{ref}}$.
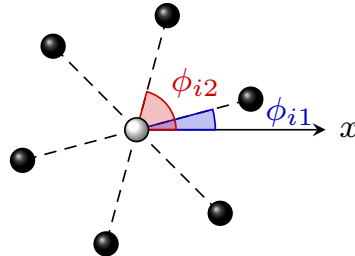

Figure 2.11.: Schematic view of the definition of the bond angles for a hexagonal lattice. Note that the crystal may be rotated with respect to the reference axis.

When calculated for just the central particle, the BOOPs should be able to detect a local n-fold orientational symmetry, i.e., the n-fold BOOP should be large if angles between neighbors are multiples of $2\pi/n$. However, they should also be independent of the arbitrary phase introduced by the choice of the reference axis $\hat{e}_{\mathrm{ref}}$.

The full definition of the local BOOPs [130, 131]

$$\psi_n(i) \;=\; \frac{1}{\mathcal{N}_i} \sum_{j \in \mathcal{N}_i} \exp\left(\imath n \phi_{ij}\right) \tag{2.56}$$

fulfills these criteria by means of a sum of complex numbers. The module of $\psi_n(i)$ reaches its maximum value of unity if all involved bond angles are multiples of $2\pi/n$. The complex phase of $\psi_n(i)$ can be used to check whether the neighborhood of each particle has the same orientation with respect to the reference axis. Since the global BOOPs should be real numbers, we have to calculate the module of $\psi_n(i)$ at some point. There are two possible ways of doing this: the first one is to use

$$\Psi_n \;=\; \frac{1}{N} \left\| \sum_{i=1}^{N} \psi_n(i) \right\|, \tag{2.57}$$

which strongly depends on the complex phase of the local $\psi_n(i)$. We illustrate this with a small example:
- If we consider a unit cell containing a single region with a perfect square lattice, all neighborhoods have the same tilt with respect to the reference axis and $\Psi_4 = 1$.
- However, if the unit cell contains two regions – each with its own perfect square lattice – which are tilted with respect to each other and thus have *different* complex phases, Ψ_4 can be much smaller than unity or even vanish completely.

A second possible definition of the global BOOPs circumvents this behavior by using

$$\Psi_n \;=\; \frac{1}{N} \sum_{i=1}^{N} \left\| \psi_n(i) \right\|. \tag{2.58}$$

Returning to the small example above, we obtain $\Psi_4 \approx 1$ in the second case. In the complete absence of n-fold rotational symmetry, both definitions yield $\Psi_n = 0$.

In this work, we mostly use the second definition (see Equation 2.58), since it better quantifies the local environment of each single particle. Relevant simple crystal structures in two dimensions are either rectangular or hexagonal, i.e., it is definitely worth calculating Ψ_4 and Ψ_6. More complicated patterns may also lead to other non-vanishing $\Psi_n > 0$, i.e., we can use these BOOPs to spot possible occurrences of unconventional lattices. Of particular interest for this work are values of n for which no regular crystal structure exists, e.g., $n = 5$ and $n = 7$. Structures for which Ψ_5 and Ψ_7 are distinctly different from zero may be an indication of structures related to quasicrystals [132].

In three-dimensional systems, BOOPs can conveniently be defined via spherical harmonics [133].

2.4.5. Bond-orientation order parameters: implementation and modifications

As mentioned in Subsection 2.4.3, some ideal crystal lattices may result in a degenerate Voronoi construction. A simple example is the square lattice, with eight nearest neighbors, four of which are degenerate. For numerical reasons, the lattices we deal with are never perfect. As a consequence, the exact number of nearest neighbors can vary, making the BOOPs numerically unstable for even tiny variations in particle position. In addition, BOOPs may change discontinuously when the number of neighbors changes, even though this is difficult to spot when looking at snapshots of structures, where changes appear as continuous.

A simple remedy to overcome this problem is to include in the evaluation of the local BOOPs a weighting factor [134] related to the polygon side length, l_{ij}, that a neighbor j shares with the central particle i

$$\psi_n(i) \;\; = \;\; \frac{1}{\sum_{j \in \mathcal{N}_i} l_{ij}} \sum_{j \in \mathcal{N}_i} l_{ij} \exp\left(\imath n \phi_{ij}\right). \tag{2.59}$$

Since the polygon side lengths associated with degenerate vertices are zero or at least extremely small (see bottom right panel of Figure 2.10), above definition effectively prevents them from contributing substantially to the BOOPs.

2.5. Saddle points: nudged elastic band method

In this section, we discuss how to quantify the transition process of a system between different local minima in the energy landscape and its relevance for our investigations. We first explain what transition paths are (see Subsection 2.5.1) and specify their physical meaning and importance. We then present the nudged elastic band method (see Subsection 2.5.2), a concept that is able to identify transition paths and the associated saddle points and to calculate the related energy barriers. Finally, we give details on our implementation of the method and numerical parameters (see Subsection 2.5.3).

2.5.1. Transition paths

In our implementation of EAs, we effectively deal with an energy landscape characterized by many different local minima and their associated attraction basins. While our aim is to find the global minimum, the meta-stable local minima may also provide valuable information on the system. Whereas the only stable point in the energy landscape at zero temperature is the global minimum, entropic effects at finite temperature allow the exploration of previously meta-stable local minima and their surrounding attraction basins.

For a proper study at finite temperature, a rudimentary knowledge on the transitions between different minima (which we can associate with different structures) is advantageous; understanding how one structure transforms into another and estimating the involved energy barrier can help us study phase transitions at finite temperature. In particular close to first order phase transitions, where two different structures are characterized by the same free energy, a rough estimate of the energy barrier can help us to properly carry out simulations and identify interesting temperature and parameter ranges.

2.5.2. Nudged elastic band method

Determining the transition mechanism and transition probability between two local minima in a complex energy landscape is not a simple task since we have to deal with a high-dimensional parameter space and a multitude of different transition paths between two minima. In this work, we are only interested in the transition path with the lowest energy barrier. Although this is not necessarily the only path contributing to a transition, knowing the size of the involved energy barrier can be useful for choosing the temperature in finite temperature simulations.

The nudged elastic band (NEB) method [135, 136] is based on the knowledge of two local minima in the energy landscape. In order for the algorithm to converge, these minima should be rather "close" to each other in the d-dimensional search space. We define the d-dimensional vectors of the two minima $\boldsymbol{a}$ and $\boldsymbol{b}$ via their coordinates in search space. Any sequence of points connecting $\boldsymbol{a}$ and $\boldsymbol{b}$ is called a path $\boldsymbol{q}$.

The left panel of Figure 2.12 shows a schematic view of a simple two-dimensional energy landscape with two local minima separated by an energy barrier. All possible paths $\boldsymbol{a} \to \boldsymbol{b}$ are characterized by an associated energy barrier. We define the scalar *reaction coordinate* $r \in (0, 1)$ [136] as the position of a point $\boldsymbol{q}(r)$ along the path, with $\boldsymbol{q}(r = 0) = \boldsymbol{a}$ corresponding to the start- and $\boldsymbol{q}(r = 1) = \boldsymbol{b}$ to the end-point, respectively. Note that the reaction coordinate itself does not have a direct physical meaning.

The NEB method is based on approximating a path $\boldsymbol{q}(r)$ by a chain of $(n + 1)$ points $\boldsymbol{q}_i = \boldsymbol{q}(r = i/n)$ (with $0 \leq i \leq n$), which are equally spaced in r, but not necessarily in search space. We can calculate the force, $\boldsymbol{F}(\boldsymbol{q})$, acting on each of these points along the chain from our analytical knowledge of the energy functional $E(\boldsymbol{q})$:

$$\boldsymbol{F}(\boldsymbol{q}) \;=\; -\boldsymbol{\nabla} E(\boldsymbol{q}). \tag{2.60}$$

These physical force points towards the local minimum of the respective attraction basin. The key idea in the NEB approach [136] is to neglect the component of this gradient *along* the chain and to add springs *within* the chain (see center panel of Figure 2.12)

$$\boldsymbol{F}_{\text{eff}}(\boldsymbol{q}_i) \;=\; \boldsymbol{F}(\boldsymbol{q}_i) - [\boldsymbol{F}(\boldsymbol{q}_i) \cdot \hat{\boldsymbol{e}}_{\text{chain}}(\boldsymbol{q}_i)] \, \hat{\boldsymbol{e}}_{\text{chain}}(\boldsymbol{q}_i) + k \left(\boldsymbol{q}_{i+1} - 2\boldsymbol{q}_i + \boldsymbol{q}_{i-1}\right), \tag{2.61}$$

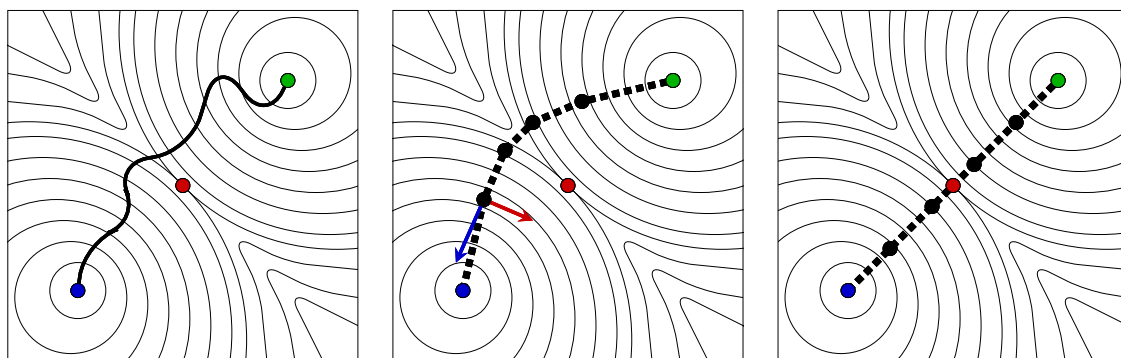Figure 2.12.: Schematic view of a simple two-dimensional energy landscape with two local minima: a (blue circle) and b (green circle) are separated by an energy barrier (indicated by isopotential lines), which assumes its lowest value at the saddle point (red circle). Left panel: a possible path connecting start- and end-point $a \rightarrow b$ is shown. Center panel: the transition path is approximated by a chain of points (black circles) in the NEB algorithm. The force calculated as gradient of the potential (blue arrow orthogonal to the isopotential lines) is split into a component *along* the direction of the chain (the chain direction is indicated by the dashed black line) and one *orthogonal* to it; the former component is replaced by a spring force along the chain (see Equation 2.61). The resulting effective force (red arrow) moves the chain towards the transition path passing through the saddle point. Right panel: when the chain has converged, it passes through the saddle point.

where the spring constant k is a parameter of the algorithm. The definition of the chain direction

$$\hat{\boldsymbol{e}}_{\mathrm{chain}} \;=\; \frac{\boldsymbol{\tau}}{|\boldsymbol{\tau}|} \tag{2.62}$$

depends on how the values of E_{i+1}, E_i, and E_{i-1} are related. We obtain six different cases

$$\begin{aligned}
E_{i-1} < E_i < E_{i+1} & \quad \boldsymbol{\tau} = \boldsymbol{\tau}_i^+ \\
E_{i+1} < E_i < E_{i-1} & \quad \boldsymbol{\tau} = \boldsymbol{\tau}_i^- \\
\left.\begin{array}{c} E_i < E_{i-1} < E_{i+1} \\ E_{i-1} < E_{i+1} < E_i \end{array}\right\} & \quad \boldsymbol{\tau} = \boldsymbol{\tau}_i^+ \Delta E_i^{\mathrm{max}} + \boldsymbol{\tau}_i^- \Delta E_i^{\mathrm{min}} \;, \\
\left.\begin{array}{c} E_{i+1} < E_{i-1} < E_i \\ E_i < E_{i+1} < E_{i-1} \end{array}\right\} & \quad \boldsymbol{\tau} = \boldsymbol{\tau}_i^+ \Delta E_i^{\mathrm{min}} + \boldsymbol{\tau}_i^- \Delta E_i^{\mathrm{max}}
\end{aligned} \tag{2.63}$$

where

$$\begin{aligned}
\boldsymbol{\tau}_i^+ &= \boldsymbol{q}_{i+1} - \boldsymbol{q}_i & (2.64) \\
\boldsymbol{\tau}_i^- &= \boldsymbol{q}_i - \boldsymbol{q}_{i-1} & (2.65) \\
\Delta E_i^{\mathrm{max}} &= \max\left(\left|\mathrm{E}(\mathrm{q_{i+1}}) - \mathrm{E}(\mathrm{q_i})\right|, \left|\mathrm{E}(\mathrm{q_{i-1}}) - \mathrm{E}(\mathrm{q_i})\right|\right) & (2.66) \\
\Delta E_i^{\mathrm{min}} &= \min\left(\left|\mathrm{E}(\mathrm{q_{i+1}}) - \mathrm{E}(\mathrm{q_i})\right|, \left|\mathrm{E}(\mathrm{q_{i-1}}) - \mathrm{E}(\mathrm{q_i})\right|\right). & (2.67)
\end{aligned}$$

The component of the force orthogonal to the chain (see center panel of Figure 2.12) points towards the transition path with the lowest energy barrier. The springs keep the chain roughly equally spaced in search space. The start- and end-points are kept fixed; this allows relaxation of the chain to yield the desired transition path, which passes through the saddle point (see right panel of Figure 2.12).

2.5.3. Implementation and numerical parameters

We use particle configurations to generate the start-point $\boldsymbol{a}$ and the end-point $\boldsymbol{b}$; for the initialization of the chain, we keep with the common practice [136] of linearly interpolating the chain points between $\boldsymbol{a}$ and $\boldsymbol{b}$ in search space. However, this may be troublesome for some systems – e.g., if particles overlap due to the interpolation – and more complicated methods may be required [137]. In this work, we only study rather "simple" transitions, i.e., interpolation of the chain between $\boldsymbol{a}$ and $\boldsymbol{b}$ is to some extent already a viable transition path. Such simple transitions do not require a large number of chain points to model correctly; we commonly use $(n + 1) = 21$ chain points.

We can justify the appropriateness of this choice by verifying that we do not miss any significant features of the energy landscape with this number of points by linearly interpolating between neighboring points of the chain and plotting the energy: if we do not use a sufficient number of points, "bumps" in $E(\boldsymbol{q})$ appear between neighboring points in the chain, indi-

cating additional – true or artifical – barriers along the chain; these features can be missed if the distances in parameter space between chain points is too large. On the other hand, it is of course advantageous to keep the number of chain points as small as possible in an effort to improve convergence speed.

The numerical value for the spring constant used in the algorithm is set to $k = 500$. We consider the transition path converged when the total forces acting on the chain are smaller than 10^{-5}. Interpolation between chain points (after the algorithm has converged) allows us to compute the barrier height more accurately without much additional computational effort.

Note that due to the modifications to the forces acting on a point (see Equation 2.61), it is difficult to calculate second derivatives; there is also no conservative potential. As a result, most higher-order gradient descent methods are inadequate in their common implementations and we use a simple gradient descent method for relaxation of the chain.

3. Systems

In this chapter, we present the different systems we studied and the results we obtained.

We start with a simple long-ranged system, for which exact analytical results are available: the classical Wigner[1] monolayer system. These results are useful as a benchmark for our implementation of Ewald summation, which we use to properly treat long-ranged interactions (see Section 2.1). We then extend the model of the classical Wigner monolayer to an equimolar binary mixture of charges (see Section 3.1).

Our next goal is to study the transition from the purely two-dimensional Wigner monolayer to a Wigner bilayer system. A first step in this endeavour is to investigate the effects of vertically displacing a single charge from the monolayer (see Section 3.2).

The next step is the symmetric Wigner bilayer crystal, which provides another benchmarking system for both global optimization and energy calculation, as exact analytical results are available. We eventually put forward the complex system of the asymmetric Wigner bilayer crystal, which incorporates many of the effects and limiting cases we have observed in preceding systems (see Section 3.3). We also compare our results to data obtained in high-precision analytical calculations and find good agreement.

In the last section, we consider anisotropic interactions based on quadrupole moments. We develop a simple model for organic molecules, based on linear quadrupole moments that are embedded in soft ellipsoids. Confining such particles to a plane provides us with a computationally sufficiently simple model, which nevertheless captures the essential features of realistic systems and exhibits interesting effects (see Section 3.4). We also discuss useful order parameters that can be used to characterize the positional and orientational order of similar systems.

Each of the following sections is organized as follows:
- We first give a short introduction to the respective system and detail its relevance for related models and experimental systems.
- We then describe the particular model and give some computational details outlining our approach.
- We also give some general theoretical considerations on the system and discuss measured quantities and order parameters if required.
- We discuss the results and – if possible – compare them to data obtained via different approaches.

---

1. Wigner systems are crystalline phases of electrons, first predicted by Eugene Wigner [138]. They consist of a system of point charges and a uniform neutralizing background and can only be observed at low temperature and low density, where the electrostatic interactions between electrons dominate over kinetic energy and entropy.

- We conclude by summarizing the results and outlining possible future studies.

3.1. Equimolar binary mixture of point charges confined to a plane

3.1.1. Introduction and motivation

In order to verify and optimize our implementation of Ewald summation (see Section 2.1), we require a simple long-ranged system for which exact analytical data is available. Such a system can serve as a stepping stone for further studies on more complicated systems as we may first observe interesting phenomena such as small energy differences between competing structures.

One possible system that fulfills the requirements outlined above is the monolayer Wigner crystal [138], i.e., a periodic arrangement of classical point charges with a neutralizing background. At zero temperature, the ground state of such a crystal is a simple hexagonal (equilateral triangular) lattice. The energy of this configuration is given by

$$E_{\text{hex}} \quad = \quad c_{\text{m}} \sqrt{\rho} Q^2, \tag{3.1}$$

where $c_{\text{m}} = -1.960515789$ is the *Madelung constant* of the hexagonal lattice, which has been calculated with high accuracy [139]. Its numerical value is thus known with extremely high precision; comparing our results obtained by Ewald summation with this reference yields very good agreement of $\delta < 10^{-6}$ (see also Figure 2.4).

3.1.2. Model and approach

The model for a monolayer Wigner crystal is the same as the one we used to demonstrate the derivation of Ewald summation (see Section 2.1). We assume a three-dimensional space filled with classical point charges Q_i (see left panel of Figure 3.1). The system has to fulfill global electro-neutrality

$$\int_{\mathbb{R}^3} \sigma(\boldsymbol{r}) d\boldsymbol{r} + \sum_i Q_i \quad = \quad 0; \tag{3.2}$$

here $\sigma(\boldsymbol{r})$ is the neutralizing background, which we assume as uniform and planar (located in the $z = 0$ plane)

$$\sigma(\boldsymbol{r}) \quad = \quad \sigma \delta(z) \tag{3.3}$$

$$\sigma \int_0^\infty 2\pi r dr + \sum_i Q_i \quad = \quad 0. \tag{3.4}$$

At zero temperature, all of the point charges condense on the neutralizing plane ($z = 0$) due to Earnshaw's theorem [140], which states that a system of point charges cannot form a stable equilibrium system when interacting solely via electrostatic potentials, thus effectively forming a two-dimensional system (see center panel of Figure 3.1). However, we emphasize that the system is still *inherently* three-dimensional, i.e., charges interact via the Coulomb interaction

$$V_{\text{Coulomb}}(r) \quad = \quad \frac{Q_i Q_j}{r}. \tag{3.5}$$

Again, we assume that the system is periodic, yielding the same expressions for the energy as in Section 2.1 (see Equations 2.29, 2.30, and 2.31). For any configuration, the dependence of the energy on the density is the same as in the hexagonal monolayer (see Equation 3.1)

$$E \quad \sim \quad \sqrt{\rho}Q^2. \tag{3.6}$$
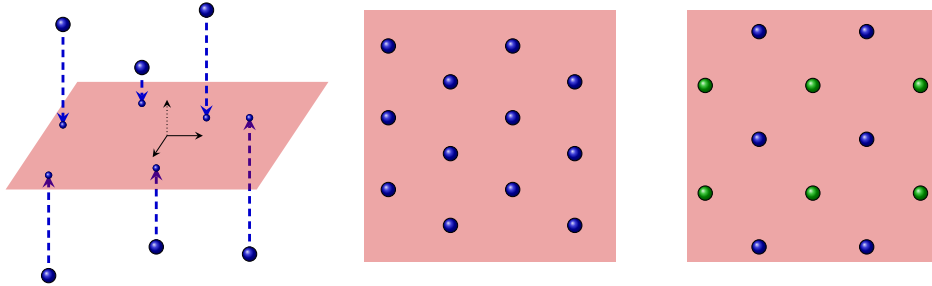
Figure 3.1.: Left panel: schematic view of the model for the monolayer Wigner crystal. The system consists of classical point charges (blue spheres) and a uniform planar neutralizing background (red plane). Center panel: at zero temperature, all charges condense on the neutralizing background due to Earnshaw's theorem. The system thus becomes effectively planar (two-dimensional) and forms a hexagonal lattice. Right panel: the introduction of two species of charges (blue and green spheres) creates complexity in the system.

In principle, we can use the above model to describe real charged colloids in confinement [141, 142] or for electrons at the surface of liquid helium [143]. However, since we do not consider short-range non-Coulombic interactions (e.g., between the colloids), this theoretical model is only applicable in the dilute case and even there, screening effects due to the dielectric properties of the solvent and to counter-ions are likely to lead to differences in experimental set-ups. Another important feature in realistic systems is polydispersity of the particles, i.e., their size and the associated charge follows a certain distribution [144, 145]. In this work, we want to investigate the most basic effects of polydispersity on the formed structure; we therefore study a binary mixture with two species of charges (Q_1 and Q_2) and with partial densities (ρ_1 and ρ_2). To further reduce the parameter space, we study an equimolar mixture, i.e., $\rho_1 = \rho_2 = \rho/2$ (see right panel of Figure 3.1). This leaves us

with just a single free parameter of the system (assuming that $Q_1 = Q$), namely the charge strength ratio

$$q = \frac{Q_2}{Q_1} = \frac{Q_2}{Q}. \tag{3.7}$$

Since the system would collapse for $q < 0$, we can limit the interesting range of q to

$$0 \leq \; q \; \leq 1. \tag{3.8}$$

Considering the range $q > 1$ is equivalent, due to the symmetry $q \leftrightarrow 1/q$.

In our efforts to determine the ground state over the entire interesting range of q, we perform EA calculations for 101 equally spaced values of q ranging from $q = 0$ to $q = 1$. Due to Equation 3.6, the nominal particle density can be scaled out of the results, i.e., we consider the reduced energy

$$E^* \;\; = \;\; \frac{E}{\sqrt{\rho}Q^2}. \tag{3.9}$$

We run our optimization tool for $N = 2 - 40$ particles per cell and consider the output of the run with the lowest reduced energy per particle E^* as the final result.

3.1.3. Theory and order parameters

Since the Coulomb interaction is long-ranged, we can expect the energy differences between competing structures, and thereby also the influence of the particle arrangement on the energy, to be small. Therefore, it is useful to introduce a *reference* energy $E_{\text{ref}}(q)$, depending solely on q; $E_{\text{ref}}(q)$ should be related to an actual configuration. A very simple way to introduce such an $E_{\text{ref}}(q)$ is to assume a de-mixing scenario of the two species of charges (see Figure 3.2).

For this scenario, we assume that the two species of charges form two separate crystal regions with hexagonal particle arrangement. Furthermore, we assume that both regions are locally electro-neutral. This allows us to neglect higher-order interactions between the two crystal regions. The boundary region between the two crystal parts (where the lattice is significantly distorted) has only a finite width[2], thus its influence on the total energy per particle can be neglected as well.

We can now calculate the partial number densities of the two species in region 1

$$\rho_1^{(1)} = \frac{1+q}{2}\rho \qquad\qquad \rho_2^{(1)} = 0, \tag{3.10}$$

---

2. While still infinitely large in the direction along the boundary, the finite width of the boundary region makes its total area incomparably smaller than the remaining two crystal regions, each of which is also infinitely large in the direction orthogonal to the boundary.
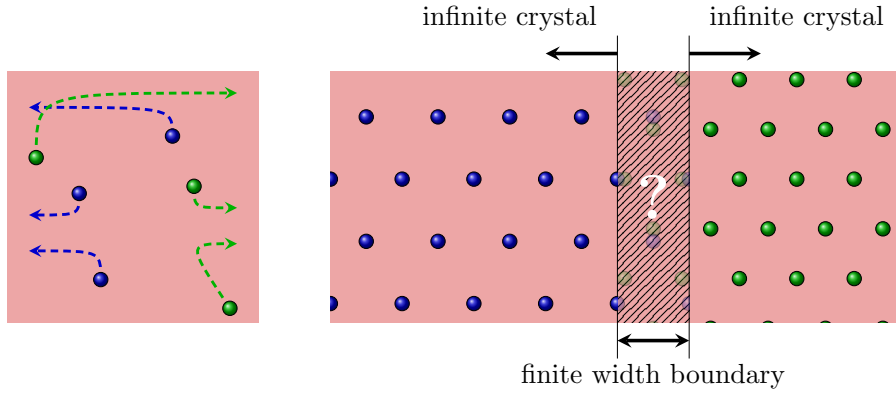
Figure 3.2.: Schematic view of the simplest phase separation scenario of a binary mixture (complete de-mixing). Left panel: the crystal de-mixes completely into two parts populated only by a single species each. Right panel: both species form infinite hexagonal crystals, which are locally electro-neutral. As a consequence, the crystal formed by the stronger charges (here blue spheres) is larger, but has a lower number density (evidenced by a larger lattice constant). The border region is of finite width, thus of no relevance for the overall energy per particle of the infinitely large crystal.

which fulfills electro-neutrality $\rho_1^{(1)}Q + \sigma = 0$. Correspondingly, we obtain for region 2

$$\rho_1^{(2)} = 0 \qquad\qquad \rho_2^{(2)} = \frac{1+q}{2q}\rho, \qquad\qquad (3.11)$$

where $\rho_2^{(2)}qQ + \sigma = 0$. Since we already know the Madelung constant of the hexagonal arrangement, we can now calculate the energy per particle in both crystal regions. As both regions contain the same number of particles, the total energy per particle $E_{\text{ref}}(q)$ is just the average of the two

$$E_{\text{ref}}(q) = c_{\text{m}}N\left[\frac{1}{2}\sqrt{\rho_1^{(1)}}Q^2 + \frac{1}{2}\sqrt{\rho_2^{(2)}}q^2Q^2\right] \qquad\qquad (3.12)$$

$$= Nc_{\text{m}}\sqrt{\rho}Q^2\sqrt{\frac{1+q}{2}}\frac{1+q^{3/2}}{2}. \qquad\qquad (3.13)$$

Further, we know which structures to expect for the two limiting cases $q \to 1$ and $q \to 0$:
(i) In the former case, we obtain a simple one-component hexagonal Wigner monolayer.
(ii) In the latter case, the weaker charges completely cease to interact, thus forming an ideal gas, whose contribution to the energy we can disregard at zero temperature. The stronger charges therefore form a hexagonal Wigner monolayer, but with a larger lattice spacing than in case (i).

In both cases, it is interesting to quantify the hexagonal symmetry of the particle arrangement. We therefore measure the six-fold BOOP Ψ_6 (see Subsection 2.4.4 – albeit without the

side-length modification) and the distortions of the lattice formed by the stronger charges.

3.1.4. Results

The left panel of Figure 3.3 shows the reduced ground state energy curve $E^*(q)/N = E(q)/N\sqrt{\rho}Q^2$ obtained with our optimization tool for the entire relevant range $0 \le q \le 1$. $E^*(q)$ decreases monotonously with increasing q, connecting the limiting values $q = 0$ and $q = 1$. For $q = 0$, the weaker charges do not interact at all, behaving like an ideal gas. The stronger charges thus form a hexagonal lattice (see top left panel of Figure 3.4) with density $\rho_1 = \rho/2$; thus the energy per particle [3] is simply $E^*(q = 0)/N = c_{\mathrm{m}}/2\sqrt{2}$. In the second limiting case, $q = 1$, all charges are indistinguishable and the ground state structure is the Wigner monolayer, thus $E^*(q = 1)/N = c_{\mathrm{m}}$ (see bottom right panel of Figure 3.4). Note that for both limiting cases $E^*(q) = E^*_{\mathrm{ref}}(q)$.

At first glance, $E^*(q)/N$ appears to be a completely smooth function of q, offering no insight into possible structural transitions. While the different observed structures are discussed later, we first focus on the energy curve itself. We can radically improve the readability of this curve by subtracting from $E^*(q)$ the reference energy $E^*_{\mathrm{ref}}(q)$, introduced in Subsection 3.1.3. The resulting curve $\Delta E^*(q)/N$ now displays a rich variety of features (right panel of Figure 3.3), which are by approximately three orders of magnitude smaller than the total energy per particle.

We emphasize that this observation is typical of systems with long-ranged interactions: a significant part of the energy is independent of the particular structure of the particle arrangement, partly due to the interaction with the neutralizing background. The fact that the total energy and the relative energy differences between competing structures differ by several orders of magnitude indicates that very high precision in the energy calculation is required for a correct treatment of long-ranged systems.

$\Delta E^*(q)$ is non-monotonous and shows kinks corresponding to transitions between different observed structures (indicated by different colors in the right panel of Figure 3.3). We observe six different stable ground state structures, which are discussed below. We also immediately observe that for $q \ge 0.6$ the energy of the phase separation scenario $E^*_{\mathrm{ref}}(q)$ is lower than the results obtained with the EA tool, indicating that the system undergoes phase separation in this q-range. We can thus discard the structures obtained in this region.

Table 3.1 provides an overview of the ground state configurations identified for $0 \le q \le 1$. The corresponding structures (including the limiting cases $q = 0$ and $q = 1$) are depicted in Figure 3.4.

For **0.00 = q**, the weaker charges vanish, leaving only the stronger charges Q_1 with density $\rho_1 = \rho/2$. These form a hexagonal lattice (see top right panel of Figure 3.4).

---

3. Although the weaker charges Q_2 in this case do not contribute to the energy, they are still considered for the total number of particles.
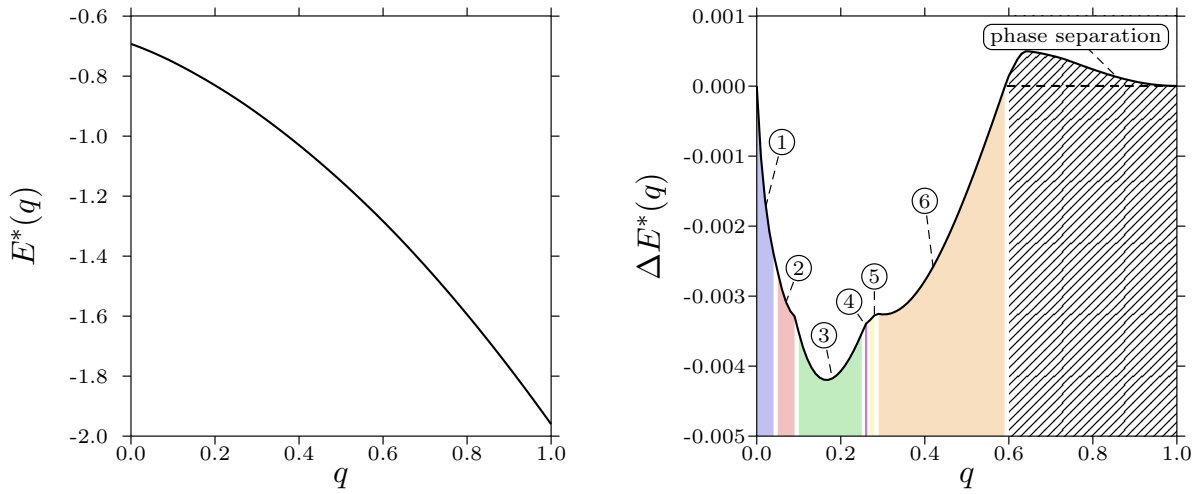
Figure 3.3.: Left panel: ground state energy $E^*(q)/N$ of the equimolar binary mixture Wigner crystal as a function of q. The energy per particle is given in units of $\sqrt{\rho}Q^2$. The curve exhibits no identifiable features to the naked eye. Both limiting cases $q \to 1$ and $q \to 0$ yield well-known results. Right panel: after subtraction of the phase separation reference energy $E^*_{\text{ref}}(q)$, a variety of features emerges in $\Delta E^*(q)/N$, indicating the occurrence of transitions between different structures (labelled 1 through 6 and indicated by colored regions). Note that relevant energy differences are by about three orders of magnitude smaller than the total energy per particle. For $Q \geq 0.6$, we obtain energies larger than $E_{\text{ref}}(q)$, indicating the occurrence of phase separation (hatched region).
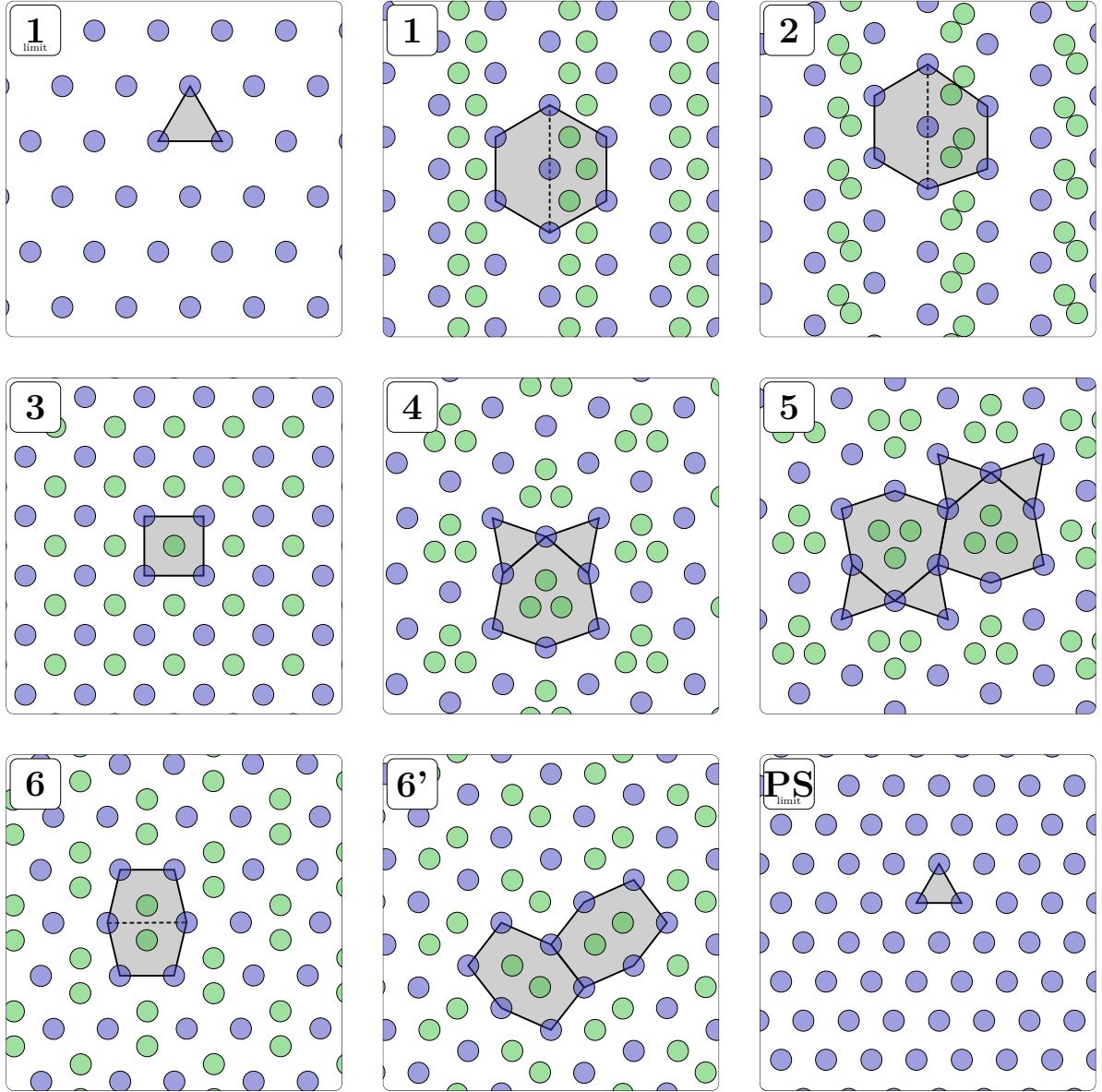
Figure 3.4.: Snapshots of the equimolar binary Wigner mixture. Strong/weak charges are colored blue/green. Interesting structural features are indicated by shaded areas. **Top row:** left panel: hexagonal structure in the limiting case for $q = 0$. Center panel: structure 1 for $q = 0.02$. Right panel: structure 2 for $q = 0.05$. **Center row:** left panel: structure 3 for $q = 0.10$. Center panel: structure 4 for $q = 0.26$. Right panel: structure 5 for $q = 0.27$. **Bottom row:** left panel: structure 6 for $q = 0.30$. Center panel: structure 6' for $q = 0.35$. Right panel: hexagonal structure in the limiting case of the phase separation scenario (PS) for $q = 1$.

Table 3.1.: Overview of the observed ground state structures of the equimolar binary mixture Wigner crystal and their respective stability ranges (see also Figure 3.4).

q-range	ground state structure
$0.00 = q$	hexagonal lattice formed by strong charges Q_1
	limiting case of structure 1
$0.00 < q \lesssim 0.04$	structure 1
$0.05 \lesssim q \lesssim 0.09$	structure 2
$0.10 \lesssim q \lesssim 0.25$	structure 3
$0.26 \simeq q$	structure 4
$0.27 \lesssim q \lesssim 0.28$	structure 5
$0.29 \lesssim q \lesssim 0.59$	structure 6
$0.60 \lesssim q < 1.00$	phase separation
$1.00 = q$	hexagonal lattice formed by indistinguishable charges $Q_1 = Q_2$
	limiting case of phase separation

For **$0.00 < q \lesssim 0.04$**, the stronger charges form a slightly distorted hexagonal lattice (**structure 1**, depicted in the top center panel of Figure 3.4). The order parameter Ψ_6 (see Subsection 2.4.4) varies between $\Psi_6(q = 0.01) = 0.99972$ and $\Psi_6(q = 0.04) = 0.99577$. The distortion of the hexagonal lattice is due to the presence of the weaker charges, which are hosted in a zig-zag arrangement in the centers of triangles formed by the stronger charges. For easier analysis, we can split the hexagonal structural units (shaded gray) of the crystal in two parts separated by a central axis (indicated by a dashed blue line). The distances between blue particles in the part hosting the weaker charges are enlarged by about $+4\%$ (with respect to a perfect hexagonal lattice), while they are reduced by about -3% in the other part.

For **$0.05 \lesssim q \lesssim 0.09$**, the stronger charges maintain their hexagonal lattice but distortions are now more strongly pronounced. The order parameters range from $\Psi_6(q = 0.05) = 0.90598$ to $\Psi_6(q = 0.09) = 0.83643$. Again, we can split the hexagonal structural units into two parts, one of which remains empty and slightly contracted by about -5%. The weaker charges are no longer hosted in the centers of triangles but instead move closer to bridge sites, forming pairs (**structure 2**, depicted in the top right panel of Figure 3.4). The distortion in the part hosting the weaker charges is asymmetric, some distances increasing by up to $+21\%$. At first look, it appears counter-intuitive that the intra-pair distances between weak charges should decrease with increasing q (the interaction between them scales as $\sim q^2$), but distances between weak and strong charges (where the interaction scales as $\sim q$) increase slightly.

For **$0.10 \lesssim q \lesssim 0.25$** we observe two intertwining, commensurate square lattices (**structure 3**, depicted in the center left panel of Figure 3.4). This structure appears to be very stable, evidenced by the large q-range in which it is observed and by its high energy gain ΔE^* (see right panel of Figure 3.3).

For **$0.26 \simeq q$** the stronger charges form hexagonal structural units which are in their shape

reminiscent of gems or diamonds. These rings host in their center a triplet of weak charges. The structural units form head-to-tail *parallel* lanes, with neighboring units sharing single vertices (**structure 4**, depicted in the center panel of Figure 3.4). Note that distances between neighboring strong charges are almost identical, indicating that this remains the dominant interaction in the system.

For **0.27 $\lesssim q \lesssim$ 0.28** we observe a particle arrangement similar to structure 4. However, the structural six-particle units now form *antiparallel* lanes, where structural units from neighboring lanes share two vertices (**structure 5**, depicted in the center right panel of Figure 3.4).

For **0.29 $\lesssim q \lesssim$ 0.59** we observe an arrangement based on intertwined elongated hexagonal lattices (**structure 6**, depicted in the bottom left panel of Figure 3.4). The stronger charges form elongated hexagons hosting two weaker charges each; the weaker charges in turn form rather strongly distorted hexagons containing two stronger charges each. For an easier analysis, we can again define an axis in each structural unit and observe that the side lengths of the hexagon parallel to the axis increases in length as q is increased. For $q = 0.29$ this length $l_2(q = 0.29) = 1.29/\sqrt{\rho}$ is shorter than the other side length $l_1(q = 0.29) = 1.297/\sqrt{\rho}$, but this situation is reversed at larger q, i.e., $l_2(q = 0.59) = 1.324/\sqrt{\rho}$ and $l_1(q = 0.59) = 1.269/\sqrt{\rho}$. Close to the crossover, where $l_1 = l_2$, we also observe a different variant, where the structural units arrange in a herringbone pattern (denoted **structure 6'**, depicted in the bottom center panel of Figure 3.4).

For **0.60 $\lesssim q <$ 1.00** we find that $E^*_{\mathrm{ref}}(q) < E^*(q)$, indicating that **phase separation** (PS) is energetically favorable. Some of the configurations obtained with the EA in this region already indicate this behavior, though their accuracy is marred by the finite system size. The two species form separate infinite hexagonal crystals which observe local electro-neutrality.

For **1.00 $= q$** we again obtain a hexagonal particle arrangement. In this case, the two species are indistinguishable and form the simple hexagonal Wigner monolayer. This is also the limiting case of the phase separation scenario (see bottom right panel of Figure 3.4).

3.1.5. Conclusions and outlook

In summary, we have been able to verify the high accuracy of our implementation of the Ewald summation technique by considering the hexagonal Wigner monolayer as a benchmarking system. In addition, we have proved the compatibility of the treatment of long-ranged interactions with Ewald summation and the global ground state search with EAs. For the simple equimolar binary mixture of charges studied in this section, we have been able to identify six different structures, some of which show remarkable structural complexity. By introducing a reference energy derived from a phase separation scenario, we were able to extract the effective influence of competing structures on the total energy of the system. We have observed that these energy differences are by about three orders of magnitude

smaller than the total energy. This fact is most likely due to the long-ranged nature of the interaction. In addition, we have identified a region where phase separation was favorable compared to any of the structures obtained with our EA tool.

The results presented in this section were published in [146].

For future work, it would be interesting to study the system for different molar fractions, i.e., $\rho_1 \neq \rho_2$. The results obtained from such an investigation could be used for the study of more complicated phase separation scenarios beyond a simple de-mixing; this could possibly improve the phase diagram presented in this work.

3.2. Removing a single charge from a Wigner monolayer

3.2.1. Introduction

In Section 3.1, we have verified the treatability of long-range interactions within the EA approach. In our study of a simple system of point charges, we have obtained useful information on the relevant energy differences. As we have seen, the one-component Wigner system is trivial at zero temperature, forming a simple hexagonal (equilateral triangular) lattice [139]. In this section, we combine our experience in studying systems of point charges confined to a plane with interesting properties of quasi-two-dimensional geometries.

In particular, we are for the moment interested in the process of removing a single charge from a Wigner monolayer, i.e., on how this vertical displacement influences the two-dimensional structure of the remaining crystal. This process is related to the formation of a bilayer system, which we will investigate in Section 3.3.

We can further relate our idealized model to more specialized studies on the interaction of asymmetrically charged surfaces [147] or on the rearrangement of charge carriers on the surface of a colloid in the presence of another colloid [148].

3.2.2. Model and approach

Our model consists of classical point charges confined to a plane; they have a charge Q and a number area density ρ. The plane which they are confined to is infinitely large and contains a uniform neutralizing background $\sigma = -Q\rho$. In addition, we add one more charge to the set-up, which is displaced vertically by a distance h from the plane (see Figure 3.5). Without loss of generality, we assume that this displaced charge – which we denote the *tagged* charge – is positioned at $x = y = 0$. The only relevant length scale in the monolayer crystal is
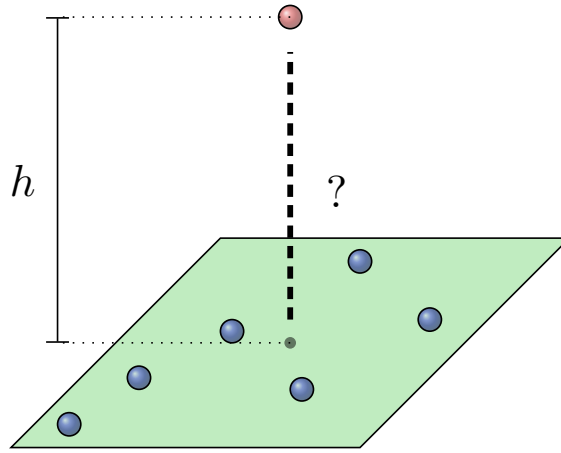
Figure 3.5.: Schematic view of the Wigner monolayer (blue spheres) when vertically displacing a single charge (denoted "tagged" charge; red sphere) by a distance h. This process is energetically unfavorable, leading to a positive energy of the defect. Charges in the layer rearrange to compensate for the displacement of the tagged charge.

determined by ρ; we can thus introduce the dimensionless displacement

$$\eta \;=\; h\sqrt{\frac{\rho}{2}}. \tag{3.14}$$

The factor $1/\sqrt{2}$ may appear arbitrary, but allows us to relate our results to previous work presented in [149, 150]. For comparison, the lattice constant of the hexagonal Wigner monolayer is

$$a_{\text{hex}} \;=\; \sqrt{\frac{2}{\sqrt{3}\rho}} \tag{3.15}$$

$$\left(\frac{h}{a_{\text{hex}}}\right)^2 \;=\; \sqrt{3}\eta^2. \tag{3.16}$$

Thus, $h > a_{\text{hex}}$ for $\eta > 0.760$. Our main interest lies in the structural changes the layer undergoes as we vary the displacement η.

Two limiting cases are immediately obvious:

$\boldsymbol{\eta \to 0}$: If the tagged charge is not displaced at all, we obtain a simple hexagonal Wigner monolayer. Therefore, we expect that for very small displacements, the vertical projection of the position of the tagged charge will be at the center of a hexagonal hole in the layer. The particles in the layer (*including* the projection of the tagged charge) form a

perfect hexagonal (equilateral triangular) lattice. We denote configurations based on this archetype as the "out"-branch (see left column in Figure 3.6). For finite values of η, the hexagonal lattice will deform slightly in order to reduce its energy; in the simplest case, i.e., for very small η, this deformation is merely a contraction of the hexagonal hole in the layer (see bottom left panel of Figure 3.6).

$\boldsymbol{\eta \to \infty}$: Positioning the tagged charge very far away from the layer (i.e., ionizing the layer) again recovers a perfect hexagonal Wigner monolayer, i.e., the crystal rearranges completely to compensate for the missing charge. Therefore, we predict that for very large displacements, the vertical projection of the position of the tagged charge will be at the center of a triangle in the layer. The particles in the layer (*excluding* the projection of the tagged charge) form a perfect hexagonal (equilateral triangular) lattice. We denote configurations based on this archetype as the "in"-branch (see right column in Figure 3.6). For finite values of η, the hexagonal lattice will deform slightly in order to reduce its energy; in the simplest case, i.e., for very large η, this deformation is merely an expansion of the triangle in the layer surrounding the projection of the tagged charge (see bottom right panel of Figure 3.6).

Our approach for studying the system is three-pronged. In all three approaches, the interesting thermodynamical quantity is the *defect* energy δE^*, which we define as the energy penalty for the formation of the defect with respect to the unperturbed hexagonal Wigner monolayer, i.e.,

$$\delta E^* \quad = \quad E^*(\eta, N) - N c_{\mathrm{m}}. \tag{3.17}$$

The first approach is based on analytical calculations performed by Ladislav Šamaj and Emmanuel Trizac [149, 150]. Their method directly optimizes candidate configurations in order to study energies and deformations along the "out"- and the "in"-branches with extremely high accuracy. However, due to the complexity of the involved energy terms, only a limited number of deformations can be considered for the two branches. Figure 3.6 shows what types of deformations can be taken into account for the two considered branches in the analytical approach.

Our other two approaches are numerical and use Ewald summation for accurate treatment of the long-ranged interactions. Since the system we have described so far is *non*periodic, it is obviously incompatible with Ewald summation, which assumes periodicity. We thus approximate the nonperiodic system with a periodic system with an appropriately large unit cell. In particular, we want to keep interactions between periodic replicas of the tagged charge and its surroundings in the layer (denoted the *defect*) as small as possible. Since the deformations of the lattice caused by the tagged charge are also a concern, our cell should be sufficiently large such that the deformations of neighboring cells do not compensate each other.

The unit cell contains a total number N of charges, only one of which is vertically displaced.
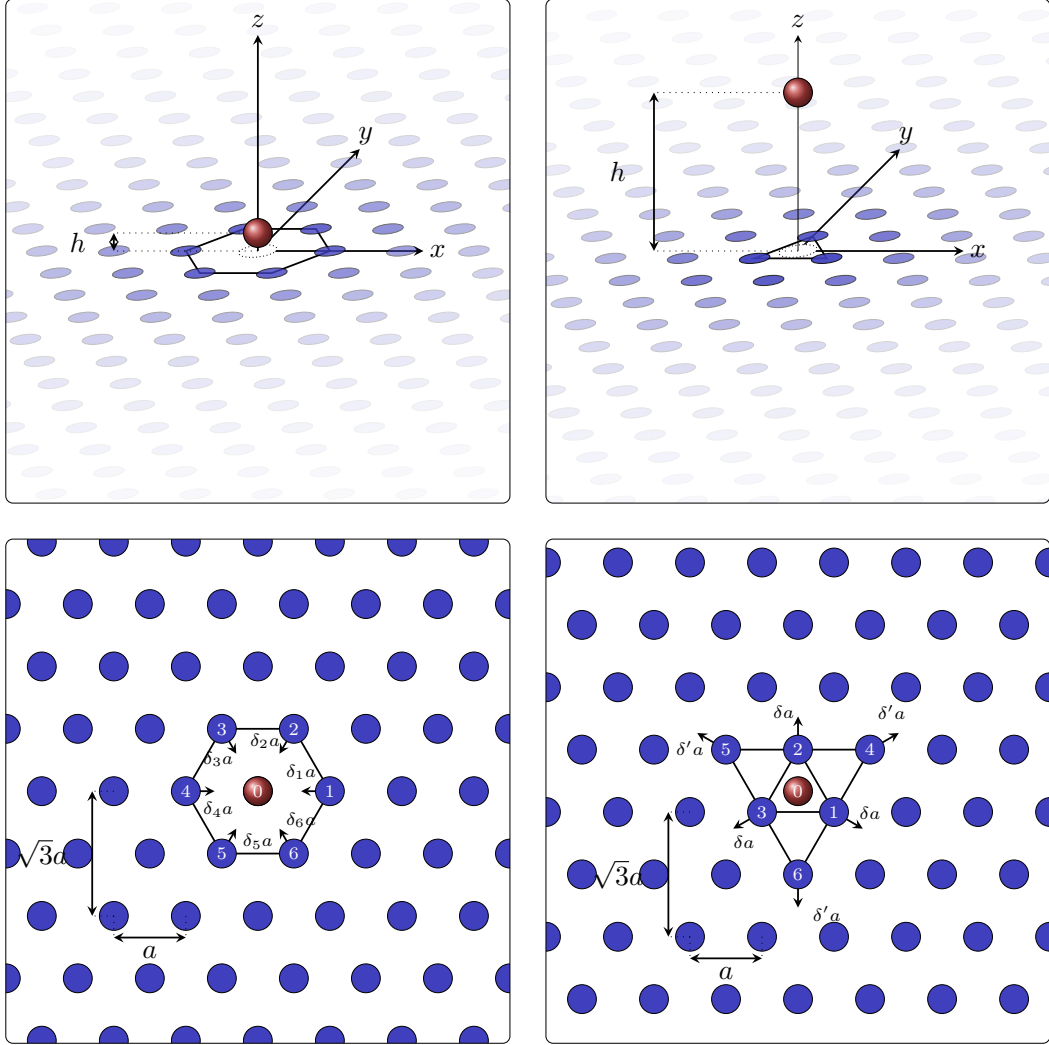
Figure 3.6.: Schematic representation of the two considered branches. **Left column:** top panel: "out"-branch, based on the $\eta \to 0$ limiting case. Bottom panel: two different deformations δ and δ' are considered in the analytical approach [149–151], while particles are free to move in the energy minimization (EM) and MC approaches. **Right column:** top panel: "in"-branch, based on the $\eta \to \infty$ limiting case. Bottom panel: only one possible deformation δ is considered in the analytical approach.

The system effectively forms a bilayer, but with very low density in the second layer (we denote the original layer by *layer 1* and the layer formed by the displaced charges by *layer 2*)

$$\frac{\rho_2}{\rho} \;=\; \frac{1}{N} \ll 1. \tag{3.18}$$

We initially performed a small number of EA runs for different values of η and observed only two different configuration archetypes: equivalents of the "out"- and "in"-branches. In order to both increase system size and accuracy, we thus limit our investigation to these two branches. If we assume a hexagonal lattice in layer 2, we can calculate values of N that are *compatible* with either the "out"- or the "in"-branch. For the former, these N-values are given by

$$N_{\text{out}}(i,j) \;=\; (i+j)^2 - ij \tag{3.19}$$
$$\;=\; 3, 4, 7, 9, 12, 13, ..., 100, ..., 2025, ... \tag{3.20}$$

where $i \geq j$ and $j \geq 0$ are integers. Note that for some values of N, more than one configuration fulfilling all characteristics of the respective branch can be constructed, i.e., the mechanism is to some extent degenerate. An example is $N = 49$, which can be represented either with ($i = 7$, $j = 0$) or with ($i = 5$, $j = 3$); the two lattices are not identical. The values of N compatible with the "in"-branch are given by

$$N_{\text{in}}(i,j) \;=\; (i+j)^2 - ij + 1 \tag{3.21}$$
$$\;=\; 4, 5, 8, 10, 13, 14, ..., 101, ..., 2026, ... \tag{3.22}$$

Note that some values of N_{out}- and N_{in}-values are identical, thus they can be used in either branch. This fact will be useful when we try to calculate the energy barrier between the two branches.

We compare results obtained from the following three approaches:

- The analytical approach considers the "out"- and "in"-branches as described in Figure 3.6. While it is able to correctly describe the nonperiodicity of the system, only a limited set of selected deformations can be taken into account (two in the "out"-branch, one in the "in"-branch).

- The energy minimization (EM) approach considers system sizes of $N = 100$ and $N = 101$ per unit cell (using periodic boundary conditions) for the "out"- and "in"-branches, respectively. We use the L-BFGS-B algorithm [104] to relax the undistorted configuration. All particles are free to move in this approach.

- The Monte Carlo (MC) approach considers system sizes of $N = 2025$ and $N = 2026$ per cell (again using periodic boundary conditions) for the "out"- and "in"-branches, respectively. Simulations are initialized with either the "out"- or "in"-configuration and – with exception to the tagged particle – all particles are allowed to move. We perform simulations at low

temperature (corresponding to a high coupling constant $\Gamma = \sqrt{\pi\sigma}Q^2/k_{\mathrm{B}}T \approx 1550$ such that the overall crystalline order is preserved [152, 153]. The system is first equilibrated for $\approx 2 \times 10^5$ MC cycles before computing averages for $\approx 3 \times 10^5$ MC cycles.

Apart from the documentation of the rearrangement of the hexagonal lattice caused by the vertical displacement of this single charge, the transition between the "out"- and the "in"-branches represents an additional interesting problem. We try to investigate the involved energy barrier using the nudged elastic band (NEB) method (see Section 2.5). For this method, we require "out"- and "in"-configurations with the same number of particles per cell. We find that such configurations can *always* be found for what we denote *double-compatible* values

$$
\begin{aligned}
N_{\mathrm{out}}(i+1, i-1) = & \ 3i^2 + 1 \ = N_{\mathrm{in}}(i,i) \\
N_{\mathrm{out-in}}(i) = & \ \ \ 3i^2 + 1,
\end{aligned}
\tag{3.23}
$$

where $i > 0$ is an integer. Note that there are values of N other than $N_{\mathrm{out-in}}$ that also fulfill the condition $N_{\mathrm{out}} = N_{\mathrm{in}}$: examples are $N_{\mathrm{out}}(4,3) = 37 = N_{\mathrm{in}}(6,0)$ or $N_{\mathrm{out}}(8,0) = 64 = N_{\mathrm{in}}(6,3)$.

We investigate configurations with $N_{\mathrm{out-in}} = 4, 13, 28, 49$ particles per cell. While these cells are comparatively small, they allow us to investigate a trend in the energy barrier as the system size increases and possibly even an extrapolation to the non-periodic system. As detailed in Section 2.5, we need to uniquely identify all particles in the cell in both start- and end-configuration since particles are required to be distinguishable in the NEB approach. Since this limits the possible transition paths, we have to be very careful in this choice. For double-compatible values of $N = N_{\mathrm{out-in}}$, "out"- and "in"-configurations with the same periodicity can be constructed.

If we now overlay both configurations (corresponding to the start- and end-points of the NEB approach), we can correlate particles in one branch with those in the other (see Figure 3.7). The required displacements form a vortex-like scheme: the cell spanned by the periodic images of the tagged charge consists of two equilateral triangles. At the center of one of these, particle positions for the two branches are almost identical; we denote this the center of the vortex, where we can start correlating particle positions based on proximity. As we move radially outwards from the center of this vortex, the displacements between the "out"- and "in"-branches increase in a swirl-like manner, allowing us to systematically correlate particle positions even if the displacements are larger than the lattice spacing a.

3.2.3. Theory and order parameters

In order to properly compare the results obtained with the three different approaches specified in the preceding subsection, we have defined the defect energy δE^*, which quantifies the energy penalty caused by the vertical displacement of the tagged charge. Since we know
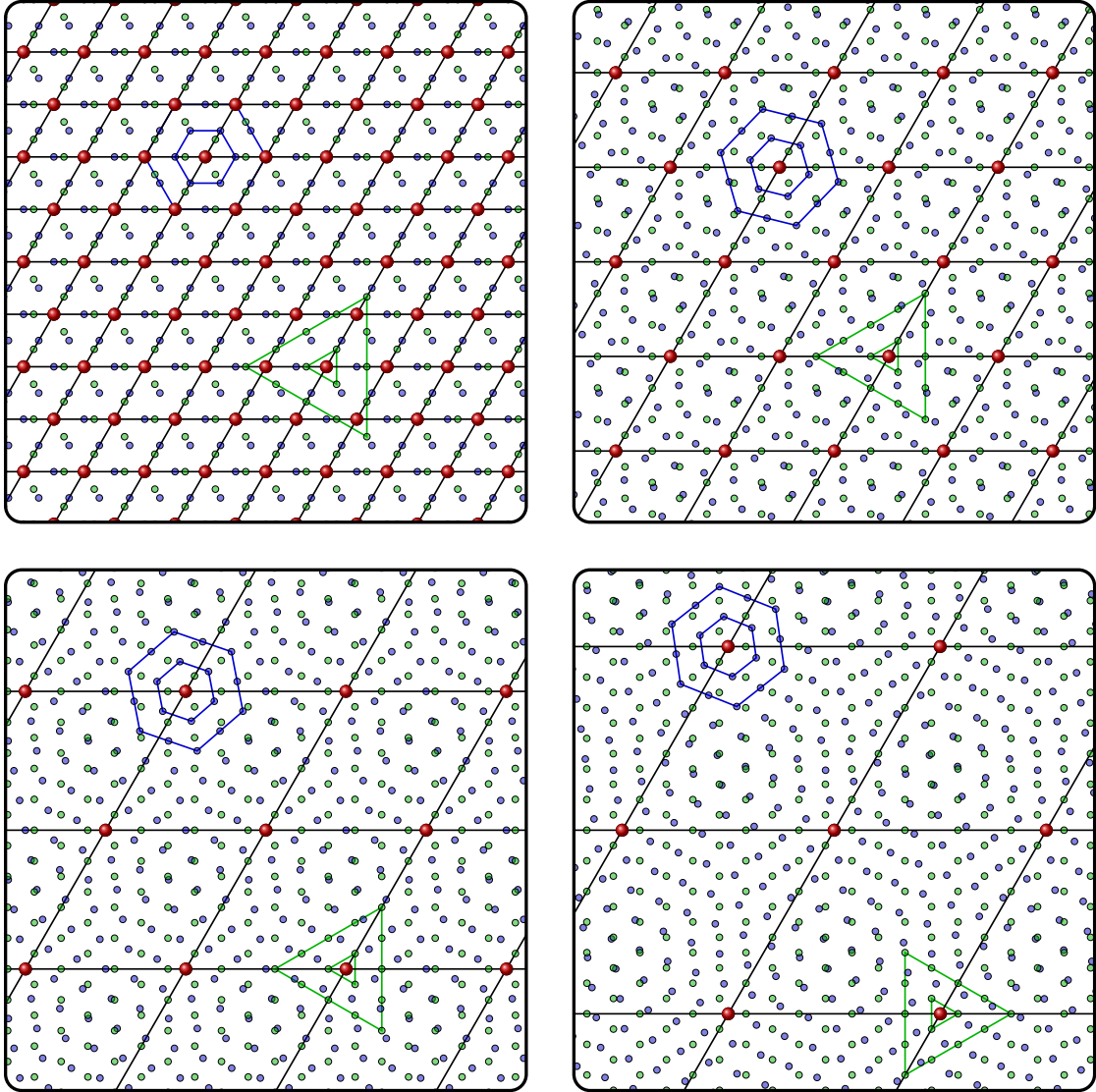
Figure 3.7.: Schematic views of superposed "out"- (blue circles) and "in"-branch (green circles) configurations for different double-compatible cell sizes $N_{\text{out}-\text{in}}$. **Top row:** left panel: $N_{\text{out}-\text{in}}(i = 1) = 4$. Right panel: $N_{\text{out}-\text{in}}(i = 2) = 13$. **Bottom row:** left panel: $N_{\text{out}-\text{in}}(i = 3) = 28$. Right panel: $N_{\text{out}-\text{in}}(i = 4) = 49$. The position of the tagged charge (red sphere) and the lattice vectors (black lines) are the same for both branches. Blue and green lines indicate the orientation of the hexagonal lattices in the two branches, as well as the position with respect to the tagged charge. For small values of N, correlation based on proximity arguments is straight-forward. For larger values of N, we consider the vortex-like structure of the displacement between the two branches: each cell is composed of two equilateral triangles formed by periodic images of the tagged charge. The center of one of these triangles is considered the center of the vortex, where displacements are very small. We can systematically identify correlations between the two branches by radially moving outwards from the vortex center; this allows us to correlate particles even when the displacement is larger than the lattice spacing a of the underlying hexagonal lattice.

the limiting cases concerning the particle arrangement for $\eta \to 0$ and $\eta \to \infty$ – namely the "out"- and "in"-branches, respectively – we can calculate the corresponding defect energies. In the former case, we obtain the simple hexagonal monolayer, i.e.,

$$\delta E^*(\eta \to 0) = 0. \tag{3.24}$$

In the latter case, we obtain a hexagonal monolayer (index 1) with an additional charge located in a layer (index 2) that is separated by an infinite distance from layer 1. If we assume that the neutralizing background is also split between the two layers such that both are *locally* electro-neutral, i.e.,

$$\frac{\sigma_2}{\sigma_1} = \frac{1}{N-1}, \tag{3.25}$$

we can easily calculate the asymptotic defect energy for the "in"-branch: since both layers are hexagonal at infinite separation $\eta \to \infty$ and do not interact with each other

$$\delta E^*(\eta \to \infty, N) = c_{\mathrm{m}} Q^2 \sqrt{\rho} N \left[\left(\frac{N-1}{N} \right)^{3/2} - 1 \right]. \tag{3.26}$$

Interestingly, in the limit of an infinite cell size (i.e., for $N \to \infty$), this expression yields an asymptotic defect energy

$$\lim_{N \to \infty} \delta E^*(\eta \to \infty, N) = c_{\mathrm{m}} Q^2 \sqrt{\rho} \lim_{N \to \infty} \left[N \left(1 - \frac{1}{N} \right)^{3/2} - N \right]$$

$$\delta E^*(\eta \to \infty, N \to \infty) = -\frac{3}{2} c_{\mathrm{m}} Q^2 \sqrt{\rho}. \tag{3.27}$$

The prefactor 3/2 might seem counter-intuitive at first sight, as we would expect a factor of one instead. However, the removal of a single particle from the infinite lattice causes an infinitesimal increase in the lattice constant a of the hexagonal lattice in layer 1

$$a \to a \sqrt{\frac{N}{N-1}} \tag{3.28}$$

$$\rho_1 \to \rho_1 \frac{N-1}{N}. \tag{3.29}$$

The resulting energy gain affects infinitely many particles, yielding thus a finite difference. We can also understand the prefactor 3/2 if we keep in mind that c_{m} is only the *average* energy per particle in the monolayer. However, when we start building a monolayer by assembling charges, the energy required for adding another charge depends on how many charges have already been accumulated: thus, the corresponding prefactor is different for each case and also differs from the average value c_{m}. Our result is substantiated by analytical calculations, which do not assume periodicity.

As already indicated in Figure 3.6, the deformations caused by the vertical displacement of the tagged charge are of particular interest to us. We thus use them to quantify the agreement between the different approaches. For the "out"-branch, we measure the normalized projected distance between the the tagged charge and its six nearest neighbors ($i = 1 - 6$, see bottom left panel of Figure 3.6)

$$\delta_i(\eta) = \frac{s_{0i}(\eta)}{s_{0i}(\eta \to 0)} - 1, \qquad (3.30)$$

where $s_{0i}(\eta \to 0) = a$ is the lattice constant of the hexagonal lattice. Note that this may lead to up to six different values in the EM approach, while only two possible different values

$$\delta = \delta_1 = \delta_3 = \delta_5 \qquad (3.31)$$
$$\delta' = \delta_2 = \delta_4 = \delta_6 \qquad (3.32)$$

are assumed in the analytical approach. In the MC approach, we measure the positions of the first three peaks of the radial distribution function, respectively. The third peak is required for a correct identification of the lattice structure using the radial distribution function.

For the "in"-branch, we measure the distances to the nearest and second-nearest neighbors (see bottom right panel of Figure 3.6), normalized by the corresponding undeformed distances at $\eta \to \infty$. In the analytical approach, only the deformations caused by the three nearest neighbors are considered; they are assumed radially symmetric

$$\delta = \delta_1 = \delta_2 = \delta_3 \qquad (3.33)$$
$$\delta' = 0. \qquad (3.34)$$

3.2.4. Results

The left panel of Figure 3.8 shows the obtained defect energies for the "out"- and "in"-branches in the analytical approach, the EM approach, and the MC approach. We can see that the "out"-branch is favorable for small η, whereas the "in"-branch is favorable for large η. The transition between the two branches occurs around $\eta_c \approx 0.47$. The energy curve for each branch continues into the region where it is no longer favorable, indicating that the two branches are separated by an energy barrier and thus can not transform continuously into each other. The slope of the energy difference between the two branches (see right panel of Figure 3.8) around η_c also indicates a first order transition.

If we now turn to compare the results obtained with the different approaches, we see that agreement is very good for small values of η, especially for the "out"-branch. As η increases, the differences become larger and though this is not easily visible to the naked eye, the value η_c at which the "in"-branch becomes favorable differs between the three approaches (see right panel of Figure 3.8). While EM and MC agree quite well, the analytical approach
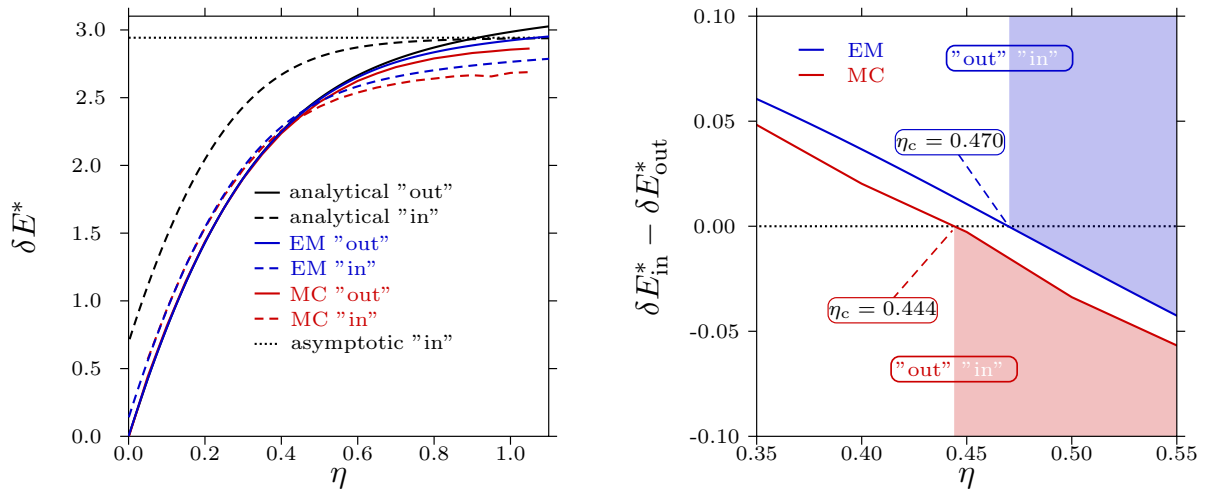
Figure 3.8.: Defect energies obtained with the three approaches: analytical calculations (black), energy minimization (blue), and MC simulations (red). Left panel: defect energies $\delta E^*(\eta)$ obtained for the "out"-branch (solid lines) and the "in"-branch (dashed lines). The asymptotic limit for the "in"-branch $E_{in}^*(\eta \to \infty)$ is indicated by a dotted black line. Right panel: energy difference between "out"- and "in"-branches, $\delta E_{in}^* - \delta E_{out}^*$, close to the transition. The η-range where the "in"-branch is favorable differs slightly between the EM and MC approaches (indicated by colored regions).

overestimates the stability of the "out"-branch significantly. This is most likely due to the fact that this approach only considers only three deformations in the "in"-branch and the configuration can thus not fully adapt to the presence of the tagged charge. It is therefore interesting to also compare the deformations themselves, which we will do below.

As pointed out above, even for large values of η, configurations in the "out"-branch do not transform into "in"-branch configurations (or vice versa for small η). This implies the existence of an energy barrier between the two branches preventing meta-stable configurations of one branch from decaying into the other stable branch, indicating a first order transition. In the EM approach, where we only locally optimize configurations, even a small barrier would be sufficient to prevent this decay. The same is, however, not true for the MC approach: while we perform simulations at relatively low temperature, one would still expect configurations to transform if the energy barrier is small enough. However, we have to keep in mind that the barrier height depends on the system size for a first order transition [126, 154, 155].

We now focus on the measured deformations in the two branches. The left panel of Figure 3.9 shows the deformations, which are characteristic of the three different approaches, of the tagged charge's nearest neighbors along the "out"-branch. For small values of η – including the entire range where the "out"-branch is stable – we observe that all deformations are isotropic, i.e., the ring of nearest neighbors contracts uniformly to compensate for the displaced tagged charge. We can see that only for $\eta \approx 0.60$ small differences between the ana-

lytical approach (which only considers these six deformations) and the other two approaches (where all particles are free to move) appear. We can explain this observation by the fact that displacements of particles in the second or third ring (which also contract slightly) become more pronounced. The analytical approach thus underestimates the deformation.
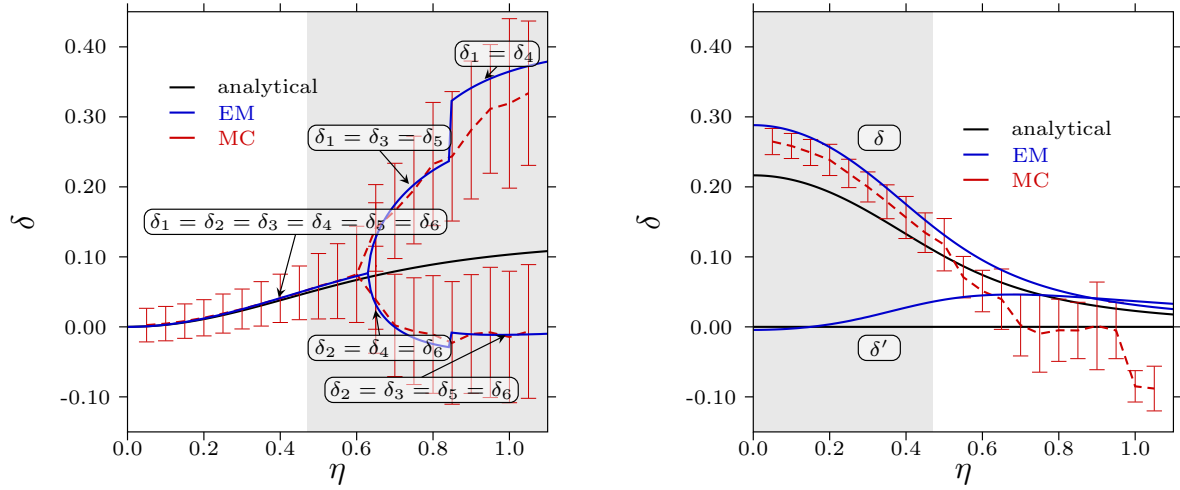

Figure 3.9.: Deformations of the lattice surrounding the tagged charge (displacement of the six nearest neighbors from their equilibrium positions at $\eta = 0$) obtained using the following three approaches: analytical calculations (black), EM (blue), and MC simulations (red). In the MC approach, a Gaussian fit is used to determine the peak positions in $g(r)$ and thus the deformations [151, 156]. Error bars indicate the width of the peaks. Left panel: "out"-branch, where we measure displacement of the six particles in the first ring. In the stable region $\eta \lesssim 0.47$, the ring of nearest neighbors contracts isotropically. In parts of the metastable region (area shaded gray), more complicated contractions occur (see text). These are not observed in the analytical approach. Right panel: "in"-branch, where we measure displacement of three particles in the first and second rings each (δ and δ', respectively).

Starting at $\eta \gtrsim 0.63$, we observe a different process: instead of a uniform contraction, we observe that three neighbors approach the tagged charge, while the other three move away (see top center panel of Figure 3.10). As quantified in the left panel of Figure 3.9, neighbors 1, 3, and 5 approach, while neighbors 2, 4, and 6 move away. This process is somewhat reminiscent of the transformation of a hexagon into a triangle (see top center panel of Figure 3.10). The previous six-fold symmetry is thus broken and replaced by a three-fold symmetry. Finally, for $\eta \gtrsim 0.85$, we observe a more complicated process, where two opposing neighbors approach and the other four move away (see left panel of Figure 3.9 and top right panel of Figure 3.10). Here, the produced defect region extends over a much larger area of the lattice.

The right panel of Figure 3.9 shows the deformations in the "in"-branch. For the results
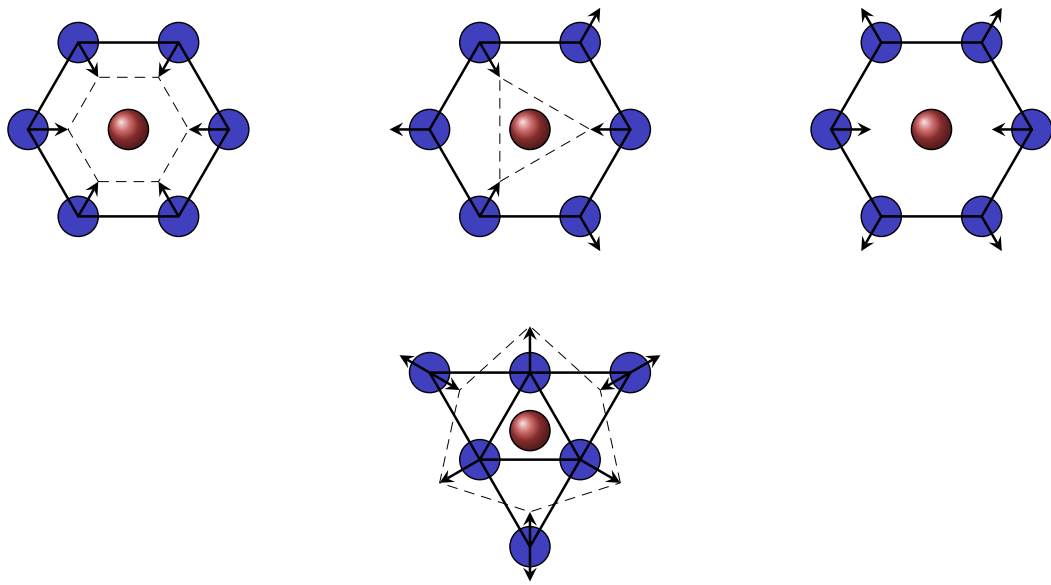
Figure 3.10.: Schematic view of the different deformation mechanisms encountered in the EM approach. **Top row:** "out"-branch. Left panel: uniform contraction of the ring of nearest neighbors encountered for small η. Note that this is the only stable deformation mechanism. Center panel: symmetry breaking for intermediate η, reminiscent of the transformation of a hexagon into a triangle. Right panel: more complicated deformation mechanism for large η, which is highly metastable. **Bottom panel:** deformation mechanism in the "in"-branch.

obtained with the EM approach, both δ (for the three nearest neighbors) and δ' (for the three second-nearest neighbors) are plotted. Note that the analytical approach assumes $\delta' = 0$. We observe that the agreement between the analytical and the EM approaches is reasonably good for large η, but noticeably not perfect, even for $\eta \approx 1.1$. In this region results are difficult to compare to the MC approach, where the position of the tagged charge is basically uncorrelated (the inter-layer energy becomes negligible). For small values of η, we observe that the analytical approach underestimates the deformation, while EM- and MC-data are in agreement.

Our final point of interest lies in determining the height of the energy barrier ΔE^* between the two branches, as well as in identification of the associated saddle point. The left panel of Figure 3.11 shows the energy barriers between the two branches calculated for several system sizes. The reaction coordinate r describes the transition from the start-configuration (in our case the "out"-branch; $r = 0$) to the end-configuration ("in"-branch; $r = 1$). η is chosen such that the energy difference between the "out"- and the "in"-branches for the respective system size is minimal after local relaxation $\delta E^*_{\text{out}} \approx \delta E^*_{\text{in}}$ (i.e., we are at η_c for the respective system size N). Table 3.2 lists the values of η that have been used for each N (see $N_{\text{out}-\text{in}}$ in Equation 3.23), as well as the calculated barrier height. We observe no barrier for the smallest system size $N = 4$, where start- and end-configurations are identical after relaxation. For the other three system sizes, we see that the barrier height grows with increasing N. This may explain why we do not observe a transition between the two branches in MC simulations at low temperatures: rearrangement of the entire crystal constitutes a barrier which grows with increasing N. If we disregard the case $N = 4$, the system sizes considered indicate that the energy barrier grows as $\Delta E^* \sim N$.

Table 3.2.: Dependence on system size N of the vertical displacement η for which we observe minimal energy difference between relaxed "out"- and "in"-branches. The energy barrier ΔE^* between the branches increases with increasing N.

N	η	ΔE^*
4	(0.45891)	0
13	0.45891	0.02862
28	0.46461	0.06561
49	0.46738	0.10701

The right panel of Figure 3.11 shows a snapshot of the configuration at the saddle point for $N = 49$. While most parts of the crystal remain hexagonal, defect lanes connecting the periodic images of the tagged charge form. These lanes form the boundaries of the hexagonal regions. We can understand the transition process as a rotation of these hexagonal regions (denoted vortices) and an associated sliding of the lanes with respect to each other. At the saddle point, the lanes are almost rectangular. Since most of the cell is hexagonal, a first approximation of the energy barrier (neglecting non-nearest-neighbor interactions) depends only on the length of the defect lines separating the vortices. The length of these lines is proportional to $l \sim \sqrt{N}$ for large values of N and vanishes for $N = 4$. This proportionality
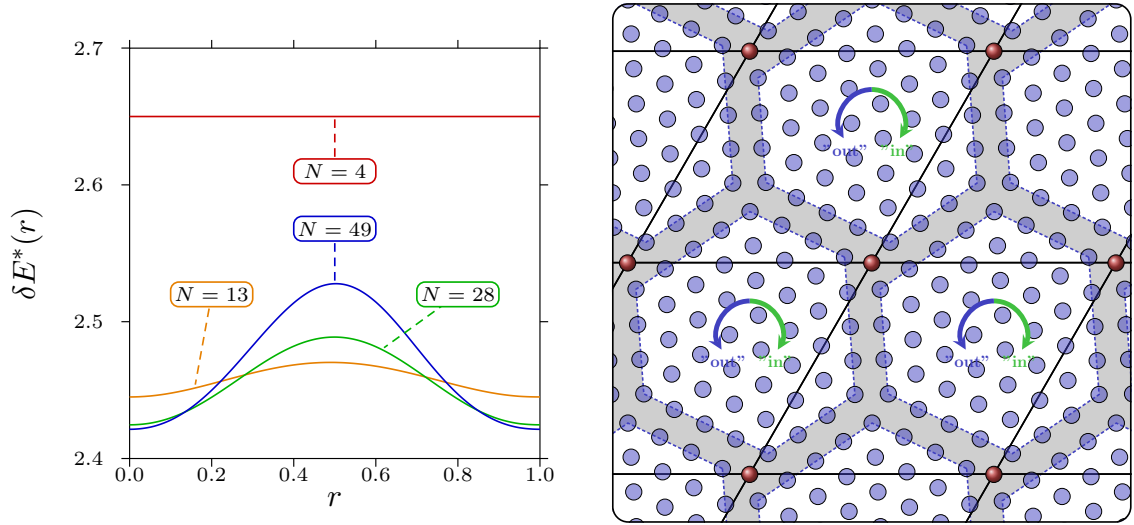
Figure 3.11.: Left panel: energy barriers calculated for the four considered system sizes $N = 4, 13, 28, 49$. The reaction coordinate r describes the transition from start-configuration ("out"; $r = 0$) to end-configuration ("in"; $r = 1$). There is no barrier for $N = 4$, since start- and end-configuration (after local relaxation) are identical in this case. For the other values of N, we observe an increase in barrier height as N increases. Right panel: snapshot of the saddle point configuration for $N = 49$. Hexagonal crystallites are indicated by dashed blue lines; arrows indicate how the rotation of these crystallites leads towards "out"-and "in"-branch configurations, respectively. At the saddle point, lanes (shaded gray) connecting the periodic images of the tagged charge appear.

is in contrast to the data in Table 3.2 and indicates that the study of much larger systems would be required. In addition, more complicated transition mechanisms than the simple vortex rotation considered here may be at work.

3.2.5. Conclusions and outlook

In summary, we have seen that the vertical displacement of a single charge from a hexagonal planar Wigner crystal causes not only small deformations close to the defect, but requires a complete reorganization of the crystal for large separation distances. The energy barrier associated with this rearrangement increases with the system size, trapping the system in meta-stable branches at low temperature. We have treated the problem using the following three approaches: analytical calculations, energy minimization, and MC simulations. In η-ranges where all approaches were able to treat the problem adequately, we have found good agreement between the corresponding data sets. In other η-ranges, we were able to understand differences in the results obtained with the different approaches.

Most of the results presented in this section were published in [151].

For future work, a more accurate computation of the energy barrier between the two branches is of interest. This would require investigating more and larger system sizes. The inherent problem here is our need to correlate start- and end-configuration in the NEB method, leading to – at least loosely – pre-defined structures along the transition path.

3.3. Asymmetric Wigner bilayer crystals

3.3.1. Introduction

As we have seen in Section 3.1, long-ranged systems composed of classical point charges can show a rich variety of stable structures. For these cases, we have been able to verify the accuracy and flexibility of both our implementations of Ewald summation and EA global energy minimization. In Section 3.2, we have studied the effects of a vertical displacement of a single charge from the monolayer Wigner crystal. For this problem, we have already employed concepts of a true bilayer system, albeit in the dilute case. In this section, we focus on actual bilayer systems and investigate the interplay between two layers of point charges. The ground state structures of *symmetric* bilayer Wigner crystals (the term symmetric referring to the fact that both layers exhibit the same background, $\sigma_1 = \sigma_2$, and thus also density and particle arrangement) have only recently been determined analytically [149, 150]: depending on the distance between the plates, five different archetypes of structures (denoted structures I through V) can be observed. In particular the stability of the hexagonal monolayer (structure I) has posed a long-standing question [157, 158]. The exact, analytical results showed that structure I is only stable if the distance between the plates is zero. The sequence of phases

and their stability regions provide a final benchmark for our implementation and we find excellent agreement.

Bilayer Wigner crystals can be observed in several experimental systems, such as ions in Penning traps [159], electrons [160] or holes [161–163] in double quantum well semiconductor interfaces, confined dusty plasmas [164], bilayer graphene [165], or vertically coupled quantum dots [166]. The symmetric bilayer Wigner crystals poses a simple, yet already surprisingly interesting problem [158, 167, 168]. In this section, we develop the model of the *asymmetric* bilayer Wigner crystal, where the particle arrangements of the two layers may differ ($\sigma_1 \neq \sigma_2$), leading thereby to a tremendous increase in the complexity of the problem.

3.3.2. Model and approach

The bilayer Wigner system consists of two parallel infinite plates with uniform charge densities σ_1 and σ_2, respectively. The plates are separated by a vertical distance h and we use the same dimension-less plate separation $\eta = h\sqrt{\sigma/2}$ as in Section 3.2, where $\sigma = \sigma_1 + \sigma_2$ is the total neutralizing background charge density. The point charges of size Q occupy the plates with number densities $\rho_1 = N_1/S_0$ and $\rho_2 = N_2/S_0$ (S_0 being the unit cell area), respectively. We introduce the total background charge and particle number densities

$$\sigma \;=\; \sigma_1 + \sigma_2 \tag{3.35}$$

$$\frac{N}{S_0} = \rho \;=\; \rho_1 + \rho_2, \tag{3.36}$$

which allow us to define global electro-neutrality

$$\sigma S_0 + \rho Q S_0 \;=\; 0 \tag{3.37}$$

$$\sigma S_0 \;=\; -\rho Q S_0 = -NQ. \tag{3.38}$$

In particular cases, the system also exhibits *local* electro-neutrality, where both layers carry zero net charge

$$\sigma_1 S_0 \;=\; -\rho_1 Q S_0 = -N_1 Q \tag{3.39}$$

$$\sigma_2 S_0 \;=\; -\rho_2 Q S_0 = -N_2 Q. \tag{3.40}$$

In the *symmetric* bilayer Wigner system (see left panel of Figure 3.12), both plates carry the same charge density $\sigma_1 = \sigma_2 = \sigma/2$. This also implies that they carry the same number of charges $\rho_1 = \rho_2 = \rho/2$, which entails local electro-neutrality.

In experimental systems, applying an electric field perpendicular to the plates will cause more point charges to sit on one plate than the other. We can model this behavior by
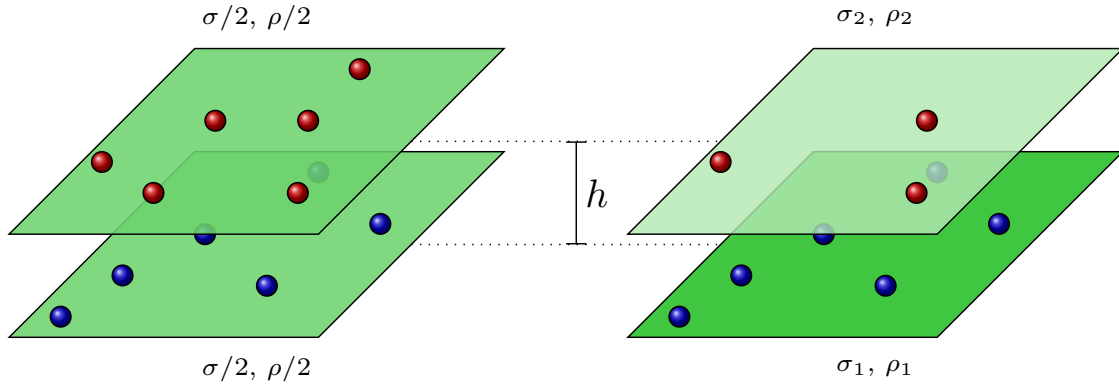
Figure 3.12.: Schematic views of the bilayer Wigner crystal model. Left panel: symmetric case, where both plates have the same charge density $\sigma_1 = \sigma_2$. Both plates carry the same density of point charges $\rho_1 = \rho_2$. Right panel: asymmetric case, where the charge densities are different $\sigma_1 > \sigma_2$. In general, the plates carry different densities of point charges $\rho_1 \geq \rho_2$.

introducing the asymmetry parameter A such that (see right panel of Figure 3.12)

$$A \;=\; \frac{\sigma_2}{\sigma_1} \tag{3.41}$$

$$\sigma_1 \;=\; \frac{1}{1+A}\sigma \tag{3.42}$$

$$\sigma_2 \;=\; \frac{A}{1+A}\sigma. \tag{3.43}$$

The range of A is technically $A \in (-\infty, \infty)$; however, a negative value leads to the trivial hexagonal Wigner monolayer (structure I). In addition, A-values larger than unity are equivalent to the range $A \in (0, 1)$, with the role of the two plates reversed. We can thus limit our investigations to the range $0 < A \leq 1$, with $A = 1$ corresponding to the symmetric case.

A direct consequence of $A < 1$ is that we can no longer assume $\rho_1 = \rho_2 = \rho/2$. Instead, we only obtain

$$\rho_1 \;\geq\; \rho_2 \tag{3.44}$$

$$\rho_1 + \rho_2 \;=\; \rho. \tag{3.45}$$

We define an order parameter x as follows:

$$x \;=\; \frac{N_2}{N} = \frac{\rho_2}{\rho} \tag{3.46}$$

$$\rho_1 \;=\; (1-x)\,\rho \tag{3.47}$$

$$\rho_2 \;=\; x\rho. \tag{3.48}$$

Global electro-neutrality is still maintained, while local electro-neutrality is no longer guar-

anteed.

The energy per particle of the system can be calculated using the same Ewald summation as in Section 3.2 (see also Appendix A.1). We will use the reduced energy per particle, defined as

$$\frac{E^*}{N} \;\; = \;\; \frac{E}{N\sqrt{\rho}Q^2}. \tag{3.49}$$

In an effort to determine the ground state structure of the system for the entire range $0 \le \eta \le \infty$ and $0 < A \le 1$, a straight-forward approach would be to perform EA optimizations for a suitably fine grid in both parameters η and A. However, we can take advantage of the fact that the only A-dependent terms E_A^* in the energy calculation are independent of the particle positions and instead only depend on η and x:

$$E_A^*(\eta, x, A) \;\; = \;\; 2^{3/2}\pi\eta N \frac{x + A^2 - xA^2}{\left(1 + A\right)^2}. \tag{3.50}$$

This allows us to transform the energy obtained for $(\eta, x, A_{\mathrm{old}})$ to a new value $(\eta, x, A_{\mathrm{new}})$ by using

$$E^*(\eta, x, A_{\mathrm{new}}) \;\; = \;\; E^*(\eta, x, A_{\mathrm{old}}) - E_A^*(\eta, x, A_{\mathrm{old}}) + E_A^*(\eta, x, A_{\mathrm{new}}). \tag{3.51}$$

We can thus formulate the following strategy for computing the phase diagram, which in our experience improves the convergence speed when sampling search space:

(i) We do not allow particles to move from one layer to the other but consider all possible values of $x(\le 0.5)$ that are compatible with the number of particles per cell, which ranges from $N = 1$ to $N = 40$.

(ii) We fix $A = 0$ and perform computations for 201 evenly spaced values of $\eta \in [0, \sqrt{2}]$. We thus obtain the optimized energy-values $E^*(\eta, x, A = 0)$.

(iii) We then proceed to $A > 0$ and vary this quantity on a grid of 201 evenly spaced values of $A \in [0, 1]$. The optimized energy for these configurations $E^*(\eta, x, A)$ is then obtained via

$$E^*(\eta, x, A) \;\; = \;\; E^*(\eta, x, A = 0) + 2^{3/2}\pi\eta N \frac{A}{(1 + A)^2}(A^2 - 2x - 2xA); \tag{3.52}$$

For a given state point $(\eta,\ A)$ we retain only the configuration with the lowest reduced energy per particle E^*/N as the ground state.

As we will see in Subsection 3.3.4, two competing effects – commensurability considerations favoring a discrete set of x-values and the effective charges of the two layers favoring continuous x-values as η and A change – govern what particle arrangement is formed. In order to obtain further insight into the interplay between these two effects, we compare our results to analytical calculations performed by Ladislav Šamaj and Emmanuel Trizac [149, 150].

These calculations feature extremely high accuracy and can be performed on a very fine grid in η and A. However, they require well-defined candidate structures (limiting their scope), which we try to identify using our EA tool.

We also perform Monte Carlo simulations at a low temperature for several points in the (η, A)-plane. For the simulations presented in this section, we use a system size of $N = 4056$ particles. The system is initialized with a configuration obtained from the EA approach (see Subsection 3.3.5). We first let it equilibrate for $\approx 1.6 \times 10^6$ MC cycles, before computing averages for $\approx 8.0 \times 10^5$ MC cycles. Each cycle consists of N attempted particle moves and one attempt to deform the unit cell. Particle moves are either two-dimensional (within the current layer) or vertical from one layer to the other.

In most cases, a vertical displacement of a particle is very unfavorable if it is not accompagnied by a simultaneous two-dimensional rearrangement of both layers; this can lead to problems with proper equilibration of the x-value. We thus use the configurations obtained with the EA tool as starting points for the MC simulations and explore their stability. We focus on the phases characterized by $x = 1/3$, which offer a rich variety of structures. Initializing the simulation with a configuration characterized by a value of x similar to the one obtained at zero temperature (but possibly a different two-dimensional particle arrangement) is very convenient: it supports the formation of this structure and prevents the system from getting stuck due to frustration effects between the two-dimensional particle arrangement and the value of x.

Since we are only interested in the low temperature behavior of the system, we use a large value of the coupling constant Γ, defined as

$$\Gamma = \frac{\sqrt{\pi}}{k_{\mathrm{B}}T}\sqrt{\rho}Q^2 \approx 2000. \tag{3.53}$$

As the two-dimensional Wigner crystal melts at $\Gamma \approx 140$ [169–171], we expect the formation of crystalline structures for this value of Γ.

Finally, we make extensive use of the results obtained in Section 3.2: as we will see in Subsection 3.3.4, the "out"- and "in"-branches studied in in Section 3.2 represent a special case of the asymmetric bilayer system and structures based on these two branches play an important role in the phase diagram. For a closer study of the competition between the hexagonal Wigner monolayer and structures based on the two branches, we again use energy minimization (EM). This allows us to use a finer grid in η and to increase the number of particles per cell. As in Section 3.2, we only study particle numbers compatible with the respective branch, ranging from $N = 3$ to $N = 101$.

3.3.3. Theory and order parameters

Several limiting cases with regards to η and A are known to us from previous work [149, 150] and from general considerations. We can use these as reference data for our other investigations.

$\boldsymbol{A \to 1}$: In the symmetric case, we obtain the symmetric structures [4] I, II, III, IV, and V [149, 150]. The boundaries are reproduced within the accuracy of our grid in η.

$\boldsymbol{A \to 0}$: When $\sigma_2 = 0$, all charges occupy plate 1, thus $x = 0$, and we obtain the hexagonal Wigner monolayer (structure I).

$\boldsymbol{\eta \to 0}$: In the case of a monolayer system, we also obtain structure I.

$\boldsymbol{\eta \to \infty}$: For infinitely large plate separation, the energy of the system can only have a finite value if both layers are locally electro-neutral. In this case, we can neglect the interaction between the layers and both of them are characterized by a hexagonal particle arrangement and an asymptotic density ratio

$$x_{\mathrm{asy}} \;\; = \;\; \frac{A}{1+A}. \tag{3.54}$$

In this case, the asymptotic energy per particle is given by

$$\frac{E^*_{\mathrm{asy}}}{N} \;\; = \;\; c_{\mathrm{m}} \frac{1 + A^{3/2}}{(1+A)^{3/2}}. \tag{3.55}$$

$\boldsymbol{x \to 0}$: As we know from our results obtained in Section 3.2, the transition from structure I to a bilayer system depends on the plate separation η. For $\eta \lesssim 0.47$, we have obtain the "out"-branch, while for $\eta \gtrsim 0.47$, we expect the "in"-branch. In the asymmetric bilayer system, the two branches correspond to the upper boundary η_{c}, beyond which the hexagonal monolayer is unstable and particles start moving to layer 2. As we will see, the value of η_{c} depends on A; if $\eta_c \lesssim 0.47$, we expect a transition from structure I to the "out"-branch, and a transition to the "in"-branch for $\eta_c \gtrsim 0.47$.

As mentioned before, competition between different phases is governed by the complex interplay between commensurability considerations (favoring a discrete set of x-values) and the effective charge of the two layers (favoring continuous x-values as η and A change). One can easily observe this feature as one considers the parameter x: for small values of η, the lattices of the two layers interact strongly and commensurability considerations are the dominant factor. Therefore, unit cells are typically rather small and have an intricate particle arrangement, such that simple fractions as values of x dominate (these preferred values can be seen as plateaus of constant x). For large values of η, on the other hand, what structure is formed is dominated by the precise value of x, while the interaction (and commensurability) between the particle arrangements in the two layers plays only a minor role; thus x becomes a rather continuous quantity, evidenced by continuous curves $x(\eta)$.

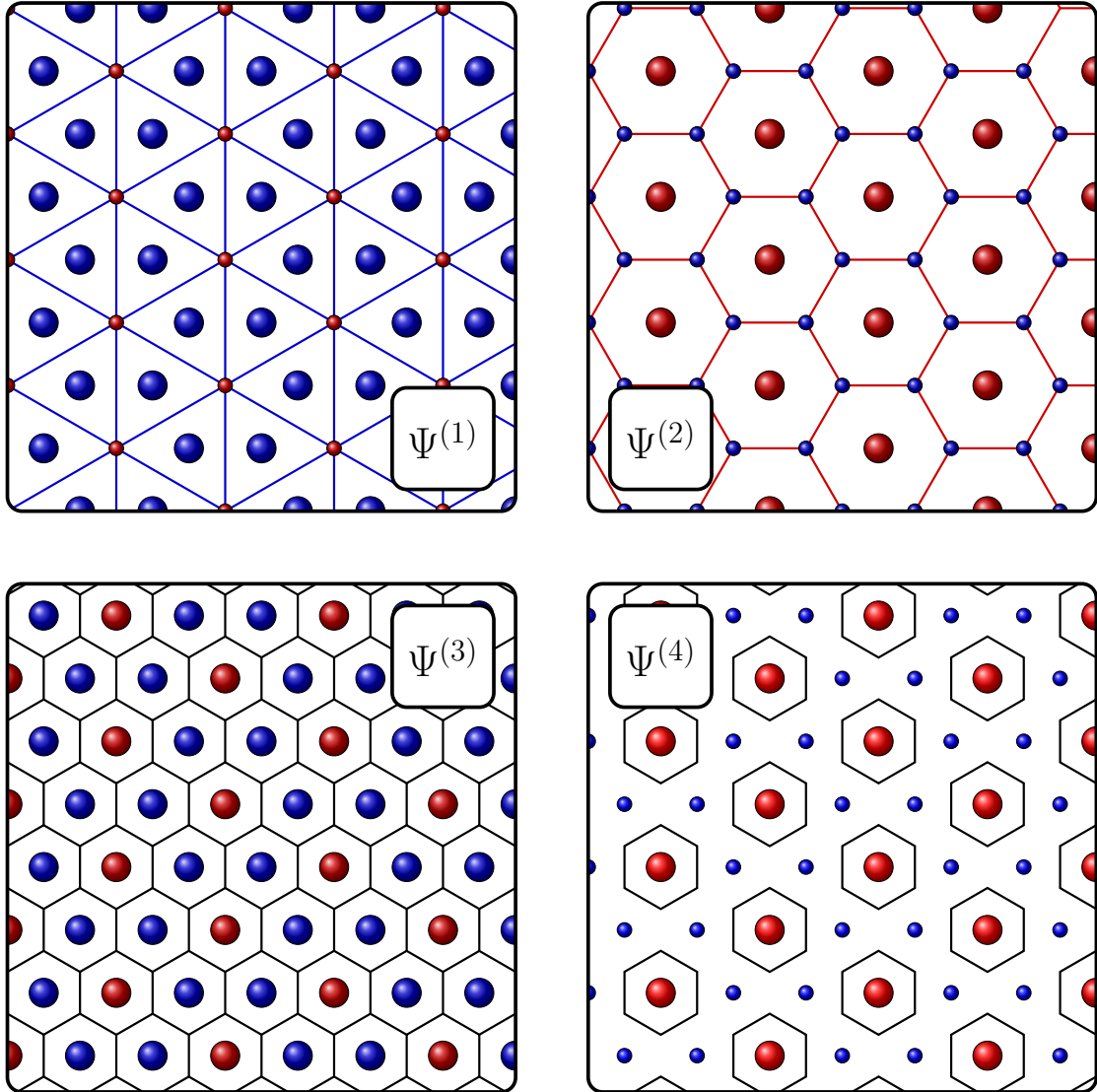4. The symmetric structures will be described in detail in the following subsection.

Figure 3.13.: Schematic view of the different Voronoi constructions used in the bilayer geometry. Voronoi polygons are indicated by lines. Particles in layer 1 are colored blue, particles in layer 2 red. Particles for which the respective order parameters are calculated are drawn enlarged. **Top row:** left panel: $\Psi^{(1)}$, calculated for particles in layer 1 only. Right panel: $\Psi^{(2)}$, calculated for particles in layer 2 only. **Bottom row:** left panel: $\Psi^{(3)}$, calculated for all particles projected into the xy-plane (see text). Right panel: $\Psi^{(4)}$, after projecting all particles into the xy-plane, we calculate parameters only for particles in layer 2 and consider only particles in layer 1 as possible neighbors (see text).

The full phase diagram computed using our EA tool is based on approximately $200 \times 200 = 40000$ grid points; to put order into the abundance of structures, we require a straight-forward method of quantifying the observed structures. For this purpose, bond-orientational order parameters (BOOPs) appear as an ideal tool (see Section 2.4). Due to the bilayer geometry of the present system, we can calculate these order parameters in several different ways:

- We can calculate them for particles in layer 1 only (denoted in the following $\Psi^{(1)}$, see top left panel of Figure 3.13).
- We can calculate them for particles in layer 2 only (denoted in the following $\Psi^{(2)}$, see top right panel of Figure 3.13).
- We can calculate them after projecting the positions of all particles into the xy-plane (denoted $\Psi^{(3)}$, see bottom left panel of Figure 3.13).
- We can calculate them after projecting the positions of all particles into the xy-plane, but calculate them only for particles in layer 2 and consider only particles in layer 1 as possible neighbors in the Voronoi construction (denoted $\Psi^{(4)}$, see bottom right panel of Figure 3.13); this can help us quantify the geometry of "holes" in layer 1, which are occupied by particles in layer 2. Note that such a construction is not space-filling, thus not a "real" Voronoi construction.

In two-dimensional structures, four- and six-fold rotational symmetries are common. We thus calculate Ψ_4 and Ψ_6. In addition, we are interested in rather unconventional crystalline structures, in particular those that might be indicative of quasi-crystals, which can exhibit uncommon rotational symmetries, such as five- or seven-fold ones. In addition to Ψ_4 and Ψ_6, we only discuss Ψ_5 in the results.

3.3.4. Results at vanishing temperature

We now proceed to present and discuss the obtained results. In a first step, we verify available results for energies and structures observed in the *symmetric* Wigner bilayer system [149, 150]. Since the *asymmetric* system is by far more complex and provides us with a multitude of results, we split the discussion in two parts:

(i) We first list and describe all observed structures, discussing the underlying competing effects, and how these structures can be adapted for the analytical approach. In parallel, we gradually construct the phase diagram.

(ii) Then, we discuss the relations between the different observed structures and further interesting phenomena. In addition, we compare our zero temperature results to MC simulations at low temperatures.

Symmetric case $A = 1$: structures I through V

As mentioned before, we will first verify results obtained for the symmetric case [149, 150]. The highly accurate analytical data available serve here as a final benchmark for our implementation. For $A = 1$, five different structures can be observed. The top panel of Figure 3.14 shows the sequence of structures in the symmetric case and their regions of stability.

In agreement with the analytical prediction, we find that the hexagonal monolayer (structure I, see first bottom panel of Figure 3.14) is only stable for $\eta = 0$. Previously, this fact had been a long-standing point of contention, as in many contributions a finite range of stability for the monolayer was predicted [157, 158, 167, 172]. We can easily identify the structure using the order parameter described in Subsection 3.3.3: $x = 0$.
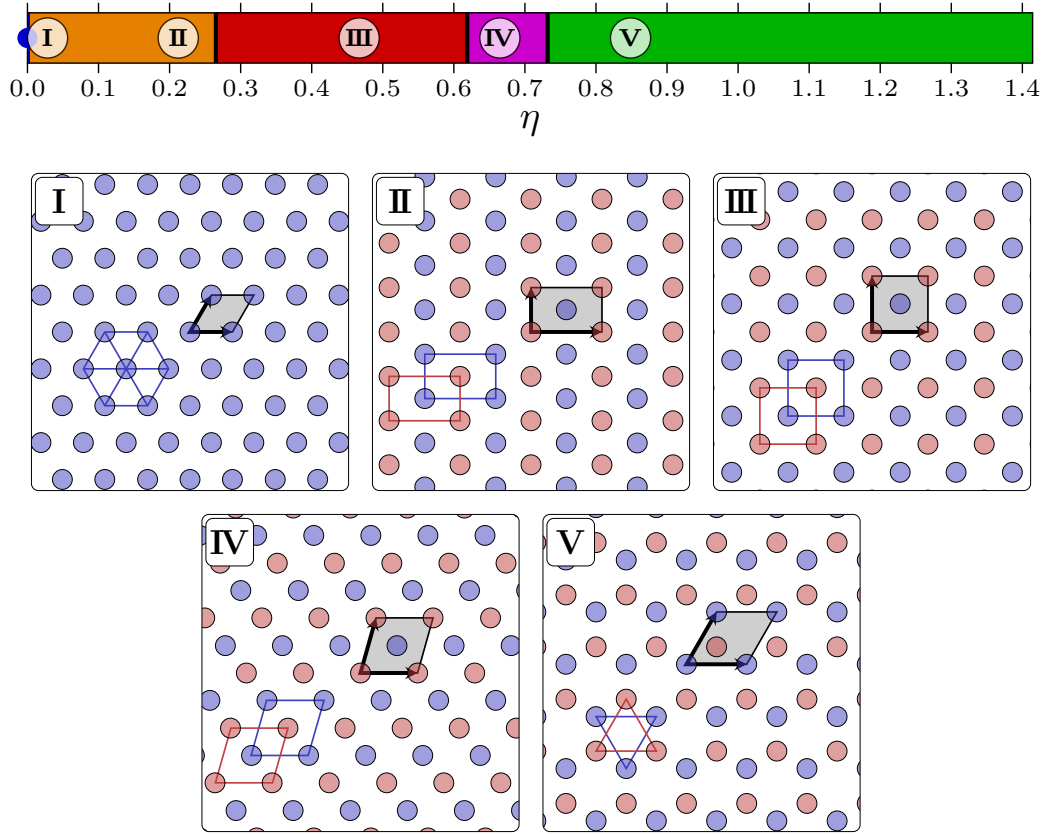
Figure 3.14.: Symmetric bilayer Wigner system ($A = 1$). Top panel: sequence of structures and their regions of stability in terms of η (as labeled). Structure I is only stable for $\eta = 0$ (indicated by a blue dot). Bottom panels: snapshots of structures I, II, III, IV, and V (as labeled). Particles in layer 1 are colored blue, particles in layer 2 red. The unit cell of the respective structure is indicated by the shaded area. Blue and red lines indicate interesting structural features in layer 1 and 2, respectively.

For $0 < \eta \lesssim 0.263$, we observe structure Ⅱ (see corresponding panel of Figure 3.14), which consists of a staggered rectangular bilayer. Particles in layer 2 are positioned above the centers of rectangles in layer 1 and vice versa. The side length ratio of the rectangles decreases from $\sqrt{3}$ at $\eta = 0$ to 1 (square) at $\eta = 0.263$. We can define structure Ⅱ using the order parameters: $x = 1/2$, $\Psi_4^{(1,2)} = 1$, $0 < \Psi_6^{(1,2)} < 1$.

For $0.263 \lesssim \eta \lesssim 0.621$, we observe structure Ⅲ (see corresponding panel of Figure 3.14), which consists of a staggered square bilayer. Particles in layer 2 are positioned above the centers of squares in layer 1 and vice versa. Structure Ⅲ can be considered a special case of both structures Ⅱ and Ⅳ; thus transitions between these three structures are of second order. We can define structure Ⅲ using the order parameters: $x = 1/2$, $\Psi_4^{(1,2)} = 1$, $\Psi_6^{(1,2)} = 0$.

For $0.621 \lesssim \eta \lesssim 0.732$, we observe structure Ⅳ (see corresponding panel of Figure 3.14), which consists of a staggered rhombic bilayer. Particles in layer 2 are positioned above the centers of rhombs in layer 1 and vice versa. The deformation angle of the rhombs decreases from $\pi/2$ (square) at $\eta = 0.621$ to 0.386π at $\eta = 0.732$; note that structure Ⅳ is not hexagonal for the latter value of η. We can define structure Ⅳ using the order parameters: $x = 1/2$, $0 < \Psi_4^{(1,2)} < 1$, $0 < \Psi_6^{(1,2)} < 1$.

Finally, for $0.732 \lesssim \eta$, we observe structure V (see corresponding panel of Figure 3.14), which consists of a staggered hexagonal (equilateral triangular) bilayer. Particles in layer 2 are positioned above the centers of triangles in layer 1 and vice versa. The transition between structures Ⅳ and V is of first order since there is a jump in the deformation angle and particles in each layer move from the center of a rhomb to the center of a triangle. Since both layers are hexagonal, structure V represents the asymptotic case for $\eta \to \infty$. We can define structure V using the order parameters: $x = 1/2$, $\Psi_4^{(1,2)} = 0$, $\Psi_6^{(1,2)} = 1$.

Hexagonal monolayer for $A < 1$: structure I

While structure I is not stable for finite η in the symmetric case, analytical calculations for $A < 1$ [173] have shown that this phase should be the energetically most favorable one at least for small values of η. The top panel of Figure 3.15 shows the region of stability of structure I, calculated with the EA and with the analytical approach. The known limiting cases for $\eta \to 0$ and for $A \to 0$ are correctly reproduced. In particular for small values of A, structure I appears to dominate the phase diagram. The small discrepancy in the line that limits the region of stability of structure I between the analytical and the EA approach will be discussed later.

The energy of structure I can be calculated analytically via the Madelung constant plus an η- and A-dependent energy term (see Equation 3.50)

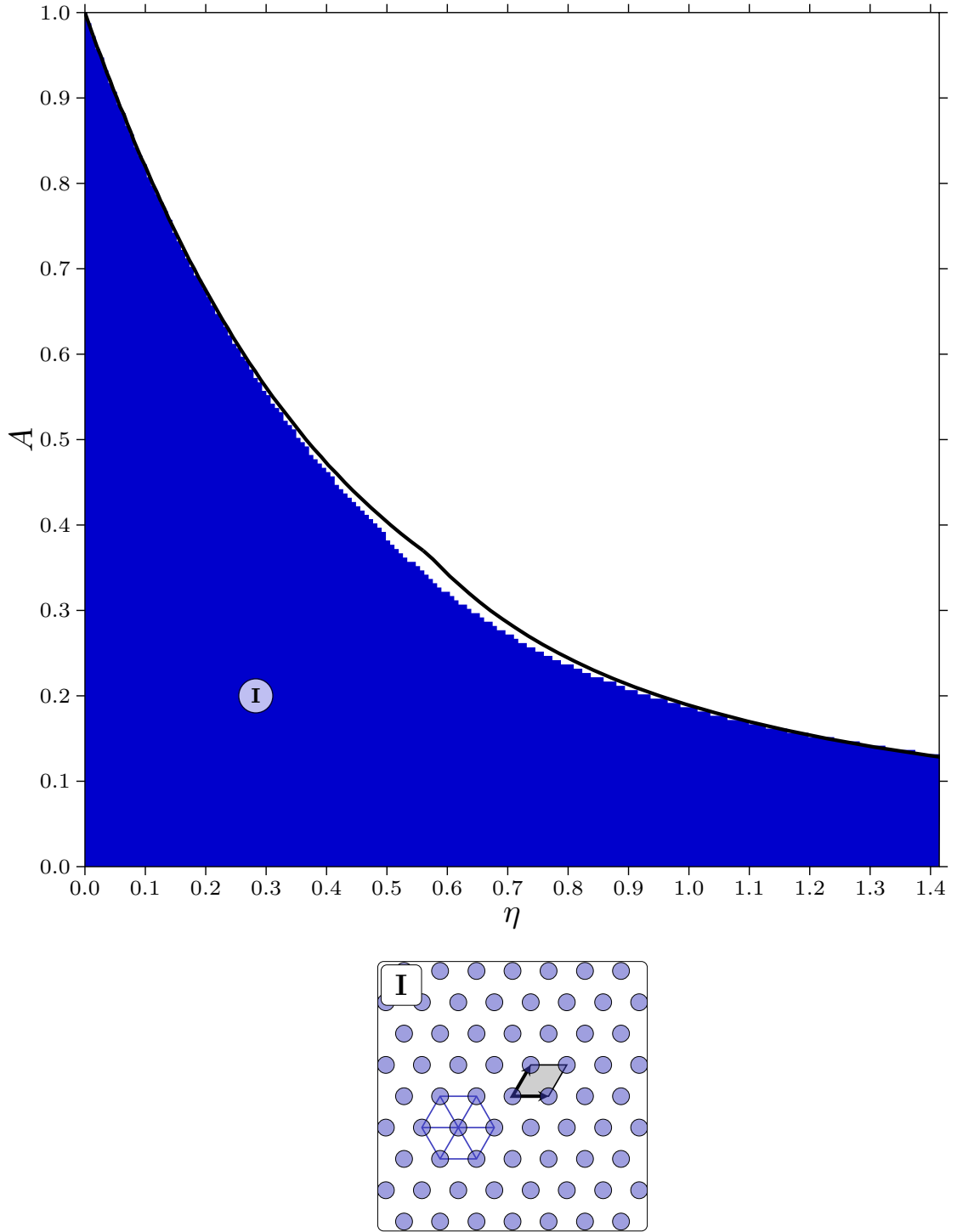$$\frac{E_{\mathrm{hex}}^*(\eta, A)}{N} = c_{\mathrm{m}} + 2^{3/2} \pi \eta \frac{A^2}{(1+A)^2}. \tag{3.56}$$

Figure 3.15.: Top panel: region of stability (colored blue) of the hexagonal monolayer (structure I); it fulfills the known limiting cases for $A \to 1$, $\eta \to 0$, and $A \to 0$. Bottom panel: snapshot of structure I. All particles are in layer 1. The unit cell is indicated by the shaded area. Blue lines indicate interesting structural features.

Structures based on the "out"-branch: structures I_x, H, and II_x

As we have seen in Section 3.2, the formation of a bilayer is facilitated – for small distances η – by the following mechanism: starting from the hexagonal crystal in layer 1 (structure I), a few particles are vertically displaced to layer 2; they leave hexagonal holes in layer 1 and form a new, ordered particle arrangement in layer 2. The emerging phases, structures I_x, H, and II_x, are shown in the snapshots of Figure 3.16; the regions of stability of the respective phases are shown in the top panel of this figure. The two-dimensional particle arrangement of these three structures is strongly reminiscent of the hexagonal monolayer, i.e., projecting all particles into one plane yields an almost perfect hexagonal lattice. We can thus characterize these structures using the criterion $\Psi_6^{(3)} > 0.9$. The main difference between structures I_x, H, and II_x lies in the percentage of particles in the upper layer, which in turn determines the structural mechanism:

- Structure I_x (see first bottom panel of Figure 3.16) represents the formation of the monolayer and is in direct competition with structure I. It is characterized by $0 < x < 1/3$.
- Structure H (see second bottom panel of Figure 3.16) is a special case of both structures I_x and II_x. It consists of a honeycomb lattice in layer 1 and a hexagonal lattice in layer 2 and is characterized by $x = 1/3$.
- Structure II_x (see third bottom panel of Figure 3.16) represents the transition from structure H to structures II and III. It is characterized by $1/3 < x < 1/2$. The hexagonal holes in layer 1 can be elongated or have more complicated shapes, while the lattice in layer 2 consists of distorted rectangles and triangles.

In the analytical approach, the two-dimensional particle arrangement of all three above phases is assumed to be perfectly hexagonal. The ordered particle arrangement of layer 2 is assumed to be as follows:

- For structure I_x, the structure of layer 2 is assumed to be hexagonal. This imposes a discrete set of possible values of x (see the quantity N_{out} derived in Section 3.2, Equation 3.19). Note that this criterion is less strict in the EA approach, where layer 2 is not necessarily perfectly hexagonal.
- Due to the high degree of symmetry in structure H, no deformations are possible in either of the lattices and the analytical model perfectly matches the particle arrangement observed with the EA.
- For structure II_x, layer 2 is assumed to be built up by a sequence of triangular and rectangular rows. These rows are produced by lines of particles in layer 1 or in layer 2 (indicated by dashed lines in the bottom right panel of Figure 3.16). A blue line followed by a red line produces a row of rectangles, while two blue lines followed by a red line produce a row of equilateral triangles. Using these two building blocks, x can be continuously interpolated between 1/3 and 1/2. Note that this does not always match the structure observed with EA. This mechanism shares some characteristics with precursors of quasicrystalline structures [174].
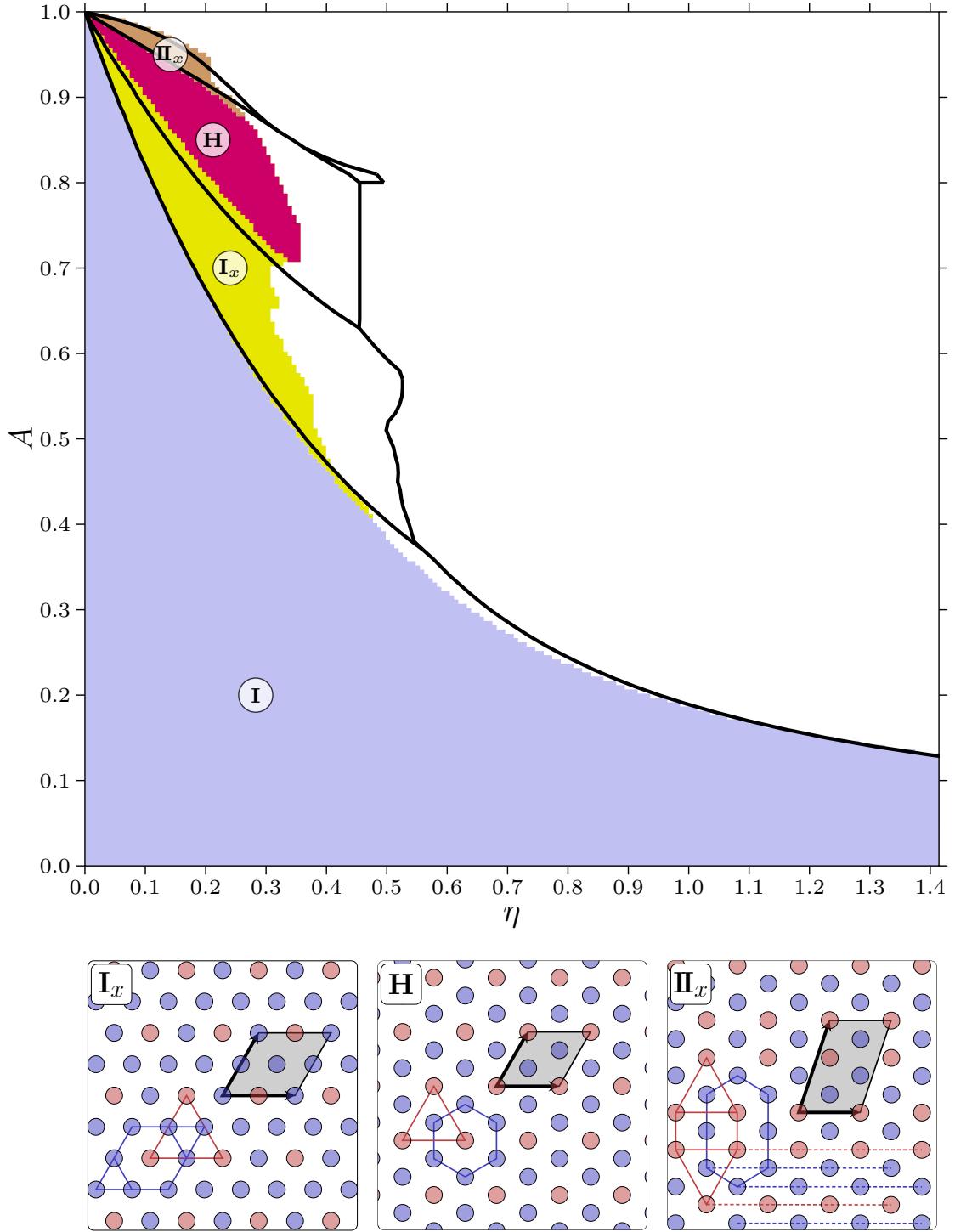
Figure 3.16.: Structures based on the "out"-mechanism: structures I_x, H, and II_x (see text).
Top panel: regions of stability of the respective structures. For small values
of x, i.e., in particular close to the boundary with structure I, we observe
structure I_x (yellow region). Structure H (pink region) is a special case with
$x = 1/3$ and represents the transition to structure II_x (brown region), which
– in turn – shares some of the features of structure II. Only a limited number
of candidate structures could be considered in the analytical approach (black
lines). **Bottom row:** snapshots of the respective structures. Particles in layer
1 are colored blue, particles in layer 2 red. Left panel: snapshot of structure
I_x for $\eta = 0.184$ and $A = 0.775$, where $x = 1/4$. Center panel: snapshot of
structure H for $\eta = 0.198$ and $A = 0.85$, where $x = 1/3$. Right panel: snapshot
of structure II_x for $\eta = 0.148$ and $A = 0.95$, where $x = 2/5 = 0.4$.

Structures based on the "in"-branch: structure V_x

The structure based on the "in"-branch in Section 3.2 (which we denote structure V_x) is dominant for small values of A and especially for large values of η. The top panel of Figure 3.17 shows its region of stability. We denote it structure V_x since it maintains many of the defining characteristics of structure V. In particular, both layers are almost perfectly hexagonal and the interaction between the two layers is small. We can define structure V_x using the modified bond-orientational order parameter: $(1 - x)\Psi_6^{(1)} + x\Psi_6^{(2)} > 0.9$. In the limiting case $\eta \to \infty$, the order parameter x approaches its asymptotic value $x_{\mathrm{asy}} = A/(1+A)$ from below. The bottom panels of Figure 3.17 show snapshots of structure V_x. In many – but not all – cases, particles in layer 2 are positioned above the centers of triangles in layer 1. Note that slight distortions are common for intermediate values of η, while the two layers form almost uncorrelated hexagonal lattices for large values of η, thereby creating a moiré-like pattern [5].

In the analytical approach, both layers are assumed to be perfectly hexagonal, albeit with different densities. The correlation of the two-dimensional lattices in the two layers is neglected and x is thus continuous and not discretized (see Equation 3.21).

Structures with $x = 1/2$: structures II, III, and IV

As mentioned before, for $A < 1$ structure I occupies a large portion of the phase diagram while structure V is immediately replaced by structure V_x (as shown by analytical calculations) as A deviates from the value of one. Interestingly, also the three other structures observed in the symmetric case play a prominent role in the asymmetric case. The top panel of Figure 3.18 shows the stability ranges of structures II, III, and IV; the limiting case $A \to 1$ is well reproduced.

A very interesting effect occurring for these three structures is that the net charge of the two layers is reversed compared to all other regions of the phase diagram. Since we usually observe $x < x_{\mathrm{asy}}$, layer 1 most often carries more point charges than would be required to compensate for the neutralizing background, leading thus to a negative net charge; layer 2 correspondingly carries a positive net charge. For the three symmetric structures, we observe charge inversion $x = 1/2 > x_{\mathrm{asy}}$, i.e., layer 2 is *overcharged* and has a negative net charge. As a consequence, $x = x(\eta)$ exhibits non-monotonic behavior. We discuss this phenomenon in more detail once we have finished constructing the phase diagram.
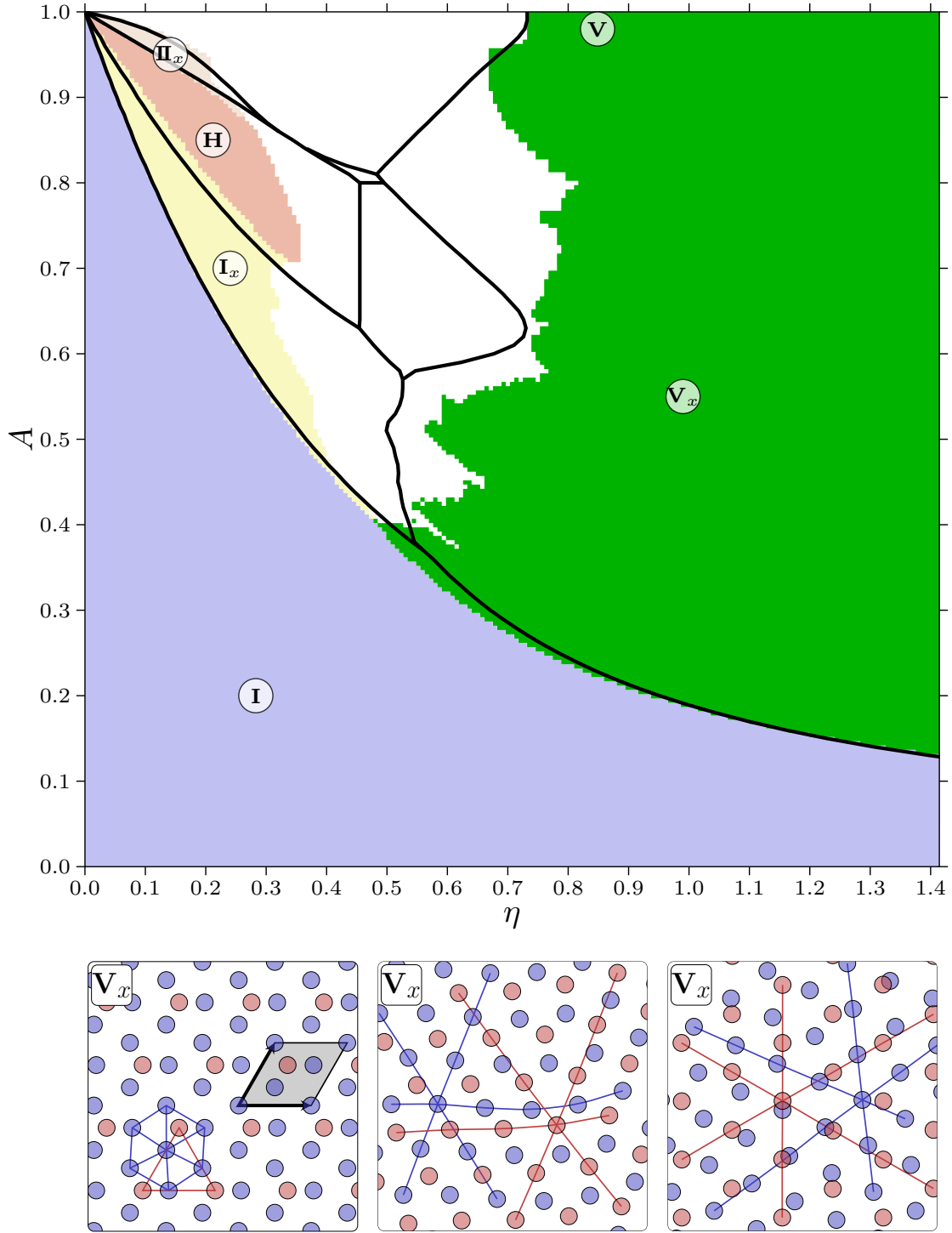
Figure 3.17.: Destabilization of structure I via the "in"-mechanism: structure V_x. **Top panel:** region of stability of structure V_x (green region). Black lines mark the respective regions of stability determined with the analytical approach, where only a limited number of candidate structures is considered. **Bottom row:** left panel: snapshot of structure V_x for $\eta = 0.707$ and $A = 0.5$, where $x = 1/4$. This allows for perfect commensurability. Center panel: snapshot of structure V_x for $\eta = 0.7$ and $A = 0.9$, where $x = 13/28 = 0.464$. Note the wave-like modulation of the hexagonal lattices. Right panel: snapshot of structure V_x for $\eta = 1.061$ and $A = 0.7$, where $x = 12/31 = 0.387$. For large η, there is little correlation between the two layers, leading to a moiré pattern. Particles in layer 1 are colored blue, particles in layer 2 red.
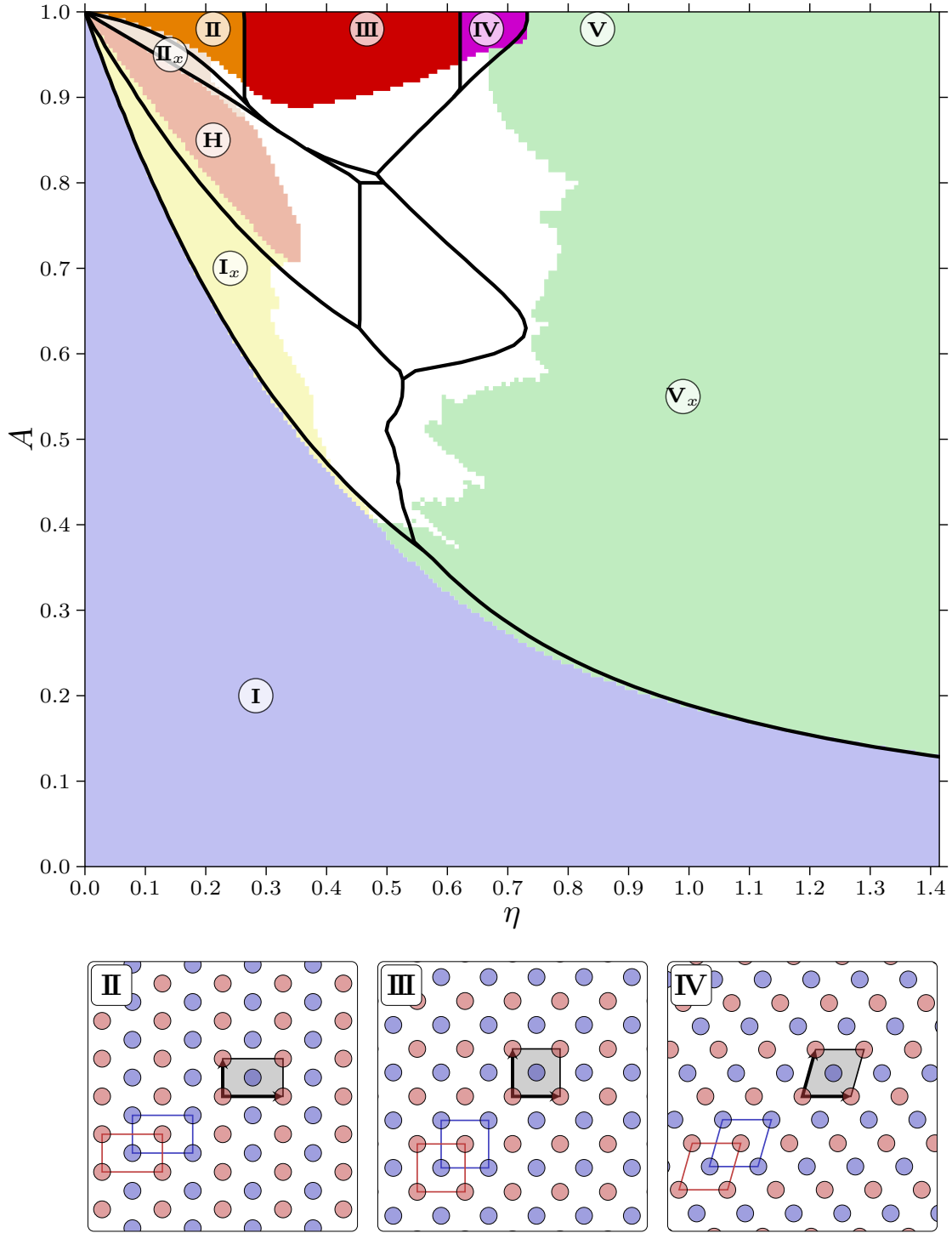
Figure 3.18.: Stability of the symmetric structures for $A < 1$: structures II, III, and IV. **Top panel:** regions of stability of the respective structures. Structures II (orange region), III (red region), and IV (purple region) remain stable even for $A < 1$. In particular, we observe structure III for as low as $A \approx 0.89$. The three symmetric structures are of particular interest as they exhibit *overcharging*, i.e., the net charge of top and bottom layer changes sign and $x(\eta)$ is non-monotonic. Black lines mark the respective regions of stability determined with the analytical approach, where only a limited number of candidate structures is considered. **Bottom row:** snapshots of the respective structures. Particles in layer 1 are colored blue, particles in layer 2 red. Left panel: snapshot of structure II for $\eta = 0.134$ and $A = 1$. Center panel: snapshot of structure III for $\eta = 0.445$ and $A = 1$. Right panel: snapshot of structure IV for $\eta = 1.414$ and $A = 1$.
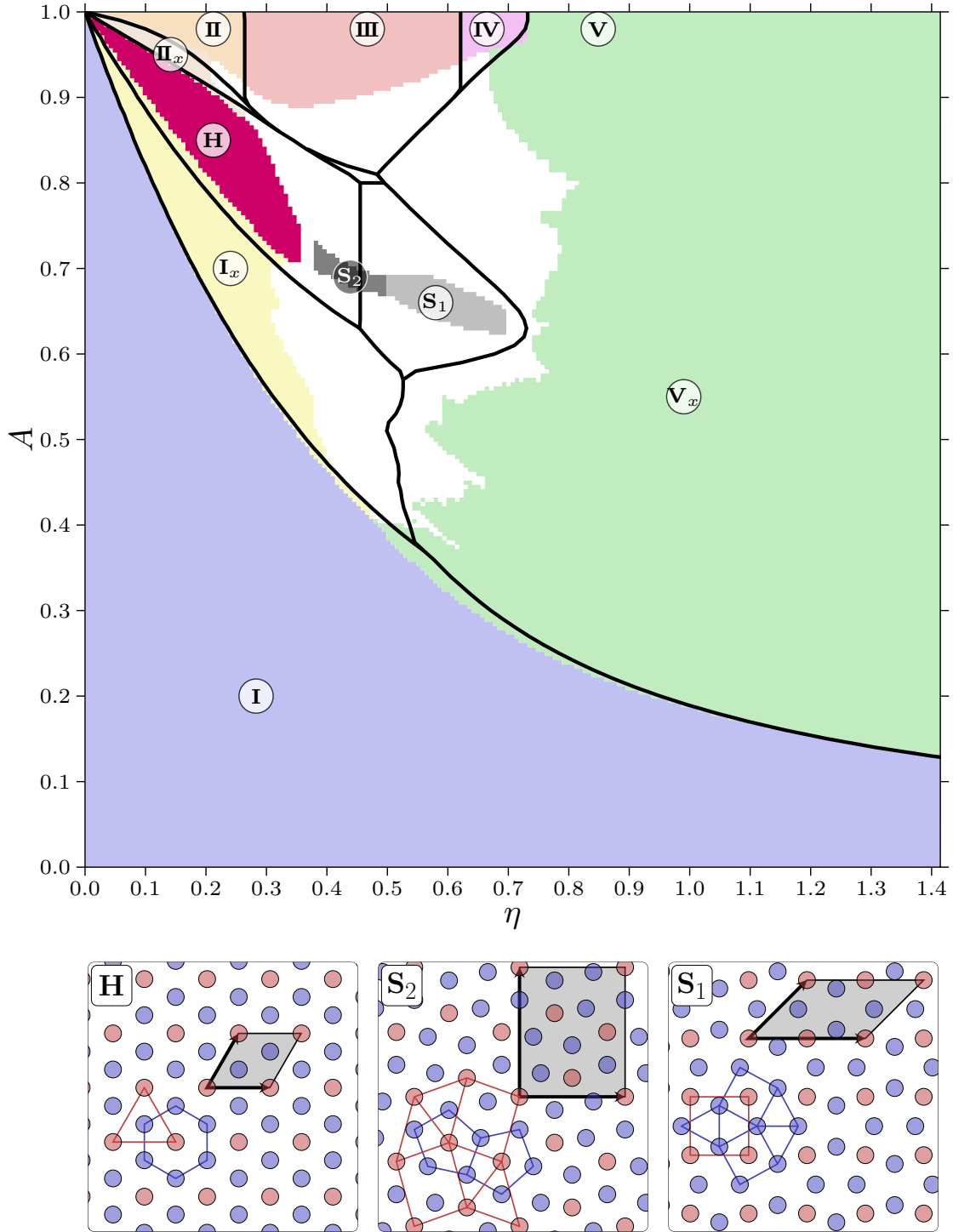
Figure 3.19.: Structures with $x = 1/3$: phases H, S_2, and S_1. **Top panel:** regions of stability of the respective structures. Phase H conforms to the I_x-formalism (pink region). Phases S_2 (dark gray region) and S_1 (light gray region) have more complicated geometric features. Black lines mark the respective regions of stability determined with the analytical approach, where only a limited number of candidate structures can be considered. Structure S_2 could not be treated within the analytical approach (indicated by a dark label). **Bottom row:** snapshots of the respective structures. Particles in layer 1 are colored blue, particles in layer 2 red. Left panel: snapshot of structure H for $\eta = 0.198$ and $A = 0.85$. Center panel: snapshot of structure S_2 for $\eta = 0.417$ and $A = 0.7$. Right panel: snapshot of structure S_1 for $\eta = 0.622$ and $A = 0.675$.

Structures with $x = 1/3$: structures H, S_1, and S_2

In addition to the previously discussed honeycomb structure H, we observe two other major structures with $x = 1/3$ for larger plate separations η. Due to their unique lattices, we denote these structures the snub square structures S_1 and S_2. The top panel of Figure 3.19 shows the stability regions of the two structures. Note that due to its more intricate particle arrangement, phase S_2 could not be treated within the analytical approach. The two structures are characterized by the following geometric features:

- Structure S_1 consists of a slightly distorted snub square particle arrangement (consisting of squares and equilateral triangles) in layer 1. Particles in layer 2 are positioned above the centers of the squares in layer 1 and thus form a square lattice (see bottom right panel of Figure 3.19). We can identify structure S_1 using $x = 1/3$, $\Psi_5^{(1)} > 0.9$, and $\Psi_4^{(2)} > 0.9$.
- Structure S_2 consists of a strongly distorted snub square particle arrangement in layer 2 and pentagonal structural units in layer 1 (see bottom center panel of Figure 3.19). While the snub square lattice is obviously less clean, structure S_2 still occupies a significant region in the phase diagram. Thus phase S_2 can be specified via $x = 1/3$ and $\Psi_5^{(2)} > 0.45$.
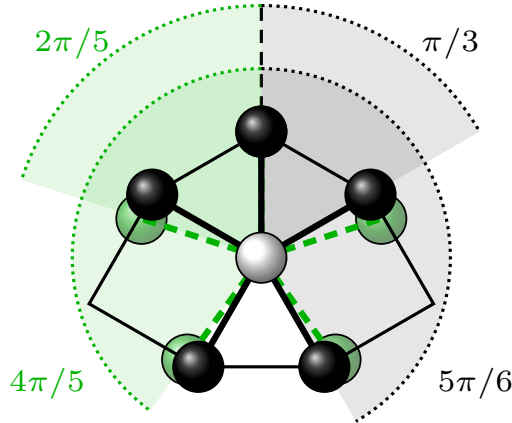

Figure 3.20.: Schematic view of the neighborhood of a particle in the snub square tiling. Going clockwise from the top, each vertex is formed by the following sequence of surrounding polygons: $\triangle - \square - \triangle - \square - \triangle$. The respective bond angles (indicated by dotted black lines) are close to the ones of a pentagonal arrangement (indicated by the green particles and the dotted green lines).

The reason why snub square lattices produce a significant five-fold BOOP Ψ_5 is related to the angles required for the formation of such a lattice. As in all Archimedean tilings, each vertex (represented by a particle) in the snub square tiling has the same surrounding geometry. Since the polygons meeting at each vertex form the characteristic sequence $\triangle - \square - \triangle - \square - \triangle$,

---

5. Moiré patterns are created by superposition of two simple lattices. Depending on the commensurability and the relative orientation of the two lattices, highly complex patterns can emerge.

the relevant bond angles are (see dotted black lines in Figure 3.20)

$$\phi_{\text{sn.sq.}} = \begin{cases} 0 \\ \pm\frac{\pi}{3} \approx \pm 0.333\pi \\ \pm\frac{5\pi}{6} \approx \pm 0.833\pi \end{cases} . \tag{3.57}$$

These are very close to the bond angles of pentagonal arrangement (see dotted green lines in Figure 3.20)

$$\phi_{\text{pent.}} = \begin{cases} 0 \\ \pm\frac{2\pi}{5} = \pm 0.400\pi \\ \pm\frac{4\pi}{5} = \pm 0.800\pi \end{cases} . \tag{3.58}$$

In the analytical approach, structure S_1 is assumed to have a perfect snub square lattice in layer 1 and a perfect square arrangement in layer 2. While the number of particles per cell $N = 6$ is relatively small for numerical calculations, it hits the limit for the analytical approach since each explicit particle position (independent of the lattice periodicity) requires evaluation of an additional integral in the calculation of the energy. For structure S_2, this problem becomes even more pronounced since $N = 12$; thus it could not be included in the analytical approach (indicated by a dark label in the phase diagram).

Structures with pentagonal features: structures P_1, P_2, and P_3

The structures in the remaining regions of the phase diagram exhibit complicated geometries and symmetries which prohibit an analytical treatment. These particular particle arrangements tend to change continuously as a function of η and A, making the classification of distinct structures difficult. However, we observe several regions where the order parameters indicate the occurrence of distinct mechanisms. We have particular interest in structures with pentagonal features due to their importance with respect to possible formation of quasi-crystals. Figure 3.22 shows the regions of stability of three observed pentagonal structures:

- Structure P_1 has a complicated particle arrangement and exhibits a significant five-fold symmetry in layer 2 (see left panel of Figure 3.21); we can identify phase P_1 with $1/3 < x < 1/2$ and $\Psi_5^{(2)} > 0.45$.
- Structure P_2 consists of a large number of pentagonal holes, i.e., a large part of particles in layer 2 occupies positions above centers of pentagons in layer 1 (see center panel of Figure 3.21). In addition, particles in layer 2 form a rather well-defined hexagonal lattice. We can identify phase P_2 with $1/3 < x < 1/2$ and $\Psi_5^{(4)} > 0.9$.
- Similarly, structure P_3 consists of a large number of pentagonal holes, albeit at a much lower density (see right panel of Figure 3.21). We can identify phase P_3 with $0 < x < 1/3$ and $\Psi_5^{(4)} > 0.45$.

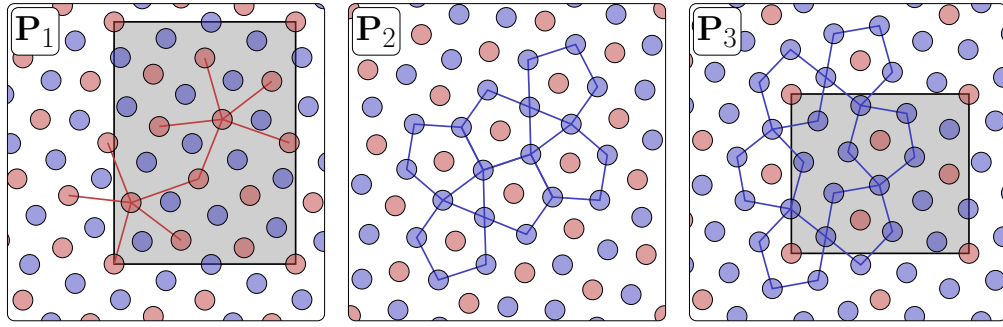Structures with pentagonal features could not be treated within the analytical approach.

Figure 3.21.: Snapshots of structures with pentagonal features identified using BOOPs: structures P_1, P_2, and P_3. The respective regions of stability are shown in Figure 3.22. They appear as contiguously colored regions in the ΨRGB-phase diagrams (see Figure 3.25). Structures P_1 and P_2 appear for $x > 1/3$, where they compete with structures III and H. Structure P_3 exhibits $x < 1/3$ and strongly competes with structure I_x; it may also be important close to the critical point (marked by a circled asterisk). Structures of these types are not included in the analytical approach (indicated by dark labels). Particles in layer 1 are colored blue, particles in layer 2 red. Left panel: snapshot of structure P_1 for $\eta = 0.381$ and $A = 0.85$, where $x = 12/28 = 0.429$. Center panel: snapshot of structure P_2 for $\eta = 0.346$ and $A = 0.825$, where $x = 3/8 = 0.375$. Right panel: snapshot of structure P_3 for $\eta = 0.410$ and $A = 0.6$, where $x = 4/18 = 0.222$.

Full phase diagrams

Figure 3.22 shows the phase diagram obtained with the EA and the analytical approach, including all structures that have been discussed so far. As can be seen, a white region of significant extent – populated by structures that could not be properly classified – remains. While the analytical approach covers the general features of the phase diagram, it is unable to treat the more complicated features surrounding the white region. The definitions of the classified structures are summarized in Table 3.3.

We can illustrate the difficulties arising in the remaining white regions of the phase diagram when color-coding the state points in the (η, A)-plane by the number of particles per cell of the observed ground state structures in the EA approach (see Figure 3.23). We observe at times abrupt changes in cell size for a variety of reasons. Bright regions in general imply simple lattice structures (with few particles per unit cell) and usually a strong correlation between the two layers, often resulting in a discrete set of preferred values of x (see Figure 3.24). Dark regions, however, not necessarily indicate complicated structures, but can also imply continuously changing values $x(\eta)$.

In order to obtain additional information on phases that populate the white region, we generate plots of the (η, A)-plane, where the order parameters of each state point are illustrated using using an RGB color scheme. Since we are interested in four-, five-, and six-fold sym-
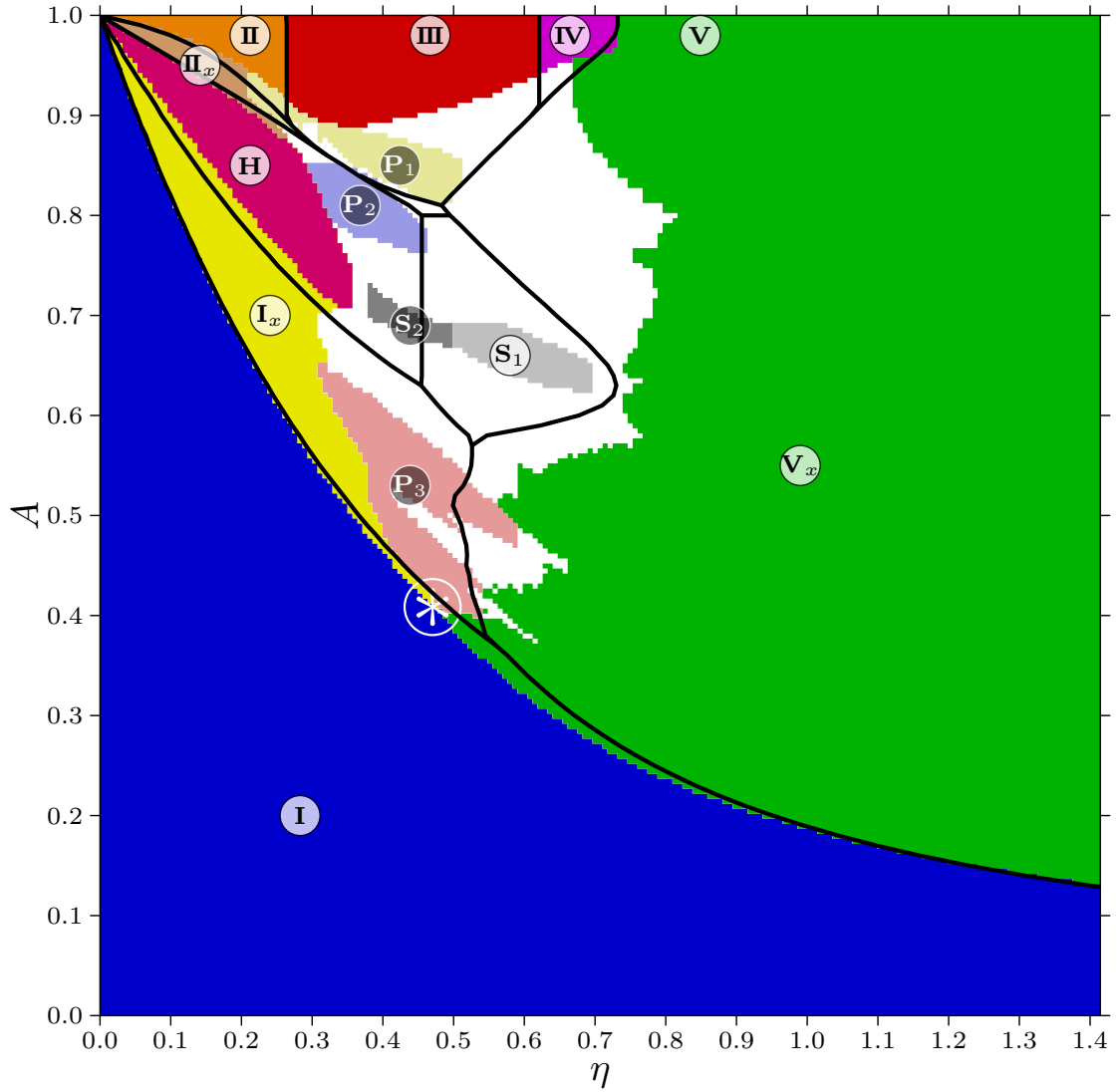
Figure 3.22.: Full phase diagram showing all structures identified in the preceding subsub-sections (as labeled). Structures that could be treated within the analytical approach have light labels. Black lines mark the respective regions of stability determined with the analytical approach. Structures with dark labels are too complicated to be treated within the analytical approach. White regions indicate structures with more complicated geometric features, some of which may be characterized by specific color combinations in the ΨRGB-phase diagrams (see Figure 3.25).
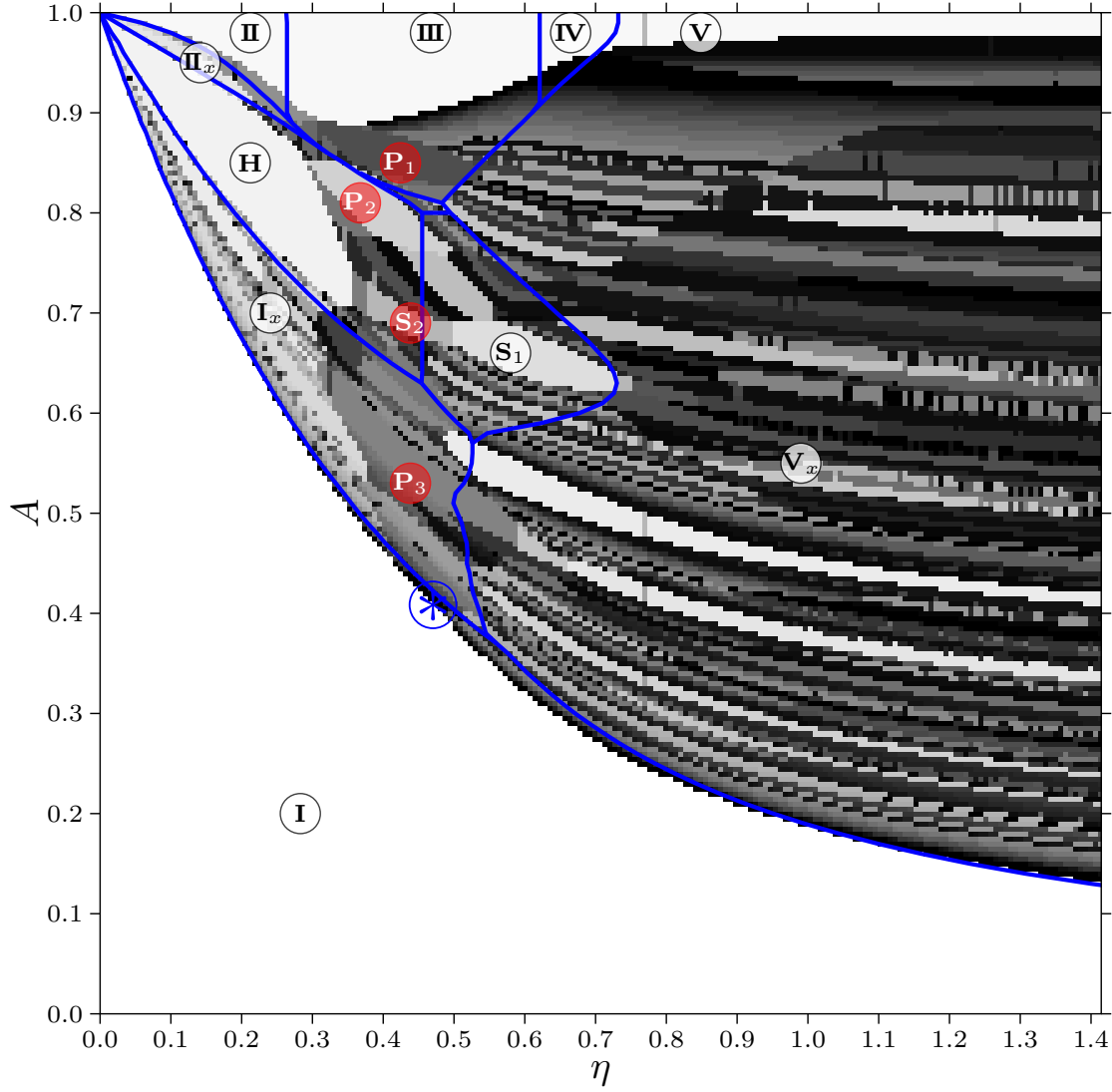
Figure 3.23.: Number N of particles per cell for the observed ground state structures in the (η, A)-plane in the EA approach using a grayscale encoding: $N = 2$ corresponds to white, $N = 40$ to black. Simple structures that are easily treatable with the analytical approach (blue lines and bright labels) appear as bright regions. Structure V_x poses an exception to this since the layers are not necessarily strongly correlated here. Note that parts of the phase diagram – in particular the white region – exhibit large cells and continuously changing structures.
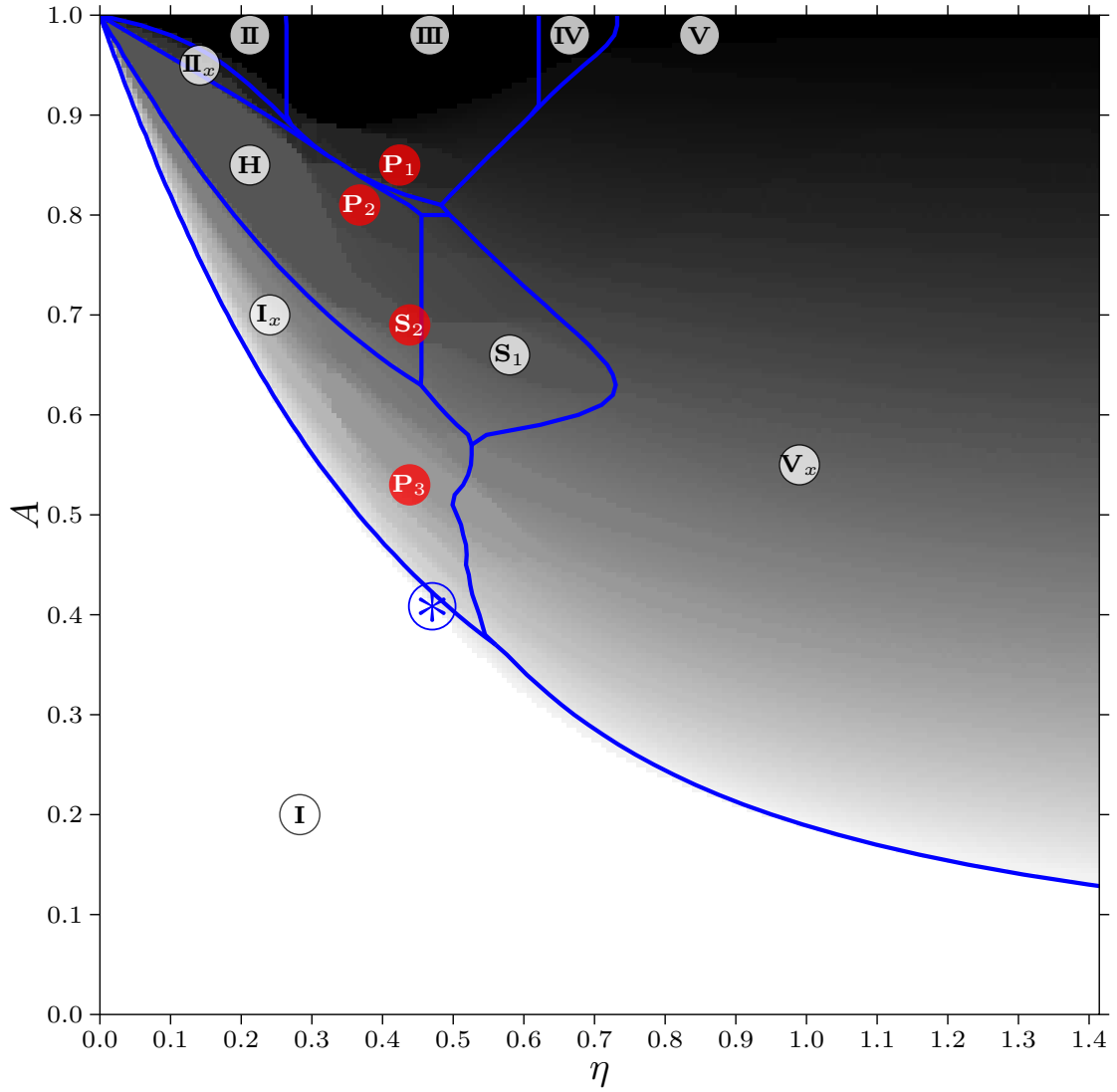
Figure 3.24.: Order parameter $x = \rho_2/\rho$ for the observed ground state structures in the (η, A)-plane in the EA approach using a grayscale encoding: $x = 0$ corresponds to white, $x = 1/2$ to black. Certain discrete values are preferred and appear as plateaus. Note the especially interesting value $x = 1/3$ (region surrounding the labels of structures H, S_2, and S_1).
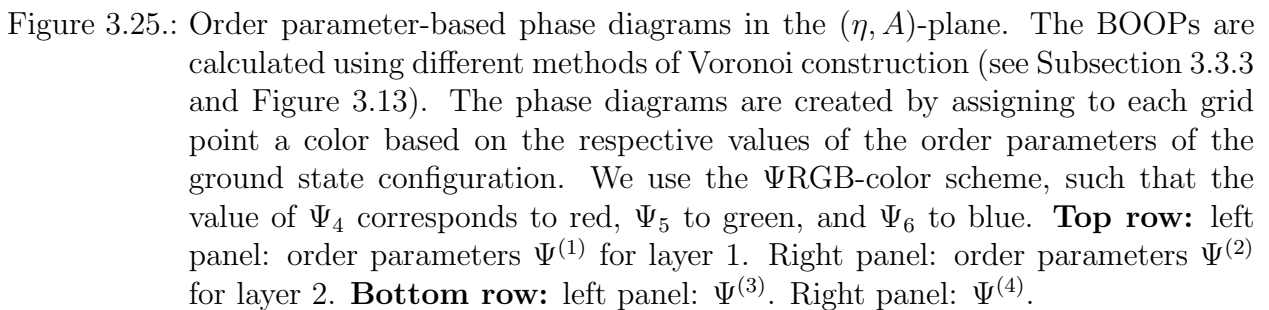
Table 3.3.: Observed structures in the asymmetric Wigner bilayer system and their characteristic features. For the classification, we first decide by the value of x (second column) and then further refine using BOOPs (third column). Note that the cutoff values for the order parameters are to some extent arbitrary, but fit well with distinctly colored regions in Figure 3.25.

I	$x = 0$		hexagonal monolayer
II	$x = 1/2$	$\Psi_4^{(1,2)} = 1,\ 0 < \Psi_6^{(1,2)} < 1$	rectangular bilayer
III	$x = 1/2$	$\Psi_4^{(1,2)} = 1,\ \Psi_6^{(1,2)} = 0$	square bilayer
IV	$x = 1/2$	$0 < \Psi_4^{(1,2)} < 1,\ 0 < \Psi_6^{(1,2)} < 1$	rhombic bilayer
V	$x = 1/2$	$\Psi_4^{(1,2)} = 0,\ \Psi_6^{(1,2)} = 1$	hexagonal bilayer
I_x	$0 < x < 1/3$	$\Psi_6^{(3)} > 0.9$	
H	$x = 1/3$	$\Psi_6^{(3)} > 0.9$	honeycomb (layer 2)
II_x	$1/3 < x < 1/2$	$\Psi_6^{(3)} > 0.9$	
V_x	$0 < x < x_{\mathrm{asy}}$	$(1-x)\Psi_6^{(1)} + x\Psi_6^{(2)} > 0.9$	hexagonal bilayer
S_1	$x = 2/6$	$\Psi_5^{(1)} > 0.9,\ \Psi_4^{(2)} > 0.9$	snub square (layer 1)
S_2	$x = 4/12$	$\Psi_5^{(2)} > 0.45$	snub square (layer 2)
P_1	$1/3 < x < 1/2$	$\Psi_5^{(2)} > 0.45$	pentagonal (layer 2)
P_2	$1/3 < x < 1/2$	$\Psi_5^{(4)} > 0.9$	pentagonal holes
P_3	$0 < x < 1/3$	$\Psi_5^{(4)} > 0.9$	pentagonal holes

metries, we associate Ψ_4 to the *red-*, Ψ_5 to the *green-*, and Ψ_6 to the *blue*-values, respectively. This scheme allows for an easy visualization of several order parameters at once, allowing us to perceive distinctly colored regions more easily (which may indicate a distinct mechanism). Figure 3.25 shows such ΨRGB phase diagrams for the four different Voronoi constructions presented in Subsection 3.3.3.

Stability of the monolayer

We now proceed to the discussion of a few interesting phenomena in the phase diagram. The first of these is directly related to the problem presented in Section 3.2. There, we were interested in the transition from a monolayer to an extremely diluted bilayer. In the asymmetric bilayer Wigner system, this corresponds to the line where x assumes an infinitesimal positive value, i.e., the upper boundary of structure I. As we have seen in the phase diagram (see Figure 3.22), structure I competes only with structures I_x and V_x, which correspond to the "out"- and "in"-branches, respectively. The tricritical point where these three stability regions meet can be calculated within the EM approach by comparing the energy curves obtained for the two branches in Section 3.2 to structure I using Equation

Figure 3.25.: Order parameter-based phase diagrams in the (η, A)-plane. The BOOPs are calculated using different methods of Voronoi construction (see Subsection 3.3.3 and Figure 3.13). The phase diagrams are created by assigning to each grid point a color based on the respective values of the order parameters of the ground state configuration. We use the ΨRGB-color scheme, such that the value of Ψ_4 corresponds to red, Ψ_5 to green, and Ψ_6 to blue. **Top row:** left panel: order parameters $\Psi^{(1)}$ for layer 1. Right panel: order parameters $\Psi^{(2)}$ for layer 2. **Bottom row:** left panel: $\Psi^{(3)}$. Right panel: $\Psi^{(4)}$.

3.52; we obtain (see circled white asterisk in Figure 3.22)

$$\eta_{\rm c} = 0.470 \qquad\qquad (3.59)$$
$$A_{\rm c} = 0.4085. \qquad\qquad (3.60)$$

This compares reasonably well to the values obtained with the EA approach, where we use smaller cell sizes than in the EM approach (up to $N = 40$ particles per cell)

$$\eta_{\rm c} = 0.477 \qquad\qquad (3.61)$$
$$A_{\rm c} = 0.4075. \qquad\qquad (3.62)$$

The EA results imply that the region of stability of structure P_3 also reaches this tricritical point. This might be an indication that structure P_3 represents a transition phase between structures I_x and V_x. However, our resolution in the EA approach is too small for a closer study of this phenomenon and the complicated geometry of structure P_3 precludes a more accurate analytical investigation.

Close to the tricritical point, deformations in structure I_x and V_x are most pronounced for the iso-line $x \approx 0$. For structure I_x, η can be considered large, causing the holes left by those particles that moved to layer 2 to contract significantly. For structure V_x, η can be considered small and the triangles in layer 1 surrounding particles in layer 2 distort significantly. Since both of these distortions are neglected in the analytical approach, the boundaries between structure I and structures I_x and V_x differ noticeably (see Figure 3.22). However, agreement is excellent both for small and large η-values, where distortions are small.

The left panel of Figure 3.26 shows the $x(\eta)$-curve for $A = 0.93$, along which we identify structures I, I_x, H, II_x, P_1, II, III, a range of unclassified structures and finally structure V_x. For now, we study only the part where $x < 1/3$, i.e., the region where structure I_x is stable. As we know, certain values $x = 1/N_{\rm out}$ are preferred for structure I_x since they allow a commensurate hexagonal particle arrangement in layer 2 (see Equation 3.19). As a consequence, $x(\eta)$ is not a continuous function in the analytical approach, but rather staircase-like (for $A = 0.93$ we observe $x = 1/7, 1/4, 1/3$). For A close to unity, $x(\eta)$ grows very quickly and the plateaus are very thin.

For smaller values of $A \approx 0.6$ (not shown), we observe more pronounced plateaus, which can become smeared out as $x(\eta)$ becomes more continuous once deformations come into play. The competition between preferred *discrete* values of x and a *continuous* increase $x(\eta)$ can serve as an explanation for the intricate shape of the upper boundary between structures I_x and P_3 (see Figure 3.22), which undulates back and forth with decreasing A.

The analytical approach predicts that the transition I→I_x is of second order with a critical exponent for the order parameter x of $\beta = 2/3$

$$x(\eta) \quad \sim \quad [\eta - \eta_{\rm c}(A)]^{2/3}. \qquad\qquad (3.63)$$
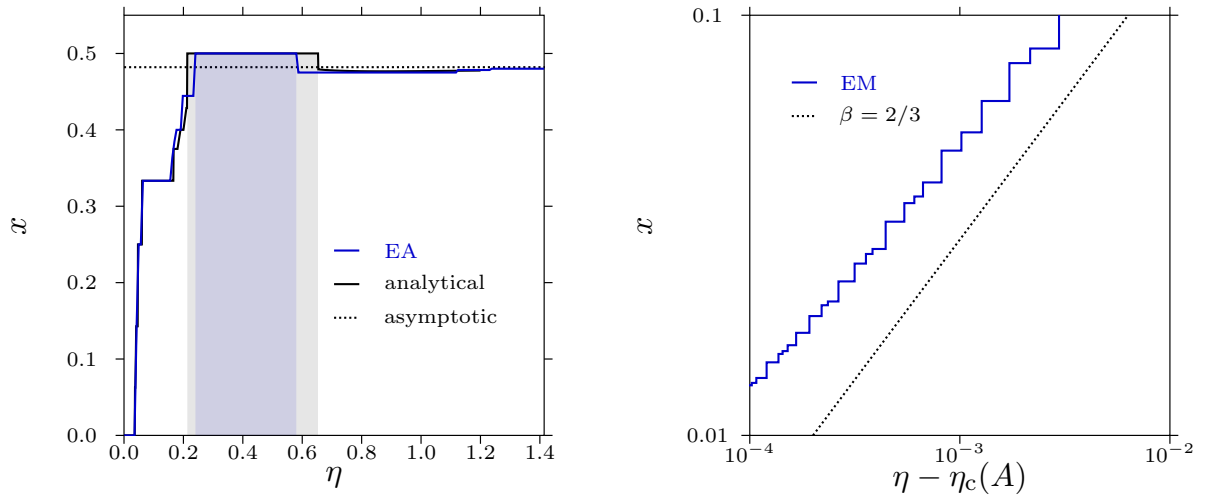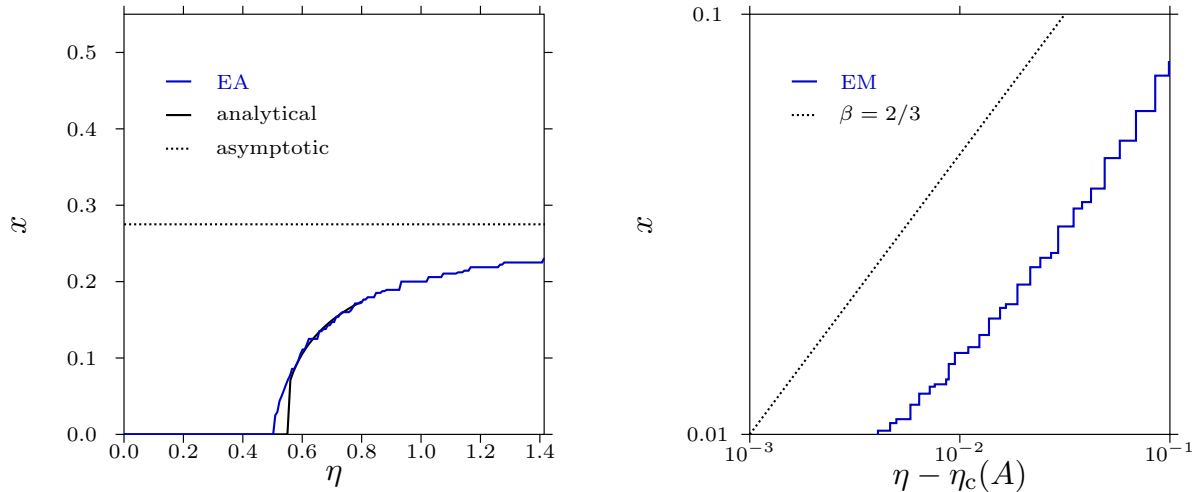
Figure 3.26.: $x(\eta)$ for $A = 0.93$. Left panel: curve over the entire considered range of η. EA results in blue, analytical results in black. In the region of stability of structure I$_x$ (where $x < 1/3$), a discrete set of compatible x-values (see N_{out} in Equation 3.19) is preferred, evidenced by a staircase-like form of the curve; regions of constant x are very thin for A this close to unity. However, non-compatible values are also possible in the EA approach. Shaded areas indicate overcharging, i.e., where $x > x_{\text{asy}}$. Right panel: double-logarithmic plot of $x(\eta - \eta_{\text{c}})$. The dotted black line is a guide to the eye, indicating a critical exponent $\beta = 2/3$ (see Equation 3.63).

While we can not directly calculate the critical exponent from either our EA data nor from our EM data, we can use them to corroborate this prediction. The right panel of Figure 3.26 shows $x(\eta)$ close to the transition I→I$_x$. Note that even small numerical inaccuracies in η_c or the energy calculation can severely change the slope in a double-logarithmic representation. However, the observed shape of $x(\eta)$ does seem compatible with the analytical prediction.

We now proceed to the case of rather small values of A. The left panel of Figure 3.27 shows the $x(\eta)$-curve for $A = 0.38$, along which we identify structures I and V$_x$. While we know that some preferred values $x = 1/N_{\mathrm{in}}$ exist for structure V$_x$ (see Equation 3.21), the $x(\eta)$-curve is basically continuous and smooth; the reason for this is that η is already quite large at the transition, leading to a rather weak interaction between the two layers. Interestingly, $x(\eta)$ appears to converge only very slowly towards the asymptotic value x_{asy}. As mentioned before, deformations are rather well pronounced since we are close to the tricritical point (evidenced by a visible difference in η_c between EA and analytical results).

Figure 3.27.: $x(\eta)$ for $A = 0.38$. Left panel: curve over the entire considered range of η (compare Figure 3.26). EA results in blue, analytical results in black. As η_c is rather large, the two layers are not strongly correlated, leading to a smooth curve $x(\eta)$. The asymptotic value x_{asy} is indicated by a dotted line. Note the visible difference in η_c between the two approaches; this difference is due to deformations, which are rather strongly pronounced in structure V$_x$ this close to the tricritical point (see also Figure 3.22). Right panel: double-logarithmic plot of $x(\eta - \eta_c)$. The dotted black line is a guide to the eye, indicating a critical exponent $\beta = 2/3$.

The analytical approach predicts the transition I→V$_x$ to be of first order with an associated jump in x from zero to a finite value. This discontinuity is most distinct close to the tricritical point. However, the EA and EM results predict the transition to be of second order. We can again try to obtain more information on this critical behavior by computing $x(\eta)$ close

to the transition (see right panel of Figure 3.27). Data are much less accurate here, but it appears that our results would again be compatible with a critical exponent $\beta = 2/3$.

Overcharging

The second interesting phenomenon is overcharging. In significant parts of the phase diagram, the symmetric structures II, III, and IV are stable (see Figure 3.22). Since these structures are characterized by $x = 1/2 > x_{\mathrm{asy}}$ for $A < 1$, the net charge of the two plates changes sign compared to all other regions in the phase diagram. In most regions of the phase diagram, the stronger (positive) background on plate 1 causes the majority of the (negative) point charges to be in layer 1, resulting in net charges

$$\sigma_1 + Q\rho_1 = \left(\frac{1}{1+A} - (1-x)\right)\sigma \;\; < \;\; 0 \tag{3.64}$$

$$\sigma_2 + Q\rho_2 = \left(\frac{A}{1+A} - x\right)\sigma \;\; > \;\; 0. \tag{3.65}$$

This energetically unfavorable value of x again exemplifies the strong competition between two opposing principles:

Commensurability When the two layers are strongly correlated, the commensurability of the particle arrangements in the two layers is the dominant factor. This favors *discrete values* of x which result in commensurate lattices. Otherwise, strong distortions are required to avoid unfavorable inter-layer interactions. This principle is dominant for small values of η.

Effective charge When correlation between the two layers is weak, the interaction between the effective charges (particles plus background) of the two layers is the dominant factor. If we consider structure V_x in the case of large plate separation $\eta \gg 1$, the energy per particle in the analytical approach is given by [173]

$$\frac{E^*_{\eta \gg 1}}{N} \;\; = \;\; c_{\mathrm{m}} \left[(1-x)^{3/2} + x^{3/2}\right] + 2^{3/2}\pi\eta \left(x - \frac{A}{1+A}\right)^2. \tag{3.66}$$

This expression assumes that both layers are hexagonal and that their lattices are uncorrelated. The first term in Equation 3.66 on the left side is merely the energy of the two (isolated) hexagonal layers, whereas the second term gives the interaction between the *effective* plate charges $\sigma_{\mathrm{eff}} = \rho Q[x - A/(1+A)]$, i.e., of background and point charges combined. The value of x for which $E^*_{\eta \gg 1}$ reaches its minimum is a continuous function in η and A.

The system thus tries to achieve a favorable value $x(\eta, A)$, favoring a smooth curve and a *continuous increase* in x as η or A increase. This principle is dominant for large values of η.

In the case of the symmetric structures (characterized by $x = 1/2$), the first principle is

decisively dominant. As x increases above the asymptotic value x_{asy}, $x(\eta)$ further acquires non-monotonic features (see left panel of Figure 3.26).

We point out that our numerical resolution in the EA approach is limited regarding x. In particular, the largest value of $x < 1/2$ obtainable is $x = 19/39 = 0.487$. It is possible that significantly larger system sizes could allow for both a good value of x and a more complicated two-dimensional particle arrangement.

Additional details of structure V$_x$

We now turn to the discussion of additional details of structure V$_x$. While we make no distinction between structures V and V$_x$ in the phase diagram, we point out that the analytical approach clearly shows that $x = 1/2$ is only obtained for $A = 1$. Due to the limited numerical resolution regarding x in the EA approach, we observe structure V also for a small region $A < 1$ (as can be seen in Figure 3.23 since structure V requires only two particles per cell and is thus visible as a bright region close to $A = 1$).

The lower boundary of structure V$_x$ (see Figure 3.22) undulates back and forth with decreasing A. Again, we can relate this phenomenon to preferred values of x, which necessitate fewer distortions (see Figures 3.23 and 3.25). There is, however, a pronounced region where a distinct mechanism appears to be at work. For $A \gtrsim 0.8$, the ΨRGB phase diagrams (see Figure 3.25) show a region in structure V$_x$ where the color changes smoothly. A closer look at the corresponding snapshots reveals a wave-like modulation of the hexagonal lattices in the two layers, allowing for a good correlation between the lattices in the two layers without significantly decreasing the hexagonal order of either layer or preventing a favorable value of x (see bottom center panel of Figure 3.17). A different mechanism is at work for structures V$_x$ for $A \lesssim 0.8$, where the two lattices are mostly uncorrelated, leading to moiré patterns (see bottom right panel of Figure 3.17).

In the symmetric case, where both layers are locally electro-neutral, the interaction between the two plates decays exponentially [150, 157]. In the asymmetric case, the analytical results show that the two layers remain charged for arbitrarily large plate separation η. In particular for small values of A, $x(\eta)$ converges very slowly towards the asymptotic value x_{asy} for large η (see left panel of Figure 3.27). The remaining effective interaction between the two plates decays algebraically $\sim 1/\eta^2$ [173].

3.3.5. Results at finite temperature

As mentioned in Subsection 3.3.2, frustration between the lattices in the two layers and the value of x can pose a problem for correct equilibration of the Wigner bilayer system and an unfavorable choice of the initial configuration can prevent the ground state structure from
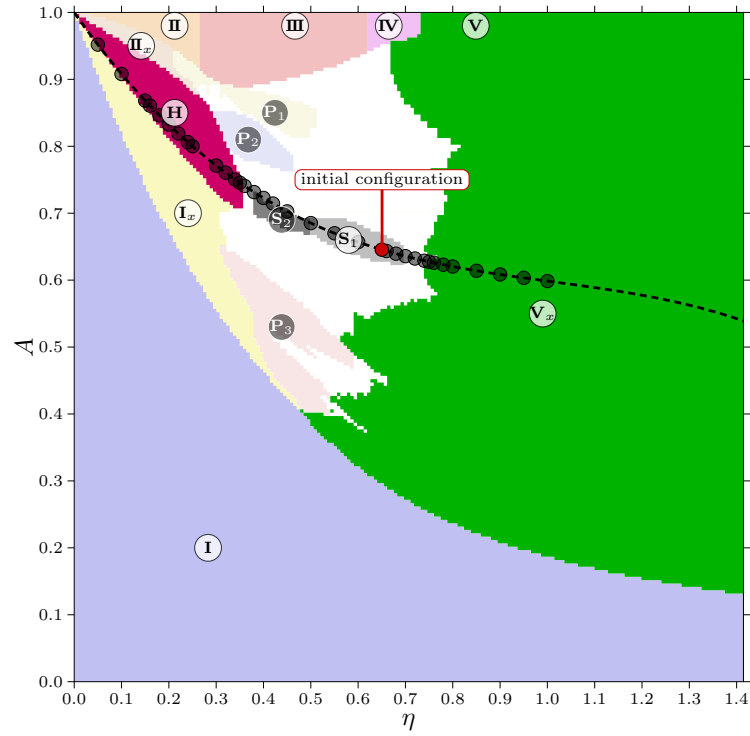
Figure 3.28.: State points investigated with MC simulations (indicated by black dots). We use a rough interpolation line $[A(\eta) = 1 - 1.00749\eta + 0.905807\eta^2 - 0.299731\eta^3]$ (dashed line), along which $x \approx 1/3$. The red dot indicates the S_1-configuration obtained with the EA used for initialization of the simulation. Note that along a small section of this line, the EA predicts $x \neq 1/3$, a feature which is confirmed by the MC simulations.

being formed even for very large coupling constant Γ. However, this problem all but disappears if we choose an initial configuration with a similar value of x as the predicted ground state structure, even though the two-dimensional particle arrangement may be different.

For the results presented in this section, we focus on the case $x = 1/3$, for which we have classified via the EA approach a sequence of four different distinct structures with increasing η and decreasing A, namely H, S_2, S_1, and V_x; in addition, some unclassified regions with more complicated structures remain. Figure 3.28 shows the investigated state points in the (η, A)-plane chosen for MC simulations. These lie along an interpolated line $x \approx 1/3$

$$A(\eta) = 1 - 1.00749\eta + 0.905807\eta^2 - 0.299731\eta^3. \qquad (3.67)$$

For the initial configuration of all subsequent MC-based investigations [6], we choose structure S_1 obtained in the EA approach for $\eta = 0.65$ and $A = 0.6455$. MC simulations for state points along the line given in Equation 3.67 show that the systems easily adapt to these selected values of η and A by forming the structure predicted in the EA approach. While x assumes a value extremely close to $1/3$ for $\eta \gtrsim 0.4$, it is slightly larger than $1/3$ for $\eta \lesssim 0.4$, indicating that it can adjust properly. Note that the interpolated curve lies slightly above the region where we predict $x = 1/3$ in the ground state around $\eta \approx 0.35$.

Figure 3.29 shows the bond-orientation order parameters Ψ_6, Ψ_8, and Ψ_{10} along the interpolated line. In particular $\Psi_6^{(3)}$ and $\Psi_8^{(2)}$ prove useful in determining the regions of stability of structures H and S_1. In addition, we see a significant increase of $\Psi_6^{(1)}$ and $\Psi_6^{(2)}$ as we approach structure V_x. The region where $\Psi_5 > 0$ coincides with the unclassified region between structures S_1 and V_x (see Figure 3.25).

Figure 3.30 shows a snapshot of structure H. We can see excellent hexagonal order when all particles are projected into a plane. In addition, the honeycomb lattice in layer 1 and the hexagonal lattice in layer 2 are apparent.

Figure 3.31 shows a snapshot of structure S_2. Even though this structure is already rather strongly distorted at zero temperature, a pronounced pattern in layer 2 remains visible.

Figure 3.32 shows a snapshot of structure S_1. The excellent square order in layer 2 is nicely visible.

Figure 3.33 shows a snapshot of structure V_x. Both layers exhibit excellent hexagonal order with very few defects. For the value of η presented here, particles in layer 2 still avoid being on top of particles in layer 1; this implies that the two layers are correlated (see also below). For larger values of η, this correlation decreases and the two layers form independent hexagonal lattices.

We can study the correlation between the two layers more closely by calculating the center-

---

6. Computational details of the MC simulations are given in Subsection 3.3.2.
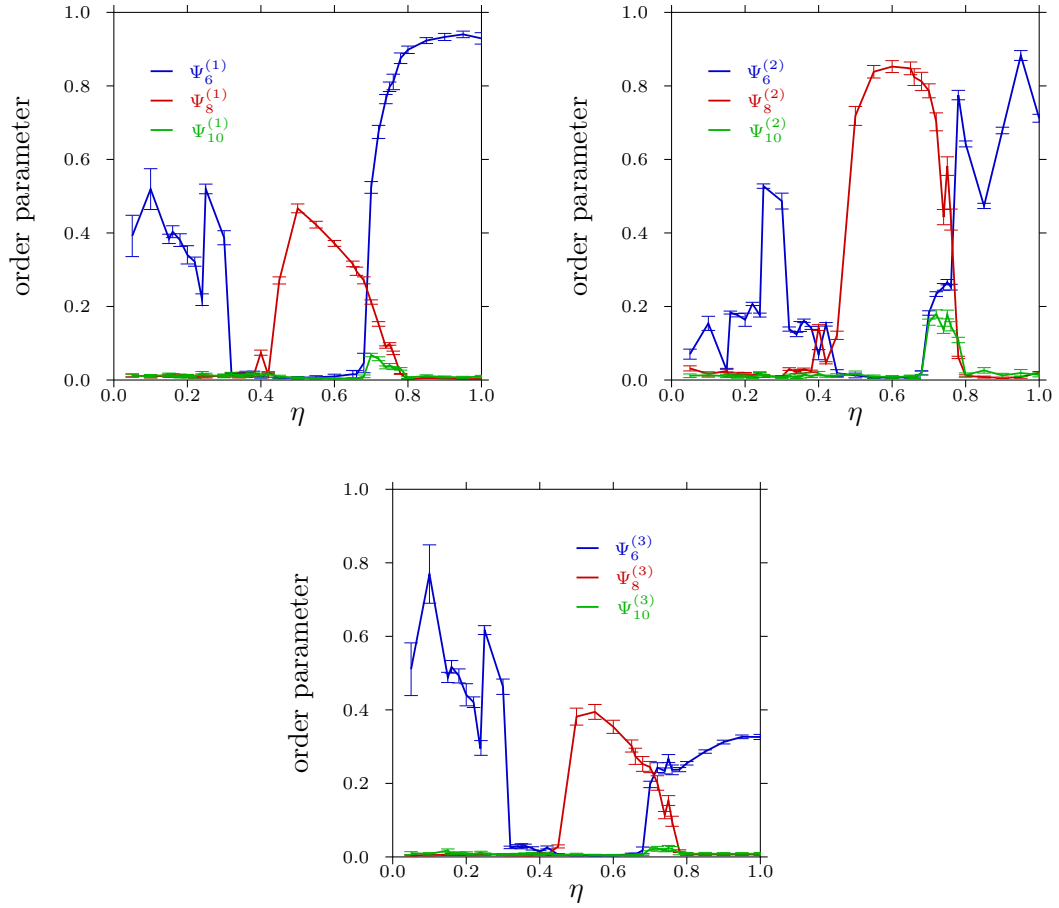
Figure 3.29.: BOOPs of different state points with $x \approx 1/3$ in low-temperature MC simulations. Shown are Ψ_6 (blue), Ψ_8 (red), and Ψ_{10} (green); the latter two parameters can be used to quantify four- and five-fold rotational symmetry, respectively. Top left panel: $\Psi^{(1)}$ for layer 1. Top right panel: $\Psi^{(2)}$ for layer 2. Bottom panel: $\Psi^{(3)}$ when all particles are projected into a plane (see Figure 3.13).
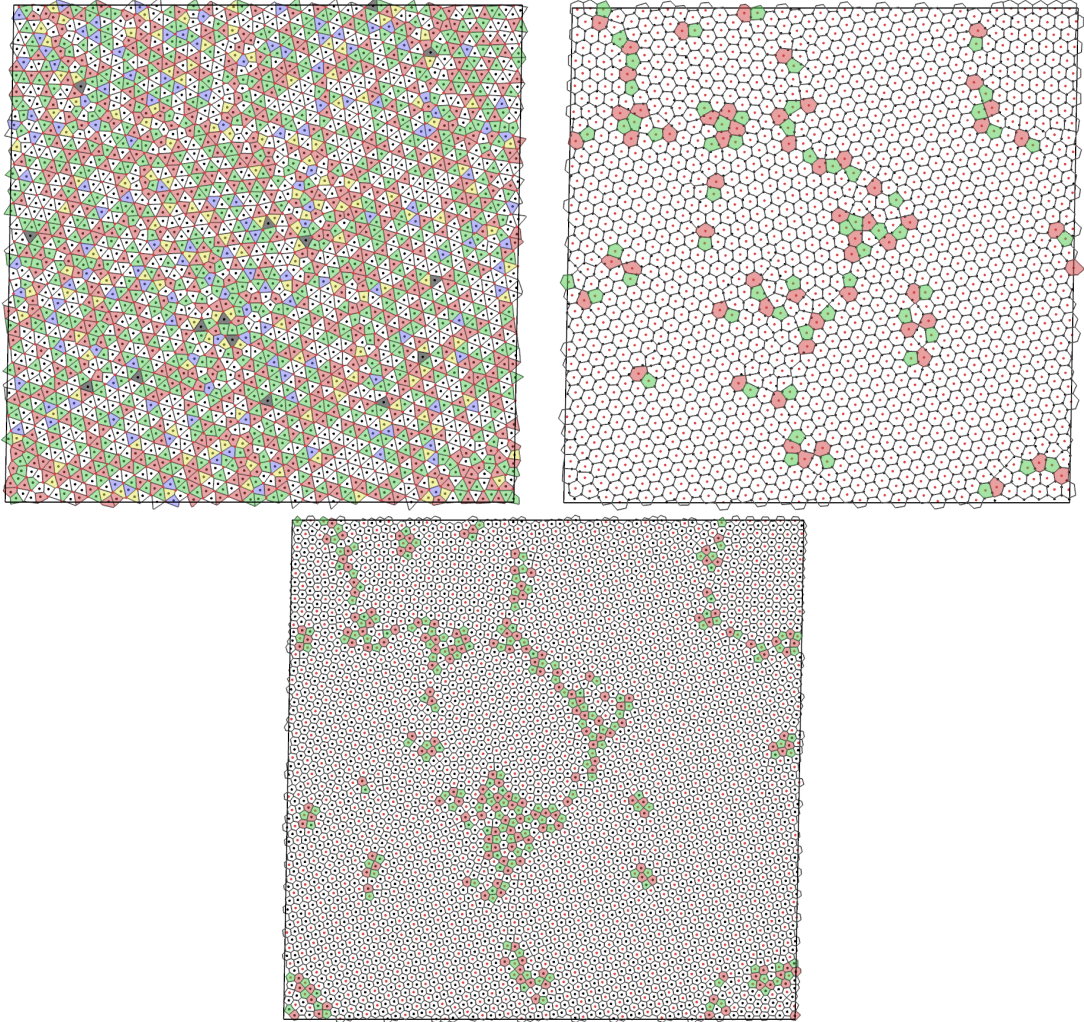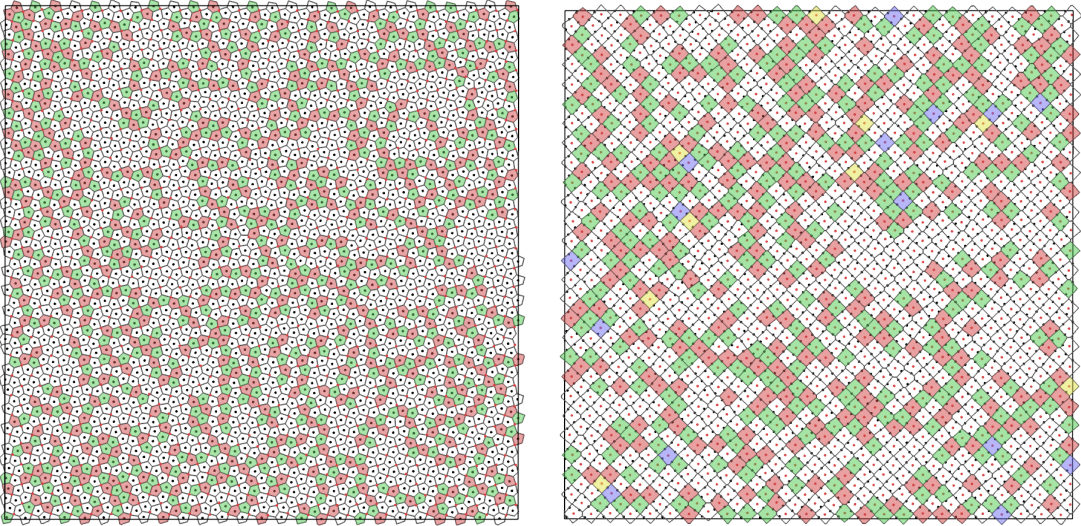
Figure 3.30.: Snapshots of MC simulations for $\eta = 0.30$ and $A = 0.771$ (where we predict structure H). Particles in layers 1 and 2 are colored black and red, respectively. Voronoi polygons are colored according to their number of sides: three sides (black), four (yellow), five (green), six (white), seven (red), eight (blue). Top left panel: Voronoi construction for layer 1. Top right panel: Voronoi construction for layer 2. Bottom panel: Voronoi construction when all particles are projected into a plane. Note the excellent hexagonal order.
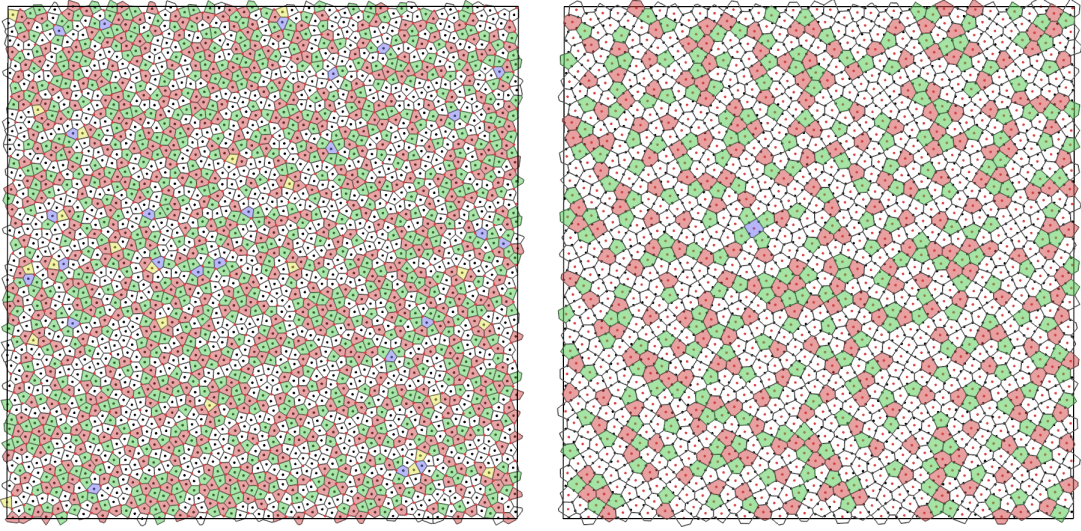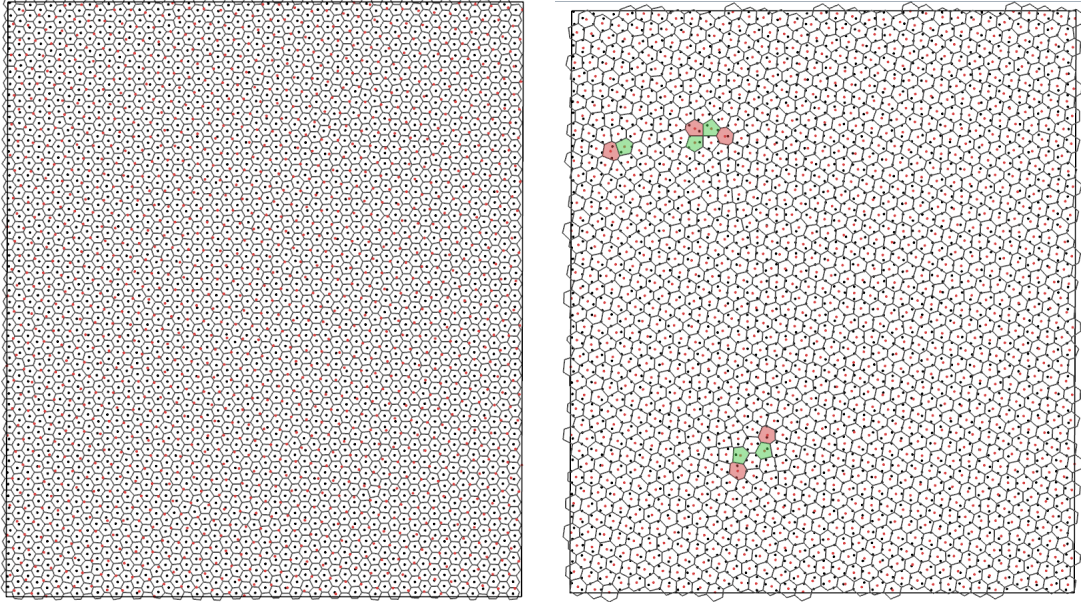
Figure 3.31.: Snapshots of MC simulations for $\eta = 0.45$ and $A = 0.703$ (where we predict structure S_2). Particles in layer 1 and 2 are colored black and red, respectively. Voronoi polygons are colored according to their number of sides: three sides (black), four (yellow), five (green), six (white), seven (red), eight (blue). Left panel: Voronoi construction for layer 1. Right panel: Voronoi construction for layer 2.

Figure 3.32.: Snapshots of MC simulations for $\eta = 0.60$ and $A = 0.657$ (where we predict structure S_1). Particles in layer 1 and 2 are colored black and red, respectively. Voronoi polygons are colored according to their number of sides: three sides (black), four (yellow), five (green), six (white), seven (red), eight (blue). Left panel: Voronoi construction for layer 1. Right panel: Voronoi construction for layer 2. Note the excellent square order.

Figure 3.33.: Snapshots of MC simulations for $\eta = 0.78$ and $A = 0.623$ (where we predict structure V_x). Particles in layer 1 and 2 are colored black and red, respectively. Voronoi polygons are colored according to their number of sides: three sides (black), four (yellow), five (green), six (white), seven (red), eight (blue). Left panel: Voronoi construction for layer 1. Right panel: Voronoi construction for layer 2. Note that both layers exhibit good hexagonal order.

to-center pair correlation functions for different values of η and A

$$g_{11}(r) = \frac{1}{4\pi r \sigma_1 N_1} \left\langle \sum_{i \in L_1} \sum_{i \neq j \in L_1} \delta \left(r - |\boldsymbol{r}_{ij}| \right) \right\rangle \tag{3.68}$$

$$g_{22}(r) = \frac{1}{4\pi r \sigma_2 N_2} \left\langle \sum_{i \in L_2} \sum_{i \neq j \in L_2} \delta \left(r - |\boldsymbol{r}_{ij}| \right) \right\rangle \tag{3.69}$$

$$g_{12}(r) = \frac{1}{2\pi r \sigma_1 N} \left\langle \sum_{i \in L_1} \sum_{j \in L_2} \delta \left(r - |\boldsymbol{r}_{ij}| \right) \right\rangle. \tag{3.70}$$

These are shown in Figure 3.34. We observe that for intermediate values of η, hexagonal order is more strongly pronounced in layer 1; this indicates that the lattice in layer 2 is rather strongly distorted. A distinct structure in $g_{12}(r)$ (see top left panel of Figure 3.34) also indicates that the correlation between the two layers is quite strong. For larger values of η, the peak positions coincide well with a hexagonal lattice in both layers. We further observe a loss of correlation between the layers, evidenced by a flat shape of $g_{12}(r)$ (see bottom left panel of Figure 3.34).

In order to obtain an even better understanding of the structural correlations between the
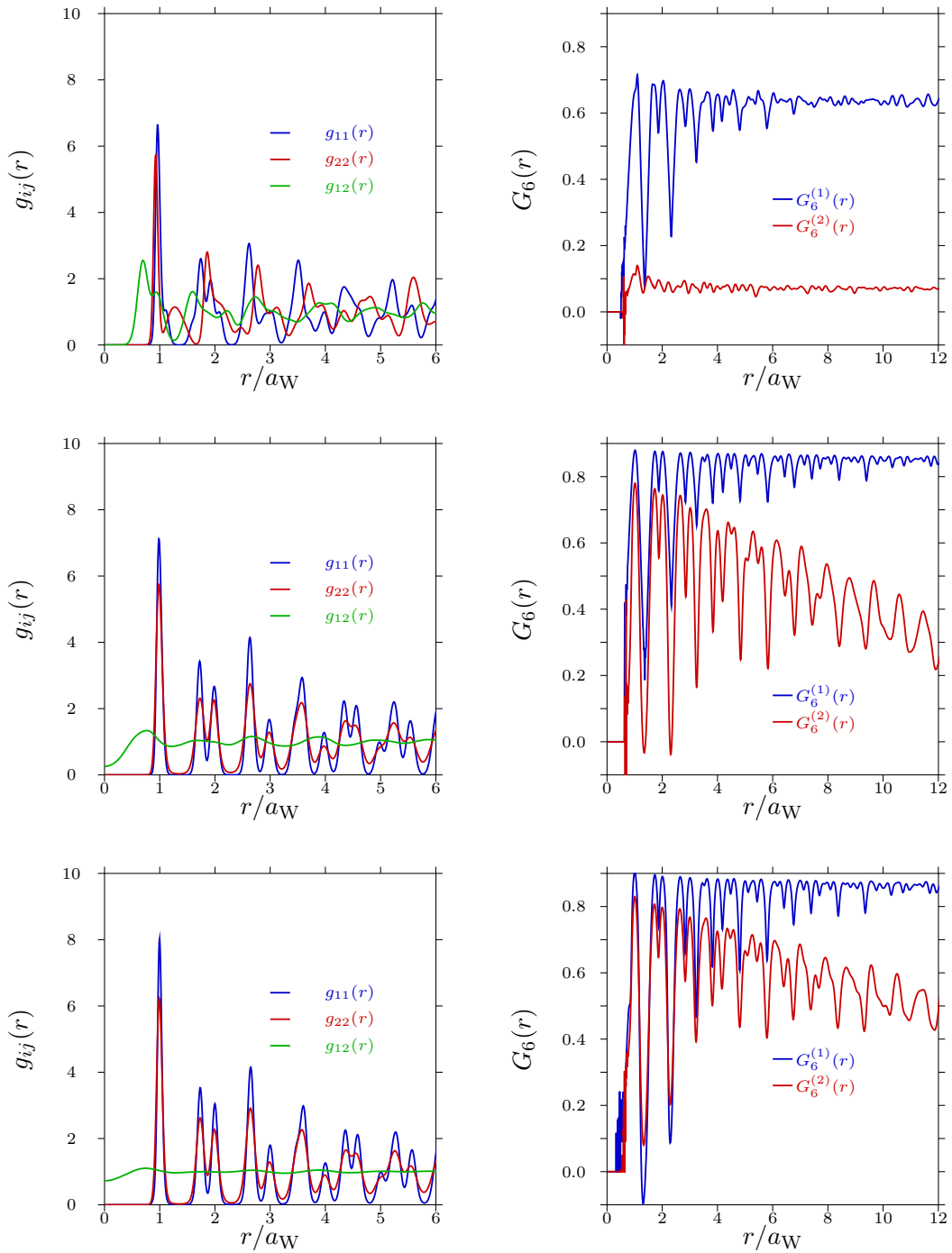
Figure 3.34.: Correlation functions $g_{ij}(r)$ and $G_6(r)$ calculated in the MC simulations. The relevant length scale is given by the Wigner-Seitz radius $a_W = (2/\sqrt{3}\rho)^{1/2}$ of the respective layer or of the total system. **Top row:** results for $\eta = 0.75$ and $A = 0.6274$. Left panel: $g_{ij}(r)$ for the different layers. Right panel: $G_6(r)$ for the two layers. **Center row:** results for $\eta = 0.85$ and $A = 0.6140$. Left panel: $g_{ij}(r)$ for the different layers. Right panel: $G_6(r)$ for the two layers. **Bottom row:** results for $\eta = 1.00$ and $A = 0.5986$. Left panel: $g_{ij}(r)$ for the different layers. Note the weakening of the structural correlations between the two layers in $g_{12}(r)$. Right panel: $G_6(r)$ for the two layers.

layers, it is useful to also calculate the bond-orientational correlation functions

$$G_6^{(1)}(r) = \frac{1}{g_{11}(r)} \left\langle \psi_6^{(1)}(0)\psi_6^{(1)}(r) \right\rangle \qquad (3.71)$$

$$G_6^{(2)}(r) = \frac{1}{g_{22}(r)} \left\langle \psi_6^{(2)}(0)\psi_6^{(2)}(r) \right\rangle . \qquad (3.72)$$

We observe that long-range hexagonal order in layer 1 is indeed present for all three values of η presented in Figure 3.34. For intermediate values of η, we observe a small – yet constant – value of $G_6^{(2)}(r)$ (see top right panel of Figure 3.34). This matches with snapshots (not shown here), which show that particles in layer 2 form a well-ordered rhombic lattice. For larger values of η, we observe that $G_6^{(2)}(r)$ is large for small r, but decays with increasing distance (see bottom right panel of Figure 3.34). We can interpret this as the presence of several large crystallites in layer 2 with slightly different orientation. This indicates that even for $\eta = 1.00$, the lattice in layer 2 still tries to adapt to the lattice in layer 1; this leads to distortions since there is no possible commensurate case of structure V_x with $x = 1/3$ (it is not part of the set N_{in} in Equation 3.21).

We point out that the coupling constant Γ differs for the two layers [175], i.e., $\Gamma_1 \neq \Gamma_2$: if we assume that the layers are uncorrelated, we obtain that for $\rho_1 \approx 2\rho_2$ the coupling constants of the two layers, Γ_1 and Γ_2, are related as $\Gamma_1 \approx \sqrt{2}\Gamma_2$. Though not relevant at the low temperatures studied in this work, this indicates that layer 2 may melt at a lower temperature than layer 1 when the coupling between the two layers is small.

3.3.6. Conclusions and outlook

In summary, we have seen that the introduction of asymmetry to the Wigner bilayer model entails a significant increase in complexity of the observed structures. While we are able to describe the important structural mechanisms for most parts of the phase diagram, a complete classification of *all* observed structures remains elusive. Starting from the known limiting cases – $A \to 0$, $A \to 1$, $\eta \to 0$, and $\eta \to \infty$ – and previously known results, we have identified 14 different structures. Out of these, ten are relatively simple and can be used in the formulation of analytical calculations, which allow for higher precision computations. In particular structures II_x and S_1 were observed with the EA approach and could be adapted for analytical calculations. Both of these configurations exhibit an intricate, non-trivial particle arrangement and are remarkably stable. The remaining four structures identified in the EA approach were too complicated to be included in the analytical approach; these structures show more complicated structural mechanisms with large unit cell sizes. In the entire phase diagram, we have observed a strong competition between two opposing effects: commensurability and effective charge of the layers. While the former plays an important role for two-dimensional lattices and favors a discrete set of x-values, the latter is related to the influence of the plate separation η and the background asymmetry A on the charge

density distribution x.

A publication containing the results presented in this section is currently in preparation [173].

For future work, a closer investigation of the remaining unclassified regions would be interesting. This could on the one hand be done by performing additional computations with increased systems sizes. On the other hand, it might be possible to identify the underlying mechanisms using different ΨRGB-phase diagrams or other order parameters. In addition, finding a relatively simple parametrization of the more complicated structures and including them in the analytical approach may help improve accuracy.

3.4. Ellipsoidal particles with embedded linear quadrupole moment confined to a plane

3.4.1. Introduction

As we have seen in Section 3.1, even a simple equimolar binary mixture can exhibit remarkably complex behavior. Similarly, a simple modification to a system's confining geometry (in this case a bilayer) can produce a multitude of interesting and non-trivial structures (see Section 3.3).

In this section, we introduce and adapt another feature in the properties of the particles which also can lead to an unexpectedly large variety of self-assembly scenarios, namely anisotropy. We introduce this feature by naturally extending the electrostatic interaction, studied in Sections 3.1, 3.2, and 3.3, towards higher-order multipoles [62].

Multipoles are often used to model complicated charge distributions in complex particles, such as organic molecules [176]: in organic chemistry, molecules often exhibit complicated shapes [177, 178] and can moreover be deformable [179, 180]. In this section, we put forward a simple model for such organic molecules which captures both an aspheric shape as well as a complicated charge distribution. We study soft ellipsoidal particles with an embedded linear quadrupole moment in two dimensions.

3.4.2. Model and approach

Carbon chains are a very common element in organic molecules. Due to the large number of possible bonds that carbon can form with variety of other atoms, organic molecules can form highly intricate structures and shapes [178]. The presence of hydrogen or atoms other than carbon, as well as the geometry of the molecule and the kind of bonds between its constituent atoms can influence the distribution of partial charges within a molecule [181].

In electrostatics, any charge distribution can be developed into a multipole expansion [62], splitting the complicated charge distribution into a point net charge, a point net dipole moment, a point net quadrupole moment, etc.

The top left panel of Figure 3.35 shows an example of a simple organic molecule, the type of which we want to model. We approximate the rough shape of the elongated molecule with an ellipsoid (see top right panel of Figure 3.35). For simplicity, we further assume that the molecule carries neither a net charge, nor a net dipole moment. The lowest-order remaining electrostatic interaction is thus quadrupolar. In order to further simplify the problem, we only consider *linear* quadrupole moments, such that the quadrupole tensor can be written as

$$\hat{Q} = \begin{pmatrix} Q_{xx} & 0 & 0 \\ 0 & Q_{yy} & 0 \\ 0 & 0 & -Q_{xx} - Q_{yy} \end{pmatrix} \tag{3.73}$$

$$= Q \begin{pmatrix} 1/2 & 0 & 0 \\ 0 & 1/2 & 0 \\ 0 & 0 & -1 \end{pmatrix}. \tag{3.74}$$

We study the system in two dimensions, such that the interaction between linear quadrupole moments can be written as

$$V_{\text{qp}}(\boldsymbol{r}_{ij}, \hat{\boldsymbol{u}}_i, \hat{\boldsymbol{u}}_j) = \frac{3}{4} \frac{Q^2}{r_{ij}^5} \left[1 - 5a^2 - 5b^2 - 15a^2b^2 + 2 \left(c - 5ab \right)^2 \right], \tag{3.75}$$

where we use

$$a = \hat{\boldsymbol{u}}_i \cdot \hat{\boldsymbol{r}}_{ij} \tag{3.76}$$

$$b = \hat{\boldsymbol{u}}_j \cdot \hat{\boldsymbol{r}}_{ij} \tag{3.77}$$

$$c = \hat{\boldsymbol{u}}_i \cdot \hat{\boldsymbol{u}}_j. \tag{3.78}$$

Here, the vector $\boldsymbol{r}_{ij} = \boldsymbol{r}_i - \boldsymbol{r}_j$ denotes the distance between particles i and j and $\hat{\boldsymbol{r}}_{ij}$ its direction. The particle orientation $\hat{\boldsymbol{u}}_i$ of particle i indicates the direction of the linear quadrupole moment, which we assume to be identical with one of the two axes of the ellipse and to lie in the xy-plane. While the interaction (see Equation 3.75) decays rather slowly $\sim 1/r^5$, we can still calculate the corresponding lattice sums with sufficient accuracy with real space summations. In contrast to two dipoles, which tend to line up head-to-tail, two linear quadrupoles prefer the so-called T-configuration (see Figure 3.36).

In order to model the ellipsoidal shape of the particles, we employ a simple short-ranged repulsive potential whose dependence on the particle orientations is inspired by the Gay-
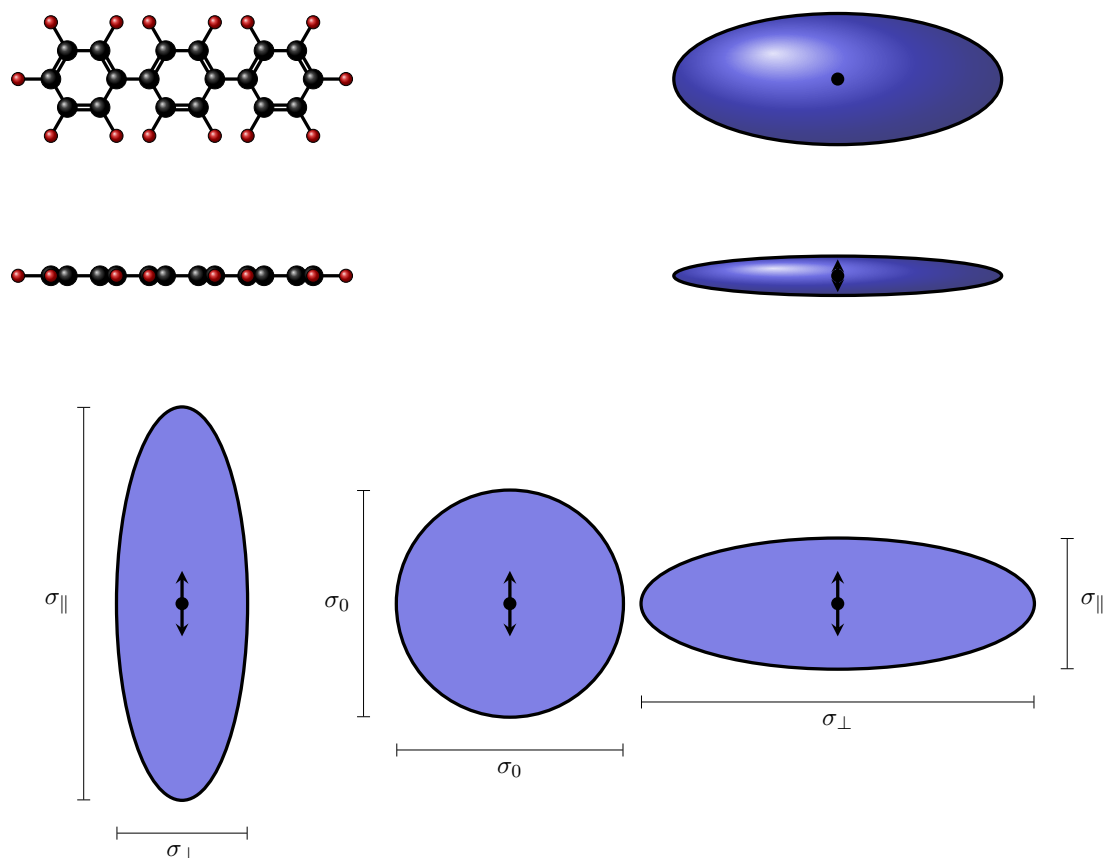
Figure 3.35.: **Top row:** left panel: example of a simple organic molecule composed of several benzene rings. Molecules of this type are distinctly aspheric and feature a complicated charge distribution. Right panel: we model simple organic molecules as soft ellipsoidal particles (with aspect ratio κ) with an embedded quadrupole moment. Due to the high degree of symmetry, the quadrupole moment in this example is linear. **Bottom row:** soft ellipsoidal particles with axes parallel and perpendicular – $\sigma_\parallel$ and $\sigma_\perp$, respectively – to the embedded linear quadrupole moment. Left panel: $\kappa = \sigma_\parallel/\sigma_\perp > 1$. Center panel: soft disk ($\kappa = 1$) with embedded linear quadrupole moment. Right panel: $\kappa < 1$.
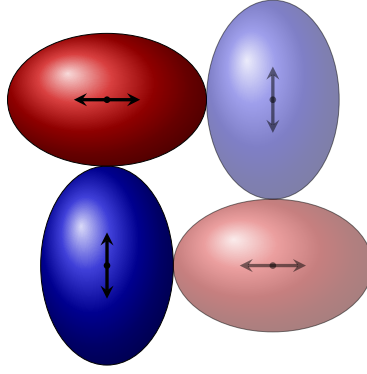
Figure 3.36.: Schematic view of the typical T-configuration in quadrupolar systems. In isolated clusters, neighboring particles assume orthogonal orientations with respect to each other. This two-particle configuration can be repeated to form a square particle arrangement.

Berne potential [182]

$$V_{\text{ell}}(\boldsymbol{r}_{ij}, \hat{\boldsymbol{u}}_i, \hat{\boldsymbol{u}}_j) \quad = \quad 4\epsilon(\boldsymbol{r}_{ij}, \hat{\boldsymbol{u}}_i, \hat{\boldsymbol{u}}_j) \left[\frac{\sigma(\boldsymbol{r}_{ij}, \hat{\boldsymbol{u}}_i, \hat{\boldsymbol{u}}_j)}{r_{ij}} \right]^n, \tag{3.79}$$

where

$$\epsilon(\boldsymbol{r}_{ij}, \hat{\boldsymbol{u}}_i, \hat{\boldsymbol{u}}_j) \quad = \quad \epsilon_0 = \text{const.} \tag{3.80}$$

$$\chi \quad = \quad \frac{\kappa^2 - 1}{\kappa^2 + 1} \tag{3.81}$$

$$\sigma(\boldsymbol{r}_{ij}, \hat{\boldsymbol{u}}_i, \hat{\boldsymbol{u}}_j) \quad = \quad \sigma_0 \left\{ 1 - \frac{\chi}{2} \left[\frac{(a+b)^2}{1 + \chi c} + \frac{(a-b)^2}{1 - \chi c} \right] \right\}^{-1/2}. \tag{3.82}$$

Throughout, we have set $n = 18$. We define the basic length scale σ_0 as the diameter of a soft disk ($\kappa = 1$), such that the area occupied by each ellipse is the same for any value of κ

$$\frac{\pi}{4}\sigma_\parallel \sigma_\perp \quad = \quad \frac{\pi}{4} \left(\sqrt{\kappa}\sigma_0 \right) \left(\sqrt{\frac{1}{\kappa}}\sigma_0 \right) \tag{3.83}$$

$$= \quad \frac{\pi}{4}\sigma_0^2 = \text{const.} \tag{3.84}$$

While the shape of the ellipse is the same for $\kappa \leftrightarrow 1/\kappa$, the orientation of the embedded quadrupole moment is not (see bottom panels of Figure 3.35). Investigating values of κ both smaller and larger than unity thus allows us to study both cases within the same model.

We perform calculations under NPT-conditions, where the relevant thermodynamic potential for vanishing temperature is the enthalpy per particle

$$\frac{H}{N} \quad = \quad \frac{E}{N} + P\frac{S_0}{N}. \tag{3.85}$$

We use reduced units throughout by defining the scales for length, σ_0, and energy, ϵ_0: the resulting reduced quadrupole moment $(Q^*)^2 = Q^2/4\pi\epsilon_{\mathrm{pm}}\sigma_0^5\epsilon_0$ (where $\epsilon_{\mathrm{pm}} = 1$ is the relative permittivity) and reduced pressure $P^* = P\sigma_0/\epsilon_0$ define – together with the aspect ratio $\kappa = \sigma_\parallel/\sigma_\perp$ – the phase diagram.

First we will treat the problem at zero temperature in order to identify the ground state structures and the basic strategies for self-assembly under specified external conditions. We employ our EA tool to investigate the ground state structures over a range of κ for several different combinations of $(Q^*)^2$ and P^*. Due to the large computational effort – necessitated by the variable density and the additional degrees of freedom of the particle orientations – we restrict ourselves to cells containing up to twelve particles.

Then, in order to determine their thermodynamic stability, we use the obtained structures as input for subsequent Molecular Dynamics (MD) simulations performed by Thomas Heinemann. The obtained results provide further insight into the melting behavior of the system.

3.4.3. Theory and order parameters

In order to quantify the positional order of a configuration, we again use two-dimensional BOOPs (see Section 2.4), in particular the four-fold Ψ_4 and and six-fold Ψ_6 parameters. Since the interaction is anisotropic, it is also useful to quantify the orientational order.

One possible way of doing this is via the tensor order parameter

$$\hat{T} = 2\frac{1}{N}\sum_{i=1}^{N}\hat{\boldsymbol{u}}_i \otimes \hat{\boldsymbol{u}}_i - \mathbb{1} \tag{3.86}$$

$$= \begin{pmatrix} T_{xx} & T_{xy} & T_{xz} \\ T_{yx} & T_{yy} & T_{yz} \\ T_{zx} & T_{zy} & T_{zz} \end{pmatrix}. \tag{3.87}$$

The more commonly used nematic order parameter S is defined as the largest eigenvalue of $\hat{T}$; its equivalent is a trivial problem in two dimensions (if – as we assume – $\hat{\boldsymbol{u}}_i$ is in-plane) since the tensor is traceless and $T_{xy} = T_{yx}$:

$$\hat{T} = \begin{pmatrix} T_{xx} & T_{xy} \\ T_{xy} & T_{yy} \end{pmatrix} \tag{3.88}$$

$$S = \sqrt{T_{xx}^2 + T_{xy}^2}. \tag{3.89}$$

The eigenvector associated with S is called the director $\hat{\boldsymbol{d}}$ and indicates a preferred orientation in the configuration. Note that S is always positive, except when all elements of $\hat{T}$ are zero; this occurs when no preferred direction is present in the system.

We can also quantify the orientational order using Voronoi construction and the alignment

of nearest neighbors

$$\beta = \frac{1}{N}\sum_{i=1}^{N}\frac{1}{\sum_{j\in\mathcal{N}_i}l_{ij}}\sum_{j\in\mathcal{N}_i}l_{ij}\left|\hat{\boldsymbol{u}}_i\cdot\hat{\boldsymbol{u}}_j\right|, \tag{3.90}$$

where we again use the modification with the side length of the Voronoi polygons (see Subsection 2.4.5). In addition, we can also define order parameters combining positional and orientational order [183, 184]

$$\alpha = \frac{1}{2N}\sum_{i=1}^{N}\frac{1}{\sum_{j\in\mathcal{N}_i}l_{ij}}\sum_{j\in\mathcal{N}_i}l_{ij}\left|(\hat{\boldsymbol{u}}_i\cdot\hat{\boldsymbol{r}}_{ij})^2+(\hat{\boldsymbol{u}}_j\cdot\hat{\boldsymbol{r}}_{ij})^2\right|. \tag{3.91}$$

Since the phase of the system is determined by three independent parameters – κ, $(Q^*)^2$, and P^* – it might be advantageous to investigate possible scaling relations between these quantities. For simplicity, we assume that the short-range interaction is hard (thus $E_{\mathrm{ell}}=0$ for allowed configurations). The remaining two contributions to the enthalpy

$$H = E_{\mathrm{qp}}+PS_0, \tag{3.92}$$

thus scale as

$$E_{\mathrm{qp}} \sim (Q^*)^2 \tag{3.93}$$
$$PS_0 \sim P^*. \tag{3.94}$$

Therefore, as long as the ratio $(Q^*)^2/P^*$ is kept constant, we expect similar structures for a given value of κ. However, we emphasize that this scaling relations is only valid in the limit of very hard particles, i.e., for very large values of n in Equation 3.79.

3.4.4. Results

In the following, we focus on results obtained for $(Q^*)^2=1$ and $P^*=1$, varying κ over an evenly spaced grid of 210 points in the range $[0.4, 2.5]$, since this set of parameters exhibits most of the interesting features of the system. In addition, we discuss some other special cases. We start with a general discussion of the different order parameters as κ varies before elaborating on the different observed structures.

Phase diagrams

The short-range potential remains unchanged upon inversion of the two axes $\kappa \leftrightarrow 1/\kappa$. This is, however, not true for the quadrupolar interaction, resulting in a different shape of both enthalpy per particle $H^*(\kappa)/N$ and order parameters (see top panel of Figure 3.37). For
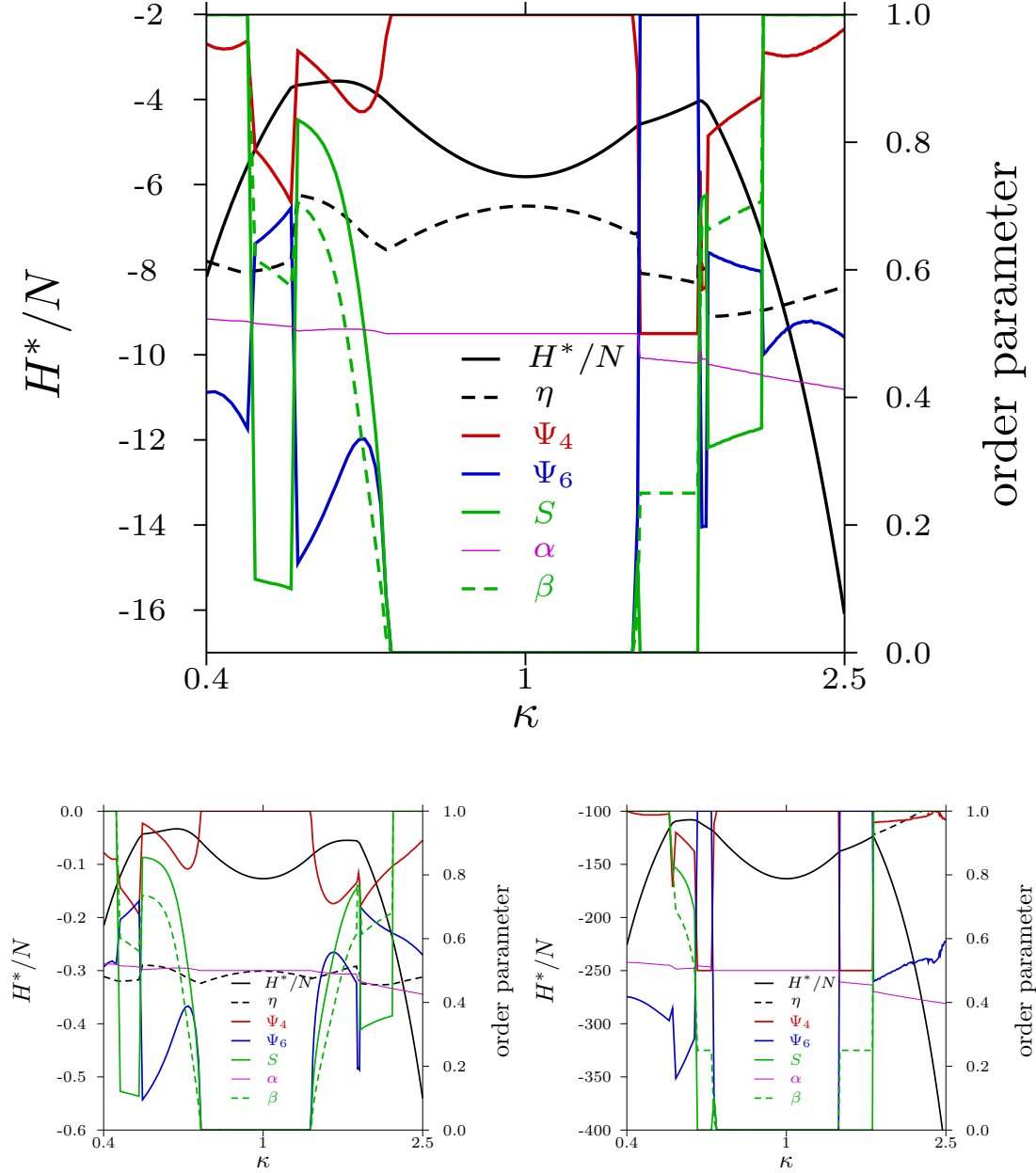
Figure 3.37.: Reduced enthalpy and order parameters of the observed structures as functions of κ (logarithmic axis). Top panel: $(Q^*)^2 = 1$ and $P^* = 1$. **Bottom row:** left panel: $(Q^*)^2 = 0.1$ and $P^* = 0.1$. Right panel: $(Q^*)^2 = 10$ and $P^* = 10$. Note that η is larger than unity for most values of κ in this case.

$(Q^*)^2 = 1$ and $P^* = 1$, the enthalpy curve shows a pronounced local minimum around $\kappa \approx 1$ (where the T-configuration is dominant) and diverges for $\kappa \to 0$ and $\kappa \to \infty$ (where the formation of parallel rows is favorable). The local maxima occurring between these regions signal the formation of more complicated structures, which is also reflected in the different order parameters. The nematic order parameter S shows that for κ far from unity, a single orientation prevails (thus $S = 1$); whereas we observe $S = 0$ for $\kappa \approx 1$, indicating the absence of a preferred direction. If we contrast S with the similar order parameter β, we see that there are actually two distinct regions with $S = 0$ and that the angles between the orientations of nearest neighbors is $\pi/2$ and $\pi/3$, respectively.

In order to check our scaling relation for hard quadrupolar ellipsoids (see Equations 3.93 and 3.94), we can compare results for several points with the same ratio $(Q^*)^2/P^*$. The two bottom panels of Figure 3.37 show the phase diagrams for $(Q^*)^2 = 0.1$, $P^* = 0.1$ and $(Q^*)^2 = 10$, $P^* = 10$. We can immediately see that the general shape of the order parameters and the enthalpy as functions of κ is partly similar, in particular for smaller values of $(Q^*)^2$ and P^*. However, results differ significantly in some regions, i.e., some structures are not observed at all. We thus conclude that even for the exponent $n = 18$ used in this work for the short-range repulsion, the behavior of the ellipsoidal particles is still remarkably different from the hard limit.

Structures with one orientation

For κ-values far from unity, i.e., in case of strong anisotropy, the ellipsoids tend to align in a parallel fashion. They accomplish this by forming tilted rows with high density, denoted the *parallel displaced*-configuration (PD-configuration, see top and bottom right panels of Figure 3.38). Since the head-to-tail arrangement is unfavorable for quadrupoles, neighboring rows repel each other, leading to large gaps between these lanes. The parallel offset between rows can be very sensitive to changing κ, leading to a slight modulation of BOOPs. An interesting special case occurs for vanishing quadrupole moment $(Q^*)^2 = 0$, where we observe a distorted hexagonal lattice, denoted the *parallel*-configuration (P-configuration, see left panel of Figure 3.38).

Structures with two orientations

For κ close to unity, particles prefer orthogonal orientation with respect to their nearest neighbors. For large $(Q^*)^2$ and small P^*, a perfectly orthogonal particle orientations with an underlying square pattern can be realized, denoted the *square T*-configuration (T_{sq}-configuration, see top left panel of Figure 3.39). However, another similar arrangement – this time with an underlying hexagonal pattern – is possible, denoted the *hexagonal T*-configuration (T_{hex}-configuration, see bottom left panel of Figure 3.39). Note that in this configuration perfect orthogonal orientation of nearest neighbors is, however, only realized
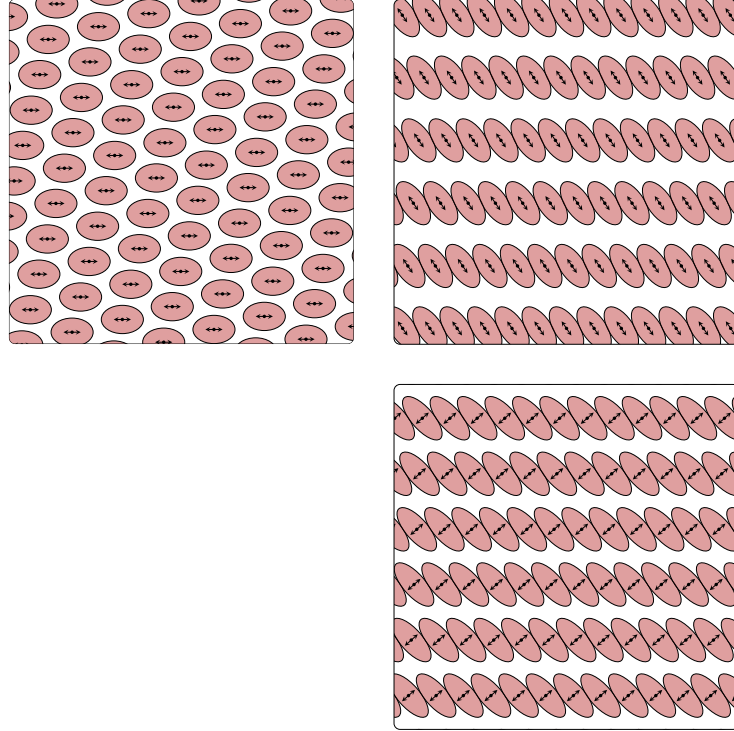
Figure 3.38.: Snapshots of configurations with one preferred orientation. Left panel: P-configuration for $(Q^*)^2 = 0$, $P^* = 1$, $\kappa = 1.5$. Top right panel: PD-configuration for $(Q^*)^2 = 1$, $P^* = 1$, $\kappa = 2.1$. Bottom right panel: PD-configuration for $(Q^*)^2 = 1$, $P^* = 1$, $\kappa = 0.4$.
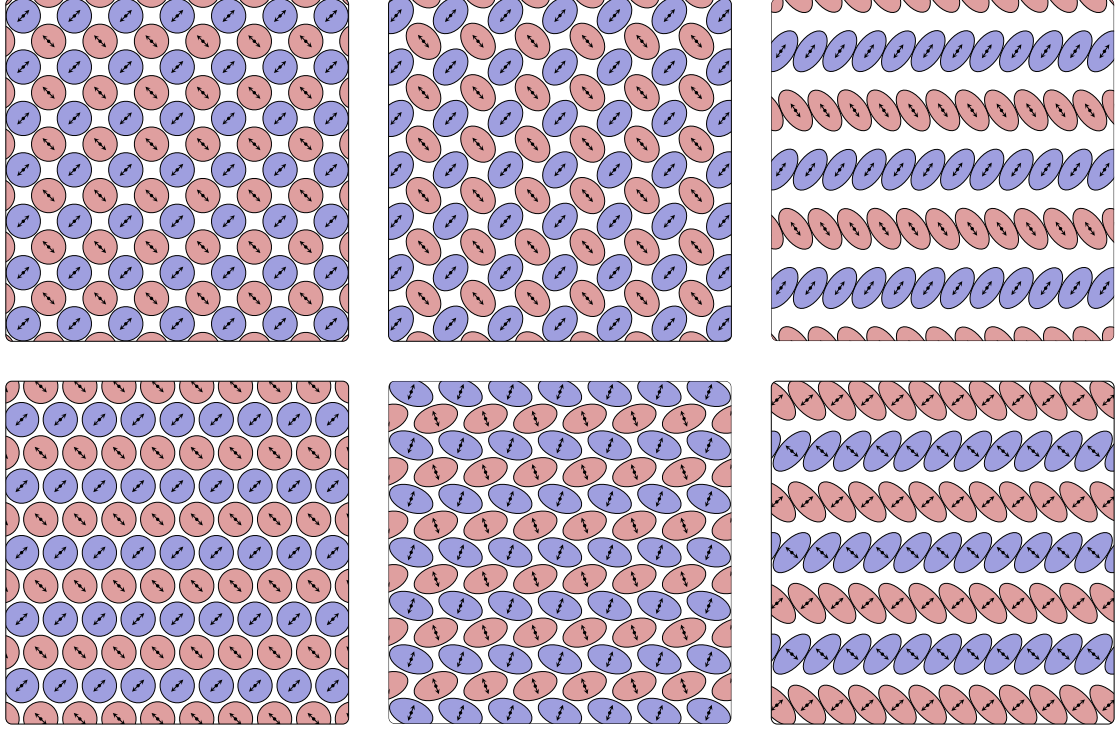
Figure 3.39.: Snapshots of configurations with two preferred orientations. Different colors indicate different orientations. **Left column:** top panel: T_{sq}-configuration for $(Q^*)^2 = 1$, $P^* = 1$, $\kappa = 1$. Bottom panel: T_{hex}-configuration for $(Q^*)^2 = 0.1$, $P^* = 10$, $\kappa = 1$. **Center column:** top panel: HB_{dense}-configuration for $(Q^*)^2 = 1$, $P^* = 1$, $\kappa = 1.38$. Bottom panel: HB_{dense}-configuration for $(Q^*)^2 = 1$, $P^* = 1$, $\kappa = 0.58$. **Right column:** top panel: HB_{loose}-configuration for $(Q^*)^2 = 1$, $P^* = 1$, $\kappa = 1.83$. Bottom panel: HB_{loose}-configuration for $(Q^*)^2 = 1$, $P^* = 1$, $\kappa = 0.48$.

for $\kappa = 1$.

The two T-configurations discussed above are special cases of the more general *herringbone*-configuration (HB-configuration). Here, the relative orientation between neighboring particles changes with κ. Interestingly, the shape of β indicates a first order transition *within* the HB-configuration (see top panel of Figure 3.37), i.e., at some point the relative orientation of neighboring particles is discontinuous. A closer investigation of the associated particle configurations reveals the existence of two different versions of the HB-configuration:

- For κ somewhat closer to unity, we observe a dense structure, which we denote HB$_{\text{dense}}$ (see top and bottom center panels of Figure 3.39).
- For κ slightly further away from unity, we observe the formation of rows of alternating orientation (see top and bottom right panels of Figure 3.39). Since neighboring rows repel each other, this structure has a lower density; we thus denote it HB$_{\text{loose}}$.
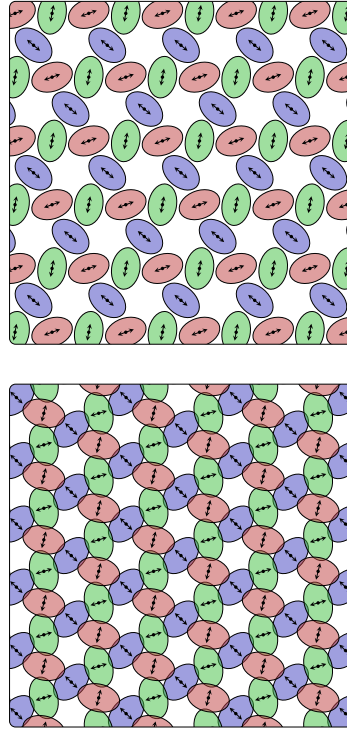
Structures with three orientations

Figure 3.40.: Snapshots of configurations with three preferred orientations. Different colors indicate different orientations. Top panel: TH-configuration for $(Q^*)^2 = 1$, $P^* = 1$, $\kappa = 1.5$. Bottom panel: TH-configuration for $(Q^*)^2 = 10$, $P^* = 1$, $\kappa = 0.65$.

A very interesting phenomenon is the occurrence of a structure with three preferred orientations. Similar to the T-configurations, we cannot define a preferred direction in this case, resulting in a nematic order parameter $S = 0$. The particle arrangement here is reminiscent

of a *trihexagonal* tiling, consisting of hexagons and triangles; we thus denote it the TH-configuration (see Figure 3.40). The relative orientation between neighboring particles of $\pi/3$ is reflected in the order parameter $\beta = \cos^2(\pi/3) = 1/4$ (see top panel of Figure 3.37). Note that the stability of the TH-configuration strongly depends on the choice of $(Q^*)^2$ and P^*, whereas some variant of the HB-configuration can almost always be observed for some range of κ.

More complicated structures
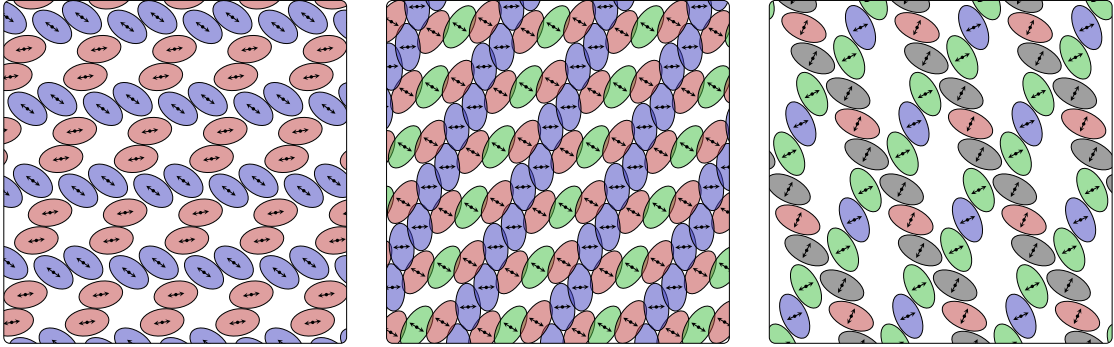
Figure 3.41.: Snapshots of more complicated configurations. Different colors indicate different orientations. Left panel: B-configuration for $(Q^*)^2 = 1$, $P^* = 1$, $\kappa = 1.66$. Center panel: B-configuration for $(Q^*)^2 = 10$, $P^* = 10$, $\kappa = 0.52$. Right panel: B-configuration for $(Q^*)^2 = 1$, $P^* = 0.1$, $\kappa = 0.53$.

For some small ranges of κ, we also observe more complicated structures not conforming to the structural mechanisms described above. These structures require a larger number of particles per cell. While we observe several different variants of such structures, they share a common mesh-like lattice, where chains of particles undulate back and forth (see Figure 3.41). We denote these *branched* structures (B-configuration). The similarity of B-configurations to what we would expect at finite temperature, i.e., the undulation of previously straight lines, indicates that they may actually represent metastable structures. Since they can also be interpreted as a hybrid between the two different HB-configurations, it is also possible that the system phase separates.

Stability and melting of observed structures

MD simulations performed by Thomas Heinemann [185] reveal that the structures observed at zero temperature remain stable at low temperature ($T^* = k_\mathrm{B}T/\epsilon_0 = 0.1$, see second column of Figure 3.42). With increasing temperature, more and more defects start to form (see third column of Figure 3.42). The most common of these is a slight wave-like modulation of previously straight lines. Finally, crystalline order is rapidly lost once the temperature is raised above a certain threshold value (see fourth column of Figure 3.42); the related
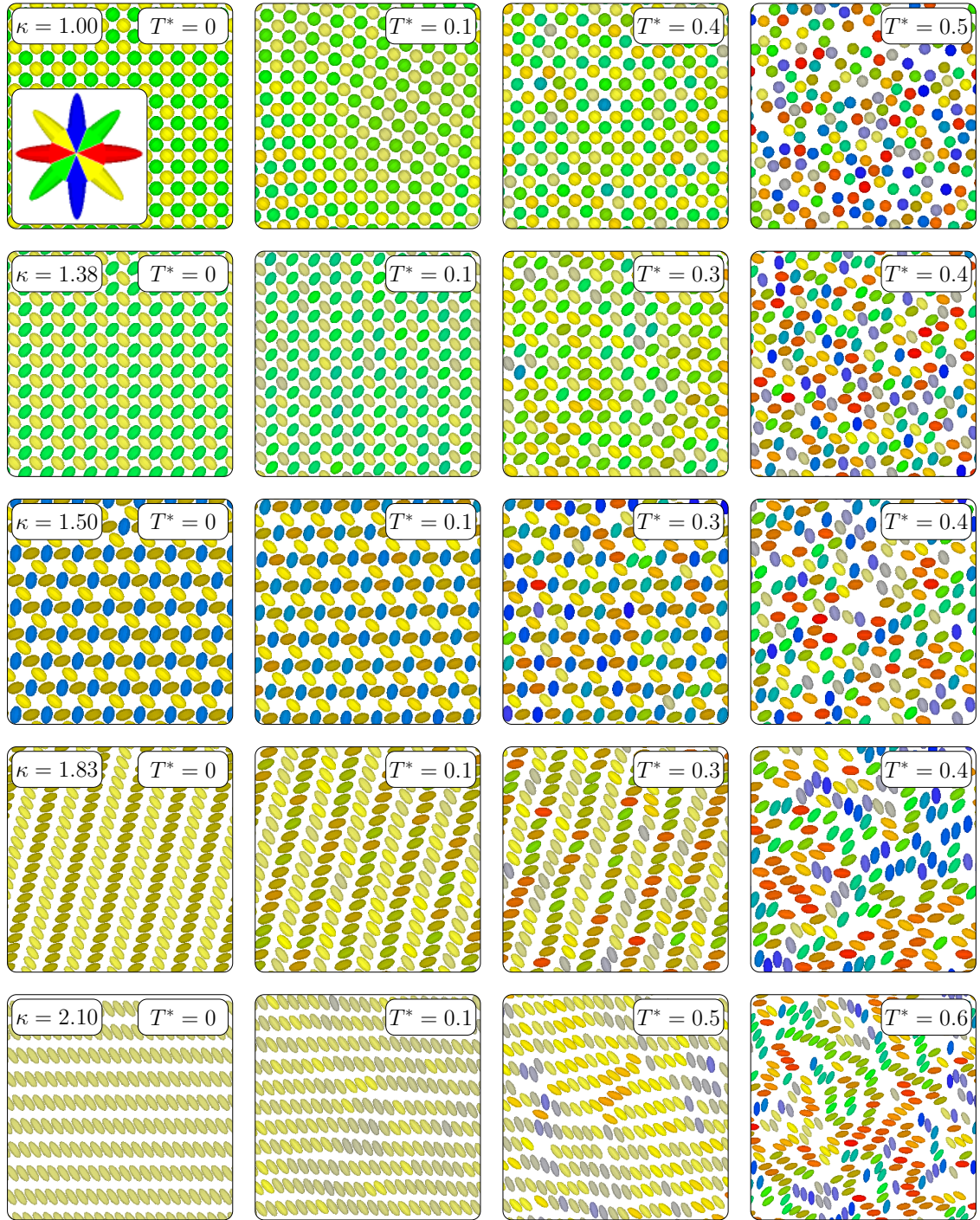
Figure 3.42.: Snapshots of MD simulations (courtesy of Thomas Heinemann [185]) for different values of $\kappa = \sigma_\parallel / \sigma_\perp$ (as labeled) and $T^* = k_B T / \epsilon_0$ (as labeled). Different colors indicate different particle orientations (see inset in the top left panel). **First row:** $\kappa = 1$ (T_{sq}-configuration). **Second row:** $\kappa = 1.38$ (HB$_{dense}$-configuration). **Third row:** $\kappa = 1.5$ (TH-configuration). **Fourth row:** $\kappa = 1.83$ (HB$_{loose}$-configuration). **Fifth row:** $\kappa = 2.1$ (PD-configuration).

temperature depends strongly on κ. Configurations with $\kappa \approx 1$ (T_{sq}-configuration) and κ far from unity (PD-configuration) are the most stable ones (losing order for $T^* = 0.5$ and $T^* = 0.6$, respectively), while the complicated B-configurations (not shown) melt very quickly or transform into other configurations (as low as $T^* = 0.2$).

Obtaining the observed ground state configurations via simulated annealing is only successful for very few parameter points. In general, it is marred by frustration effects, especially for κ far from unity, where particles have difficulties rotating.

3.4.5. Conclusions and outlook

In summary, we have derived a simple model for elongated organic molecules without a net charge or dipole moment: this model consists of soft ellipsoids with an embedded linear quadrupole moment. The preferred orthogonal arrangement of linear quadrupole moments in close proximity to each other leads to an interesting contrast compared to dipolar systems, where particles prefer parallel arrangement, thus often forming chains. In addition, the system is characterized by a competition between the shape anisotropy of the ellipsoids and the quadrupolar interaction. We have investigated the system for several different parameter points in the $[(Q^*)^2, P^*]$-plane and observed several different mechanisms depending on the shape anisotropy κ. While we always observed configurations of parallel rows for κ far from unity, the sequence of structures between these two limiting cases strongly depends on the competition between the short- and long-range interactions. We observe two different configurations with orthogonal particle arrangement for $\kappa \approx 1$, one based on a square lattice, the other on a hexagonal lattice. Intermediate ranges of κ – both for $\kappa > 1$ and $\kappa < 1$ – are mostly dominated by two variations of the herringbone configuration. In addition, we sometimes observe an interesting, non-trivial lattice based on the trihexagonal tiling. In very small ranges of κ, more complicated branched structures can emerge. However, these are generally very unstable at finite temperature as shown in complementary MD simulations, indicating metastability at vanishing temperature.

A publication containing the results presented in this section is currently in preparation [185].

For future work, it would be useful to extend our simple model to general quadrupole moments and slab (or even fully three-dimensional) geometries. This would nicely tie in with the huge experimental interest in the self-assembly of complex organic molecules on surfaces [177, 181]. Some of these systems show a remarkable variety of different structures, which can even be controlled via external parameters, which opens up many interesting technological applications [186, 187]. The understanding of our simple model could serve as a starting point for the investigation of the more complex molecules used in these studies. Extending the model step-by-step towards more complicated shapes and effective interactions would help with the many competing effects [180, 188].

A closely related system are inverse patchy colloids (IPCs): colloids decorated with charged patches, leading to a charge distribution close to a linear quadrupole moment. IPCs have been observed to form similar structures in both simulations [189] and experiments [190].

4. Conclusions

In this thesis, we have investigated the ordered equilibrium structures of several simple long-ranged systems. Each of these systems was characterized by some property that induced a sufficient degree of complexity for interesting phenomena to be observed.

Our approach consisted in first determining a system's ground state configuration using an optimization tool based on evolutionary algorithms (EAs). We then used the obtained results as starting points for investigations of their mechanical and thermodynamic stability using either Monte Carlo (MC) or Molecular Dynamics (MD) simulations at low temperatures. In order to quantify and classify the observed structures, we defined suitable order parameters.

The first system was based on classical point charges confined to a planar geometry, a well established system known as the Wigner monolayer. Its ground state is given by a simple hexagonal (equilateral triangular) lattice. Comparing our results to data available in the literature, we could verify the accuracy of our energy calculations based on Ewald summation and found excellent agreement. We then increased the complexity of the system by extending it to an equimolar binary mixture of charges confined to a planar geometry. The consideration of a simple phase separation scenario – based on complete de-mixing of the two components – allowed us to analytically calculate a reference energy to put our results in relation with. Considering the entire interesting range of ratios between the two charges, we observed six non-trivial ordered ground state configurations and a range where our phase separation scenario was favorable; the relevant energy differences between competing structures were three orders of magnitude smaller than the total energy of the system. A simple structure based on two intertwining square lattices was found to be remarkably stable. For future work, introducing the molar fraction as an additional parameter, i.e., investigating non-equimolar binary mixtures, may be of interest. Not only would this substantially increase the number of possible structures, but it would also allow more complicated phase separation scenarios with two phases: one being rich in the first charge species, the other in the second.

The second system was based on a different way of introducing complexity to the Wigner monolayer: this time by vertically displacing a single charge. The two limiting cases for vanishing and infinite separation distance are well-known and allowed us to construct two different structural branches, denoted the "out"- and "in"-branches, respectively. Global energy minimizations showed that these branches are indeed the only relevant scenarios for the entire range of separation distances. We observed that the two branches remain meta-stable outside their respective stability regions even for (small) finite temperatures (as found in MC simulations); this provided evidence for a significant energy barrier between the two branches. Using the nudged elastic band (NEB) algorithm, we calculated the approximate energy barrier for a simple transition path. We found that the energy barrier grows with

system size.

The third system we investigated was the Wigner bilayer model. Since this system received a considerable amount of attention in the past, high-accuracy reference data are available for the case that both layers are characterized by the same background density and particle arrangement (denoted the symmetric case), allowing us to benchmark both our energy calculations and global optimizations. Again, we obtained excellent agreement in the observed energy and particle arrangement, reproducing all five observed structures and their stability regions. We then introduced additional complexity by adding asymmetry between the two plates' background charges. The two-dimensional phase diagram (in plate separation and charge asymmetry factor) was characterized by several interesting structural mechanisms, some of which were suitable for analytical treatment performed by Ladislav Šamaj and Emmanuel Trizac. Some of these structures were remarkably complex: to us, lattices featuring both triangular and rectangular structural units were of particular interest; these were similar to elongated triangular or snub square Archimedean tilings, which – in turn – are related to precursors of quasi-crystalline structures. All known limiting cases – both for the plate separation and for the asymmetry factor – were correctly reproduced. The structures observed in the symmetric case remained stable within a significant region of the phase diagram in the asymmetric case, in particular the square bilayer. The de-stabilization of the monolayer crystal in this model was directly linked to the problem of vertically displacing a single charge (similar as in the system discussed above). In order to quantify the observed structures, we used bond-orientational order parameters (BOOPs) and the number density ratio between the two layers. Using in addition an RGB color scheme for three BOOPs (denoted ΨRGB-scheme) we were able to identify many distinct regions in the phase diagram characterized by the same underlying structure formation. However, the structures in some regions of the phase diagram remained too complicated to classify. Most observed structures were characterized by a strong competition between commensurability considerations (favoring a discrete set of charge density ratios) and the effective charges of the two layers (favoring a continuous change in the charge density ratio as the plate separation and charge asymmetry factor are changed). This competition can lead to frustration, making MC simulations difficult; this problem could be largely avoided by choosing a proper starting configuration featuring an appropriate charge density ratio between the two layers.

The fourth system was a simple model for complex organic molecules; it was based on soft ellipsoids with an embedded linear quadrupole moment in a planar geometry in order to model both the aspheric shape and complex charge distribution of such molecules. Complexity was introduced by the competition between short- and long-range anisotropic interactions, which each favor different two-particle arrangements. We observed several basic structural mechanisms based either on the formation of uniform crystals or on the separation into parallel rows, which repel each other. Apart from a few more complicated – and possibly meta-stable – configurations, observed structures could be characterized by the occurrence of a single, two, or three specific particle orientations. Of particular interest were structures featuring square and trihexagonal lattices. Supplementary MD simulations

showed that the observed structures remain stable for low temperatures; strongly elongated ellipsoids proved to form the most stable structures, followed by spherical ones. For future work, extending our simple model to incorporate more properties of experimental systems such as organic molecules on surfaces or inverse patchy colloids (IPCs) would be promising. Such an endeavour entails moving to a quasi-2D geometry to allow multilayer arrangements, introducing particle-substrate interactions, and including more interaction sites per particle to more closely model a molecule's distinct shape and charge distribution. The structure formed by special organic molecules on inorganic substrates was shown to be switchable in experimental studies and gaining control of their self-assembly process would allow for both tunable materials and technologically interesting surface structures and properties.

5. Acknowledgments

At last, I would like to thank the many people I have met during my studies, many of whom have been a great help in getting things done.

Bianchi, **Arash Nikoubashman**, **Giannis Georgiou**, **Marta Montes Saralegui**, **Ulf Pedersen**, **Ismene Kolovos**, **Silvano Ferrari**, and **Clara Abaurrea Velasco** – lunch time would have been no fun without you all!

I would also like to thank the members of the Laboratoire de Physique Théorique at the Université Paris-Sud 11 – **Jean-Jacques Weis**, **Dominique Levesque**, **Jean-Michel Caillol**, **Cécile Appert-Rolland**, **Hendrik-Jan Hilhorst**, **Robert Salazar Rodriguez**, and **Sarah Klein** – for their hospitality during my stays in France. I have always enjoyed going there.

I am grateful to my friends both in Vienna and in Linz for providing much-needed distractions. Finally, I am very thankful for the continuing support and encouragement of my family – **Karin Antlanger**, **Leo Furtlehner**, and **Marlies Antlanger** – throughout all these years.

Bibliography

[1] Y. Yuan, T. Yin, M. Rong, and M. Zhang. Self healing in polymers and polymer composites. Concepts, realization and outlook: A review. *Express Polym. Lett.*, 2:238, 2008.

[2] E. Yablonovitch. Inhibited Spontaneous Emission in Solid-State Physics and Electronics. *Phys. Rev. Lett.*, 58:2059, 1987.

[3] T. Krauss, D. Rue, R. De La Rue, and S. Brand. Two-dimensional photonic-bandgap structures operating at near-infrared wavelengths. *Nature*, 383:699, 1996.

[4] N. Engheta and R. Ziolkowski. *Metamaterials: Physics and Engineering Explorations.* Wiley, 2006.

[5] S. Guenneau, A. Movchan, G. Petursson, and S. Ramakrishna. Acoustic metamaterials for sound focusing and confinement. *New J. Phys.*, 9:399, 2007.

[6] J. Page. Metamaterials: Neither solid nor liquid. *Nature Mater.*, 10:565, 2011.

[7] R. Shelby, D. Smith, and S. Schultz. Experimental Verification of a Negative Index of Refraction. *Science*, 292:77, 2001.

[8] W. Lu, J.-F. Jin, Z. Lin, and H. Chen. A simple design of an artificial electromagnetic black hole. *J. Appl. Phys.*, 108:064517, 2010.

[9] H. Yan, S. Park, G. Finkelstein, J. Reif, and T. LaBean. DNA-Templated Self-Assembly of Protein Arrays and Highly Conductive Nanowires. *Science*, 301:1882, 2003.

[10] L. Di Michele, F. Varrato, J. Kotar, S. Nathan, G. Foffi, and E. Eiser. Multistep kinetic self-assembly of DNA-coated colloids. *Nature Commun.*, 4:2007, 2013.

[11] O. Cayre, V. Paunov, and O. Velev. Fabrication of asymmtrically coated colloid particles by microcontact printing. *J. Mater. Chem.*, 13:2445, 2003.

[12] L. Hong, S. Jiang, and S. Granick. Simple Method to Produce Janus Colloidal Particles in Large Quantity. *Langmuir*, 22:9495, 2006.

[13] A. Pawar and I. Kretzschmar. Fabrication, Assembly, and Applications of Patchy Particles. *Macromol. Rapid Commun.*, 31:150, 2010.

[14] S. Gubin, Y. Koksharov, G. Khomutov, and G. Yurkov. Magnetic nanoparticles: preparation, structure and properties. *Russ. Chem. Rev.*, 74:489, 2005.

[15] M. Klokkenburg, C. Vonk, E. Claesson, J. Meeldijk, B. Erné, and A. Philipse. Direct Imaging of Zero-Field Dipolar Structures in Colloidal Disperisons of Synthetic Magnetite. *J. Am. Chem. Soc.*, 126:16706, 2004.

[16] M. Klokkenburg, R. Dullens, W. Kegel, B. Erné, and A. Philipse. Quantitative Real-Space Analysis of Self-Assembled Structures of Magnetic Dipolar Colloids. *Phys. Rev. Lett.*, 96:037203, 2006.

[17] M. Klokkenburg, B. Erné, J. Meeldijk, A. Wiedenmann, A. Petukhov, R. Dullens, and A. Philipse. *In Situ* Imaging of Field-Induced Hexagonal Columns in Magnetite Ferrofluids. *Phys. Rev. Lett.*, 97:185702, 2006.

[18] L. Baraban, D. Makarov, M. Albrecht, N. Rivier, P. Leiderer, and A. Erbe. Frustration-induced magic number clusters of colloidal magnetic particles. *Phys. Rev. E*, 77:031407, 2008.

[19] M. Wang, L. He, and Y. Yin. Magnetic field guided colloidal assembly. *Mater. Today*, 16:110, 2013.

[20] S. Glotzer and M. Solomon. Anisotropy of building blocks and their assembly into complex structures. *Nature Mat.*, 6:557, 2007.

[21] E. Bianchi, R. Blaak, and C. Likos. Patchy colloids: state of the art and perspectives. *Phys. Chem. Chem. Phys.*, 13:6397, 2011.

[22] J.-J. Weis and D. Levesque. Chain formation in low density dipolar hard spheres: A Monte Carlo study. *Phys. Rev. Lett.*, 71:2729, 1993.

[23] J.-J. Weis and D. Levesque. Ferroelectric phases of dipolar hard spheres. *Phys. Rev. E*, 48:3728, 1993.

[24] D. Levesque and J.-J. Weis. Orientational and structural order in strongly interacting dipolar hard spheres. *Phys. Rev. E*, 49:5131, 1994.

[25] C. Alvarez, M. Mazars, and J.-J. Weis. Structure and thermodynamics of a ferrofluid bilayer. *Phys. Rev. E*, 77:051501, 2008.

[26] J. Richardi, M. Pileni, and J.-J. Weis. Self-organization of confined dipolar particles in a parallel field. *J. Chem. Phys.*, 130:124515, 2009.

[27] D. Young and B. Alder. Melting-Curve Extrema from a Repulsive "Step" Potential. *Phys. Rev. Lett.*, 38:1213, 1977.

[28] G. Malescio and G. Pellicane. Stripe phases from isotropic repulsive interactions. *Nature Mater.*, 2:97, 2003.

[29] T. Dotera, T. Oshiro, and P. Ziherl. Mosaic two-lengthscale quadicrystals. *Nature*, 506:208, 2014.

[30] M. Rechtsman, F. Stillinger, and S. Torquato. Optimized Interactions for Targeted Self-Assembly: Application to a Honeycomb Lattice. *Phys. Rev. Lett.*, 95:228301, 2005.

[31] M. Rechtsman, F. Stillinger, and S. Torquato. Designed interaction potentials via inverse methods for self-assembly. *Phys. Rev. E*, 73:011406, 2006.

[32] P. Damasceno, M. Engel, and S. Glotzer. Predictive Self-Assembly of Polyhedra into Complex Structures. *Science*, 337:453, 2012.

[33] H. Ikezi. Coulomb solid of small particles in plasmas. *Phys. Fluids*, 29:1764, 1986.

[34] P. Shukla and A. Mamun. *Introduction to Dusty Plasma Physics.* IOP Publishing, 2002.

[35] D. Mendis. Dust in cosmic plasma environments. *Astrophys. Space Sci.*, 65:5, 1979.

[36] A.-H. Lu, E. Salabas, and F. Schüth. Magnetic Nanoparticles: Synthesis, Protection, Functionalization, and Application. *Angew. Chem. Int. Ed.*, 46:1222, 2007.

[37] R. Blakemore. Magnetotactic bacteria. *Science*, 24:4212, 1975.

[38] S. Brush, H. Salin, and E. Teller. Monte Carlo Study of a One-Component Plasma. I. *J. Chem. Phys.*, 45:2102, 1966.

[39] J.-P. Hansen. Statistical Mechanics of Dense Ionized Matter. I. Equilibrium Properties of the Classical One-Component Plasma. *Phys. Rev. A*, 8:3096, 1973.

[40] M. Baus and J.-P. Hansen. Statistical mechanics of simple Coulomb systems. *Phys. Rep.*, 59:1, 1980.

[41] R. Coldwell-Horsfall and A. Maradudin. Zero-Point Energy of an Electron Lattice. *J. Math. Phys.*, 1:395, 1960.

[42] P. Debye and E. Hückel. On the theory of electrolytes. I. Freezing point depression and related phenomena. *Phys. Z.*, 24:185, 1923.

[43] B. Larsen. Studies in statistical mechanics of Coulombic systems. I. Equation of state for the restricted primitive model. *J. Chem. Phys.*, 65:3431, 1976.

[44] P. Teixeira, J. Tavares, and M. Telo da Gama. The effect of dipolar forces on the structure and thermodynamics of classical fluids. *J. Phys.: Cond. Matt.*, 12:R411, 2000.

[45] L. Rovigatti, J. Russo, and F. Sciortino. Structural properties of the dipolar hard-sphere fluid at low temperatures and densities. *Soft Matter*, 8:6310, 2012.

[46] S. Kantorovich, R. Weeber, J. Cerda, and C. Holm. Ferrofluids with shifted dipoles: ground state structures. *Soft Matter*, 7:5217, 2011.

[47] S. Kantorovich, R. Weeber, J. Cerda, and C. Holm. Magnetic particles with shifted dipoles. *J. Magn. Magn. Mater.*, 323:1269, 2011.

[48] W. Stockmayer. Second Virial Coefficients of Polar Gases. *J. Chem. Phys.*, 9:398, 1941.

[49] B. Groh and S. Dietrich. Crystal structures and freezing of dipolar fluids. *Phys. Rev. E*, 63:021203, 2001.

[50] M. Miller, J. Shepherd, and D. Wales. Structural trends in clusters of quadrupolar spheres. *Mol. Phys.*, 106:1655, 2008.

[51] D. Frenkel and B. Smit. *Molecular Simulation.* Academic Press, 2 edition, 2002.

[52] E. Noya, I. Kolovos, G. Doppelbauer, G. Kahl, and E. Bianchi. Phase diagram of inverse patchy colloids assembling into an equilibrium laminar phase. *Soft Matter*, 10:8464, 2014.

[53] A. Ferrenberg and R. Swendsen. New Monte Carlo technique for studying phase transitions. *Phys. Rev. Lett.*, 61:2635, 1988.

[54] A. Ferrenberg and R. Swendsen. Optimized Monte Carlo data analysis. *Phys. Rev. Lett.*, 63:1195, 1989.

[55] A. Redlack and J. Grindlay. The Electrostatic Potential in a Finite Ionic Crystal. *Can. J. Phys.*, 50:2815, 1972.

[56] S. de Leeuw, J. Perram, and E. Smith. Simulation of Electrostatic Systems in Periodic Boundary Conditions. I. Lattice Sums and Dielectric Constants. *Proc. R. Soc. London A*, 373:27, 1980.

[57] S. de Leeuw, J. Perram, and E. Smith. Simulation of Electrostatic Systems in Periodic Boundary Conditions. II. Equivalence of Boundary Conditions. *Proc. R. Soc. London A*, 373:57, 1980.

[58] E. Smith. Electrostatic Energy in Ionic Crystals. *Proc. R. Soc. London A*, 375:475, 1981.

[59] S. de Leeuw, J. Perram, and E. Smith. Simulation of Electrostatic Systems in Periodic Boundary Conditions. III. Further Theory and Applications. *Proc. R. Soc. London A*, 388:177, 1983.

[60] J. Caillol. Comments on the numerical simulations of electrolytes in periodic boundary conditions. *J. Chem. Phys.*, 101:6080, 1994.

[61] H. Herce, A. Garcia, and T. Darden. The electrostatic surface term: (I) periodic systems. *J. Chem. Phys.*, 126:124106, 2007.

[62] J. Jackson. *Classical Electrodynamics.* Wiley, 3rd edition, 1998.

[63] V. Ballenegger. On the origin of the surface term in the Ewald formula. *J. Chem. Phys.*, 140:161102, 2014.

[64] E. Smith. Calculating the pressure in simulations using periodic boundary conditions. *J. Stat. Phys.*, 77:449, 1994.

[65] P. Ewald. Die Berechnung optischer und elektrostatischer Gitterpotentiale. *Ann. Phys.*, 369:253, 1921.

[66] J. Lekner. Summation of Coulomb fields in computer-simulated systems. *Physica A*, 176:485, 1991.

[67] T. Darden, D. York, and L. Pedersen. Particle mesh Ewald: An $N \cdot \log(N)$ method for Ewald sums in large systems. *J. Chem. Phys.*, 98:10089, 1993.

[68] H. Petersen. Accuracy and efficiency of the particle mesh Ewald method. *J. Chem. Phys.*, 103:3668, 1995.

[69] J. Eastwood, R. Hockney, and D. Lawrence. P3M3DP – the three-dimensional periodic particle-particle/particle-mesh program. *Comp. Phys. Comm.*, 19:215, 1980.

[70] M. Deserno and C. Holm. How to mesh up Ewald sums. I. A theoretical and numerical comparison of various particle mesh routines. *J. Chem. Phys.*, 109:7678, 1998.

[71] M. Deserno and C. Holm. How to mesh up Ewald sums. II. An accurate error estimate for the particle-particle-particle-mesh algorithm. *J. Chem. Phys.*, 109:7694, 1998.

[72] A. Arnold and C. Holm. *"Efficient methods to compute long range interactions for soft matter systems" in Advanced Computer Simulation Approaches for Soft Matter Sciences II.* Advances in Polymer Sciences. Springer, 2005.

[73] J.-M. Caillol and D. Gilles. Numerical simulations of screened Coulomb systems. A comparison between hyperspherical and periodic boundary conditions. *J. Stat. Phys.*, 100:905, 2000.

[74] J.-M. Caillol and D. Gilles. Monte Carlo simulations of the Yukawa one-component plasma. *J. Stat. Phys.*, 100:933, 2000.

[75] M. Mazars. Long ranged interactions in computer simulations and for quasi-2D systems. *Phys. Rep.*, 500:43, 2011.

[76] E. Madelung. Das elektrische Feld in Systemen von regelmäßig angeordneten Punktladungen. *Phys. Zs.*, 19:524, 1918.

[77] I. Gradshteyn and I. Ryzhik. *Table of Integrals, Series, and Products*, volume 36 of *Mathematics of Computation*. American Mathematical Society, 1981.

[78] J. Bryngelson, J. Onuchic, N. Socci, and P. Wolynes. Funnels, Pathways, and the Energy Landscape of Protein Folding: A Synthesis. *Proteins: Struct. Funct. Genet.*, 21:167, 1995.

[79] D. Leeson, F. Gai, H. Rodriguez, L. Gregoret, and R. Dyer. Protein folding and unfolding on a complex energy landscape. *PNAS*, 97:2527, 2000.

[80] B. Robson and A. Vaithilingham. Protein Folding Revisited. *Prog. Mol. Biol. Transl. Sci.*, 84:161, 2008.

[81] J. Douglas. *Conceptual Design of Chemical Processes*. McGraw-Hill, 1988.

[82] M. Emmerich, B. Groß, F. Henrich, P. Roosen, and M. Schütz. Global optimization of chemical engineering plants by means of evolutionary algorithms. *Proc. ASPEN World*, 2000.

[83] R. Horst and H. Tuy. *Global Optimization: Deterministic Approaches*. Springer, 1996.

[84] E. Hansen. *Global Optimization using Interval Analysis*. Marcel Dekker, 1992.

[85] R. Strongin and Y. Sergeyev. *Global optimization with non-convex constraints: Sequential and parallel algorithms*. Kluwer Academic Publishers, 2000.

[86] W. Wenzel and K. Hamacher. Stochastic Tunneling Approach for Global Minimization of Complex Potential Energy Landscapes. *Phys. Rev. Lett.*, 82:3003, 1999.

[87] K. Hamacher and W. Wenzel. The Scaling Behaviour of Stochastic Minimization Algorithms in a Perfect Funnel Landscape. *Phys. Rev. E*, 59:938, 1999.

[88] S. Kirkpatrick, C. Gelatt, and M. Vecchi. Optimization by Simulated Annealing. *Science*, 220:4598, 1983.

[89] V. Černý. Thermodynamical approach to the traveling salesman problem: An efficient simulation algorithm. *J. Opt. Th. App.*, 45:41, 1985.

[90] R. Swendsen and J. Wang. Replica Monte Carlo simulation of spin glasses. *Phys. Rev. Lett.*, 57:2607, 1986.

[91] D. Wolpert and W. Macready. No Free Lunch Theorems for Optimization. *IEEE Trans. Ev. Comp.*, 1:67, 1997.

[92] J. Kennedy and R. Eberhart. Particle Swarm Optimization. *Proc. IEEE Int. Conf. Neur. Net.*, 4:1942, 1995.

[93] Y. Shi and R. Eberhart. A modified particle swarm optimizer. *Proc. IEEE Int. Conf. Evol. Comput.*, page 69, 1998.

[94] R. Battiti and G. Tecchiolli. The reactive tabu search. *ORSA J. Comp.*, 6:126, 1994.

[95] A. Blake and A. Zisserman. *Visual Reconstruction*. MIT Press, 1987.

[96] R. Storn and K. Price. Differential evolution - a simple and efficient heuristic for global optimization over continuous spaces. *J. Glob. Opt.*, 11:341, 1997.

[97] J. Holland. *Adaptation in Natural and Artificial Systems*. The University of Michigan Press, 1975.

[98] D. Gottwald. *Genetic Algorithms in Condensed Matter Theory.* PhD thesis, Vienna University of Technology, 2005.

[99] C. Broyden. The convergence of a class of double-rank minimization algorithms. *J. Inst. Math. Appl.*, 6:76, 1970.

[100] R. Fletcher. A New Approach to Variable Metric Algorithms. *Comp. J.*, 13:317, 1970.

[101] D. Goldfarb. A family of variable-metric methods derived by variational means. *Math. Comput.*, 24:23, 1970.

[102] D. Shanno. Conditioning of quasi-Newton methods for function minimization. *Math. Comput.*, 24:647, 1970.

[103] D. Liu and J. Nocedal. On the Limited Memory Method for Large Scale Optimization. *Math. Prog. B*, 45:503, 1989.

[104] R. Byrd, P. Lu, J. Nocedal, and C. Zhu. A Limited Memory Algorithm for Bound Constrained Optimization. *SIAM J. Scient. Stat. Comput.*, 16:1190, 1995.

[105] P. Moscato. On Evolution, Search, Optimization, Genetic Algorithms and Martial Arts: Towards Memetic Algorithms. Technical report, Caltech Concurrent Computation Program, 1989.

[106] G. Doppelbauer. *Ordered Equilibrium Structures of Patchy Particle Systems.* PhD thesis, Vienna University of Technology, 2012.

[107] C. Darwin. *On the Origin of Species.* J. Murray, 1859.

[108] D. Chakrabarti and D. Wales. Simulations of rigid bodies in an angle-axis framework. *Phys. Chem. Chem. Phys.*, 11:1970, 2009.

[109] D. Gottwald, G. Kahl, and C. Likos. Predicting equilibrium structures in freezing processes. *J. Chem. Phys.*, 122:204503, 2005.

[110] J. Fornleitner. *Ordered equilibrium structures of two-dimensional soft matter systems.* PhD thesis, Vienna University of Technology, 2008.

[111] J. Fornleitner and G. Kahl. Lane formation vs. cluster formation in two-dimensional square-shoulder systems: a genetic algorithm approach. *EPL*, 82:18001, 2008.

[112] D. Wales and J. Doye. Global Optimization by Basin-Hopping and the Lowest Energy Structures of Lennard-Jones Clusters Containing up to 110 Atoms. *J. Phys. Chem. A*, 101:5111, 1997.

[113] W. Gropp, E. Lusk, and A. Skjellum. *Using MPI: Portable Parallel Programming with the Message Passing Interface.* MIT Press, 1994.

[114] B. Hartke. Global cluster geometry optimization by a phenotype algorithm with

Niches: Location of elusive minima, and low-order scaling with cluster size. *J. Comput. Chem.*, 20:1752, 1999.

[115] D. Deaven and K. Ho. Molecular geometry optimization with a genetic algorithm. *Phys. Rev. Lett.*, 75:288, 1995.

[116] C. Glass, A. Oganov, and N. Hansen. USPEX – Evolutionary crystal structure prediction. *Comput. Phys. Commun.*, 175:713, 2006.

[117] N. Abraham and M. Probert. A periodic genetic algorithm with real-space representation for crystal structure and polymorph prediction. *Phys. Rev. B*, 73:224104, 2006.

[118] D. Lonie and E. Zurek. XtalOpt: An open-source evolutionary algorithm for crystal structure prediction. *Comput. Phys. Commun.*, 182:372, 2011.

[119] A. Oganov and C. Glass. Crystal structure prediction using *ab initio* evolutionary techniques: Principles and applications. *J. Chem. Phys.*, 124:244704, 2006.

[120] N. Metropolis, A. Rosenbluth, M. Rosenbluth, A. Teller, and E. Teller. Equations of State Calculations by Fast Computing Machines. *J. Chem. Phys.*, 21:1087, 1953.

[121] W. Hastings. Monte Carlo Sampling Methods Using Markov Chains and Their Applications. *Biometrika*, 57:97, 1970.

[122] M. Allen and D. Tildesley. *Computer Simulation of Liquids*. Clarendon Press, 1987.

[123] P. Chaikin and T. Lubensky. *Principles of Condensed Matter Physics*. Cambridge University Press, 2000.

[124] L. Landau. On the theory of phase transitions. *Zh. Eksp. Teor. Fiz.*, 7:19, 1937.

[125] J. Mayer and S. Streeter. Phase Transitions. *J. Chem. Phys.*, 7:1019, 1939.

[126] M. Challa, D. Landau, and K. Binder. Finite-size effects at temperature-driven first-order transitions. *Phys. Rev. B*, 34:1841, 1986.

[127] K. Binder. Theory of first-order phase transitions. *Rep. Prog. Phys.*, 50:783, 1987.

[128] G. Dirichlet. Über die Reduktion der positiven quadratischen Formen mit drei unbestimmten ganzen Zahlen. *Journal für die Reine und Angewandte Mathematik*, 40:209, 1850.

[129] G. Voronoi. Nouvelles applications des paramètres continus à la théorie des formes quadratiques. *Journal für die Reine und Angewandte Mathematik*, 133:97, 1908.

[130] K. Strandburg, J. Zollweg, and G. Chester. Bond-angular order in two-dimensional Lennard-Jones and hard-disk systems. *Phys. Rev. B*, 30:2755, 1984.

[131] K. Strandburg. Two-dimensional melting. *Rev. Mod. Phys.*, 60:161, 1988.

[132] D. Caspar and E. Fontano. Five-fold symmetry in crystalline quasicrystal lattices. *PNAS*, 93:14271, 1996.

[133] P. Steinhardt, D. Nelson, and M. Ronchetti. Bond-orientational order in liquids and glasses. *Phys. Rev. B*, 28:784, 1983.

[134] W. Mickel, S. Kapfer, G. Schröder-Turk, and K. Mecke. Shortcomings of the bond orientational order parameters for the analysis of disordered particulate matter. *J. Chem. Phys.*, 138:044501, 2013.

[135] H. Jónsson, G. Mills, and K. Jacobsen. *Nudged Elastic Band Method for Finding Minimum Energy Paths of Transitions*. Classical and Quantum Dynamics in Condensed Phase Simulations. World Scientific, 1998.

[136] G. Henkelman and H. Jónsson. Improved tangent estimate in the nudged elastic band method for finding minimum energy paths and saddle points. *J. Chem. Phys.*, 113:9978, 2000.

[137] S. Smidstrup, A. Pedersen, K. Stokbro, and H. Jónsson. Improved initial guess for minimum energy path calculations. *J. Chem. Phys.*, 140:214106, 2014.

[138] E. Wigner. On the Interaction of Electrons in Metals. *Phys. Rev.*, 46:1002, 1934.

[139] L. Bonsall and A. Maradudin. Some static and dynamical properties of a two-dimensional Wigner crystal. *Phys. Rev. B*, 15:1959, 1977.

[140] S. Earnshaw. On the nature of the molecular forces which regulate the constitution of the luminferous ether. *Trans. Camb. Phil. Soc.*, 7:97, 1842.

[141] A. Fontecha, H. Schöpe, H. König, T. Palberg, R. Messina, and H. Löwen. A comparative study on the phase behaviour of highly charge colloidal spheres in a confining wedge geometry. *J. Phys.: Cond. Matt.*, 17:S2779, 2005.

[142] E. Oğuz, A. Reinmüller, H. Schöpe, T. Palberg, R. Messina, and H. Löwen. Crystalline multilayers of charged colloids in soft confinement: experiment versus theory. *J. Phys.: Cond. Matt.*, 24:464123, 2012.

[143] C. Grimes and G. Adams. Evidence for a Liquid-to-Crystal Phase Transition in a Classical, Two-Dimensional Sheet of Electrons. *Phys. Rev. Lett.*, 42:795, 1979.

[144] J. Yamanaka, H. Yoshida, T. Koga, N. Ise, and T. Hashimoto. Reentrant Solid-Liquid Transition in Ionic Colloidal Dispersions by Varying Particle Charge Density. *Phys. Rev. Lett.*, 80:5806, 1998.

[145] H. Yoshida, J. Yamanaka, T. Koga, T. Koga, N. Ise, and T. Hashimoto. Transitions between Ordered and Disordered Phases and Their Coexistence in Dilute Ionic Colloidal Dispersions. *Langmuir*, 15:2684, 1999.

[146] M. Antlanger and G. Kahl. Wigner crystals for a planar, equimolar binary mixture of classical, charged particles. *Cond. Matt. Phys.*, 16:43501, 2013.

[147] M. Kanduč, M. Trulsson, A. Naji, Y. Burak, J. Forsman, and R. Podgornik. Weak- and strong-coupling electrostatic interactions between asymmetrically charged planar surfaces. *Phys. Rev. E*, 78:061105, 2008.

[148] R. Messina, C. Holm, and K. Kremer. Ground state of two unlike charged colloids: An analogy with ionic bonding. *EPL*, 51:461, 2000.

[149] L. Šamaj and E. Trizac. Ground state of classical bilayer Wigner crystals. *EPL*, 98:36004, 2012.

[150] L. Šamaj and E. Trizac. Critical phenomena and phase sequence in a classical bilayer Wigner crystal at zero temperature. *Phys. Rev. B*, 85:205131, 2012.

[151] M. Antlanger, M. Mazars, L. Šamaj, G. Kahl, and E. Trizac. Taking one charge off a two-dimensional Wigner crystal. *Mol. Phys.*, 112:1336, 2014.

[152] Y. Monarkha and K. Kono. *Two-Dimensional Coulomb Liquids and Solids – Springer Series in Solid-State Science.* Springer, 2004.

[153] B. Clark, M. Casula, and D. Ceperley. Hexatic and Mesoscopic Phases in a 2D Quantum Coulomb System. *Phys. Rev. Lett.*, 103:055701, 2009.

[154] P. Peczak and D. Landau. Monte Carlo study of finite-size effects at a weakly first-order phase transition. *Phys. Rev. B*, 39:11932, 1989.

[155] J. Lee and J. Kosterlitz. Finite-size scaling and Monte Carlo simulations of first-order phase transitions. *Phys. Rev. B*, 43:3265, 1991.

[156] N. Ashcroft and N. Mermin. *Solid State Physics.* Thomson Learning, 1976.

[157] G. Goldoni and F. Peeters. Stability, dynamical properties, and melting of a classical bilayer Wigner crystal. *Phys. Rev. B*, 53:4591, 1996.

[158] J.-J. Weis, D. Levesque, and S. Jorge. Solid phase diagram of a classical electronic bilayer. *Phys. Rev. B*, 63:045308, 2001.

[159] T. Mitchell, J. Bollinger, D. Dubin, X.-P. Huang, W. Itano, and R. Baughman. Direct Observations of Structural Phase Transitions in Planar Crystallized Ion Plasmas. *Science*, 282:1290, 1998.

[160] H. Manoharan, Y. Suen, M. Santos, and M. Shayegan. Evidence for a Bilayer Quantum Wigner Solid. *Phys. Rev. Lett.*, 77:1813, 1996.

[161] E. Tutuc and M. Shayegan. Counterflow Measurements in Strongly Correlated GaAs Hole Bilayers: Evidence for Electron-Hole Pairing. *Phys. Rev. Lett.*, 93:036802, 2004.

[162] Z. Wang, Y. Chen, L. Engel, D. Tsui, E. Tutuc, and M. Shayegan. Pinning modes and interlayer correlation in high-magnetic-field bilayer Wigner solids. *Phys. Rev. Lett.*, 99:3, 2007.

[163] Z. Wang, Y. Chen, H. Zhu, L. Engel, D. Tsui, E. Tutuc, and M. Shayegan. Unequal layer densities in bilayer Wigner crystal at high magnetic fields. *Phys. Rev. B*, 85:195408, 2012.

[164] L.-W. Teng, P.-S. Tu, and L. I. Microscopic Observation of Confinement-Induced Layering and Slow Dynamics of Dusty-Plasma Liquids in Narrow Channels. *Phys. Rev. Lett.*, 90:245004, 2003.

[165] A. Mayorov, D. Elias, M. Mucha-Kruczynski, R. Gorbachev, T. Tudorovskiy, A. Zhukov, S. Morozov, M. Katsnelson, V. Fal'ko, A. Geim, and K. Novoselov. Interaction-Driven Spectrum Reconstruction in Bilayer Graphene. *Science*, 333:860, 2011.

[166] H. Imamura, P. Maksym, and H. Aoki. Magic numbers and optical-absorption spectrum in vertically coupled quantum dots in the fractional quantum Hall regime. *Phys. Rev. B*, 53:12613, 1996.

[167] R. Messina and H. Löwen. Reentrant Transitions in Colloidal or Dusty Plasma Bilayers. *Phys. Rev. Lett.*, 91:146101, 2003.

[168] M. Mazars. Bond orientational order parameters in the crystalline phases of the classical Yukawa-Wigner bilayers. *EPL*, 84:55002, 2008.

[169] R. Morf. Temperature Dependence of the Shear Modulus and Melting of the Two-Dimensional Electron Solid. *Phys. Rev. Lett.*, 43:931, 1979.

[170] R. Gann, S. Chakravarty, and G. Chester. Monte Carlo simulation of the classical two-dimensional one-component plasma. *Phys. Rev. B*, 20:326, 1979.

[171] M. Mazars. The melting of the classical two-dimensional Wigner crystal. *EPL*, 110:26003, 2015.

[172] E. Oğuz, R. Messina, and H. Löwen. Crystalline multilayers of the confined Yukawa system. *EPL*, 86:28002, 2009.

[173] M. Antlanger, M. Mazars, L. Šamaj, G. Kahl, and E. Trizac. The rich polymorphic behaviour of Wigner bilayers (in preparation). 2015.

[174] J. Mikhael, J. Roth, L. Helden, and C. Bechinger. Archimedean-like tiling on decagonal quadicrystalline surfaces. *Nature*, 454:501, 2008.

[175] S. Ranganathan and R. Johnson. Asymmetric electron bilayer: A molecular dynamics study of correlations and diffusion. *Phys. Rev. B*, 78:195323, 2008.

[176] J. Günster, G. Liu, V. Kempter, and D. Goodman. Adsorption of benzene on Mo(100)

and MgO(100)/Mo(100) studied by ultraviolet photoelectron and metastable impact electron spectroscopy. *Surf. Science*, 415:303, 1998.

[177] K. Cui, O. Ivasenko, K. Mali, D. Wu, X. Feng, K. Müllen, S. De Feyter, and S. Mertens. Potential-driven molecular tiling of a charged polycyclic aromatic compound. *Chem. Commun.*, 50:10376, 2014.

[178] K. Cui, F. Schlütter, O. Ivasenko, M. Kivala, M. Schwab, S.-L. Lee, S. Mertens, K. Tahara, Y. Tobe, K. Müllen, K. Mali, and S. de Feyter. Multicomponent Self-Assembly with a Shape-Persistent N-Heterotriangulene Macrocycle on Au(111). *Chem. Eur. J.*, 21:1652, 2015.

[179] K. Palczynski, G. Heimel, J. Heyda, and J. Dzubiella. Growth and Characterization of Molecular Crystals of *para*-Sexiphenyl by All-Atom Computer Simulations. *Cryst. Growth Des.*, 14:3791, 2014.

[180] N. Kleppmann and S. Klapp. A scale-bridging modeling approach for anisotropic organic molecules at patterned semiconductor surfaces. *J. Chem. Phys.*, 142:064701, 2015.

[181] K. Cui, K. Mali, O. Ivasenko, D. Wu, X. Feng, M. Walter, K. Müllen, S. De Feyter, and S. Mertens. Squeezing, then stacking: From breathing pores to three-dimensional ionic self-assembly under electrochemical control. *Angew. Chem. Int. Ed.*, 53:12951, 2014.

[182] J. Gay and B. Berne. Modification of the overlap potential to mimic a linear site-site potential. *J. Chem. Phys.*, 74:3316, 1981.

[183] I. Georgiou, P. Ziherl, and G. Kahl. Antinematic local order in dendrimer liquids. *EPL*, 106:44004, 2014.

[184] I. Georgiou. *Simulations of Soft Matter Systems*. PhD thesis, Vienna University of Technology, 2014.

[185] T. Heinemann, M. Antlanger, M. Mazars, G. Kahl, and S. Klapp. Structures formed by two-dimensional ellipsoids with embedded linear quadrupole moment (in preparation). 2015.

[186] R. Koch, J. Finnerty, and T. Bruhn. Theoretical study on the nonlinear optical properties of phenylenes and influencing factors. *J. Phys. Org. Chem.*, 21:954, 2008.

[187] J. Roales, J. Pedrosa, P. Castillero, M. Cano, T. Richardson, Á. Barranco, and A. González-Elipe. Selective Detection of Volatile Organic Compounds by Spectral Imaging of Porphyrin Derivatives Bound to TiO_2 Porous Films. *ACS Appl. Mater. Interfaces*, 4:5147, 2012.

[188] T. Heinemann, K. Palczynski, J. Dzubiella, and S. Klapp. Angle-resolved effective potentials for disk-shaped molecules. *J. Chem. Phys.*, 141:214110, 2014.

[189] E. Bianchi, C. Likos, and G. Kahl. Self-Assembly of Heterogeneously Charged Particles under Confinement. *ACS Nano*, 7:4657, 2013.

[190] P. van Oostrum, M. Hejazifar, C. Niedermayer, and E. Reimhult. Simple method for the synthesis of inverse patchy colloids. *JPCM*, 27:234105, 2015.

A. Appendix

A.1. Ewald summation for a bilayer Wigner crystal

In this section, we present the derivation of Ewald summation for a system of classical point charges in the presence of two parallel planar uniform neutralizing backgrounds. This derivation of the *intra*-layer terms is similar to the case of the Wigner monolayer (see Subsection 2.1.3), but introduces interactions between the two layers, i.e., *inter*-layer terms. We first define the system and its parameters (see Subsection A.1.1) and then derive the Ewald summation (see Subsection A.1.2). Finally, we comment on the implementation of Ewald summation and computational details (see Subsection A.1.3).

A.1.1. Bilayer Wigner crystal

The bilayer Wigner crystal is periodic in two dimensions. It consists of N point charges Q_i per unit cell and two parallel planar uniform backgrounds with charge densities σ_1 and σ_2, respectively. For simplicity, we assume that all charges are indistinguishable, i.e., $Q_i = Q$. Since the charges condense on either plate at zero temperature (due to the Earnshaw theorem), we can define the particle number densities at the two plates $\rho_1 = N_1/S_0$ and $\rho_2 = N_2/S_0$, such that $N_1 + N_2 = N$ and $\rho_1 + \rho_2 = \rho$. Electro-neutrality states that

$$\rho Q + \sigma = 0 \tag{A.1}$$
$$(\rho_1 Q + \sigma_1) + (\rho_2 Q + \sigma_2) = 0. \tag{A.2}$$

We define *local* electro-neutrality if each layer carries no net charge, i.e., $\rho_i Q + \sigma_i = 0$ for $i = 1, 2$.

A.1.2. Derivation of Ewald summation for the bilayer Wigner crystal

The total interaction energy of the system E can be divided into *intra*- (11 and 22) and *inter*-layer (12 and 21) terms, as well as in particle-particle (pp), particle-background (pb), and background-background (bb) terms. Starting from the different contributions

$$E_{\mathrm{pp}} = E_{\mathrm{pp}}^{(1)} + E_{\mathrm{pp}}^{(2)} + E_{\mathrm{pp}}^{(12)} + E_{\mathrm{pp}}^{(21)} \tag{A.3}$$
$$E_{\mathrm{pb}} = E_{\mathrm{pb}}^{(1)} + E_{\mathrm{pb}}^{(2)} + E_{\mathrm{pb}}^{(12)} + E_{\mathrm{pb}}^{(21)} \tag{A.4}$$
$$E_{\mathrm{bb}} = E_{\mathrm{bb}}^{(1)} + E_{\mathrm{bb}}^{(2)} + E_{\mathrm{bb}}^{(12)} + E_{\mathrm{bb}}^{(21)}, \tag{A.5}$$

we again seek to derive the Ewald summation and arrive at separate real space sums, reciprocal space sums, constant contributions, and divergent terms

$$
\begin{align}
E^{(r)} &= E^{(r,1)} + E^{(r,2)} + E^{(r,12)} + E^{(r,21)} \tag{A.6} \\
E^{(k)} &= E^{(k,1)} + E^{(k,2)} + E^{(k,12)} + E^{(k,21)} \tag{A.7} \\
E^{(c)} &= E^{(c,1)} + E^{(c,2)} + E^{(c,12)} + E^{(c,21)} \tag{A.8} \\
E^{(\mathrm{div})} &= E^{(\mathrm{div},1)} + E^{(\mathrm{div},2)} + E^{(\mathrm{div},12)} + E^{(\mathrm{div},21)}. \tag{A.9}
\end{align}
$$

The intra-layer parts are identical to the ones derived for the monolayer system and we obtain immediately

$$
E^{(r,1)} = \frac{1}{2} Q^2 \sum_{i \in L_1} \sum_{j \in L_1} {\sum_{\boldsymbol{R}}}' \frac{1}{r} \mathrm{erfc}\,(\alpha r) \tag{A.10}
$$

$$
E^{(k,1)} = \frac{\pi}{S_0} Q^2 \sum_{\boldsymbol{G} \neq 0} \left\| \sum_{i \in L_1} \exp\,(\imath \boldsymbol{G} \cdot \boldsymbol{r}_i) \right\|^2 \frac{1}{G} \mathrm{erfc}\,\left(\frac{G}{2\alpha} \right) \tag{A.11}
$$

$$
E^{(c,1)} = -\frac{\sqrt{\pi}}{\alpha S_0} Q^2 N_1^2 - \frac{\alpha}{\sqrt{\pi}} Q^2 N_1 \tag{A.12}
$$

$$
E^{(\mathrm{div},1)} = \left[2\sqrt{\pi}\sigma_1 Q N_1 + \sqrt{\pi}\sigma_1^2 S_0 + \frac{\sqrt{\pi}}{S_0} Q^2 N_1^2 \right] \lim_{\epsilon \to 0} \frac{1}{\sqrt{\epsilon}}, \tag{A.13}
$$

where exchanging $1 \to 2$ yields the respective terms for the second layer. Note that the sums are only carried out for particles in the respective layer. We would also like to point out that local electro-neutrality is not necessarily given, i.e., the divergent terms do not have to cancel out.

We now develop the inter-layer terms, splitting them into (pp)-, (pb)-, and (bb)-contributions. We obtain

$$
E^{(12)}_{\mathrm{pp}} = Q^2 \sum_{i \in L_1} \sum_{j \in L_2} \sum_{\boldsymbol{R}} \frac{1}{|\boldsymbol{r}_i - \boldsymbol{r}_j + \boldsymbol{R}|} \tag{A.14}
$$

$$
E^{(12)}_{\mathrm{pb}} = Q\sigma_2 \sum_{i \in L_1} \int_L \sum_{\boldsymbol{R}} \frac{d\boldsymbol{r}}{|\boldsymbol{r}_i - \boldsymbol{r} + \boldsymbol{R}|} \tag{A.15}
$$

$$
E^{(12)}_{\mathrm{bb}} = \sigma_1 \sigma_2 \sum_{\boldsymbol{R}} \int_L \int_L \frac{d\boldsymbol{r}\,d\boldsymbol{r}'}{|\boldsymbol{r} - \boldsymbol{r}' + \boldsymbol{R}|}, \tag{A.16}
$$

where exchanging $1 \leftrightarrow 2$ yields the complementary terms. The integration over L covers the entire unit cell, the shape of which is the same for both layers. Using the same identities as

for the monolayer, we can transform these terms into

$$
\begin{aligned}
E_{\text{pp}}^{(12)} &= \frac{1}{\sqrt{\pi}} Q^2 \sum_{i \in L_1} \sum_{j \in L_2} \sum_{\mathbf{R}} \left[\lim_{\epsilon \to 0} \int_{\epsilon}^{\alpha^2} \frac{dt}{\sqrt{t}} \exp\left(- |\mathbf{r}_i - \mathbf{r}_j + \mathbf{R}|^2 t \right) \right. \\
&\quad \left. + \int_{\alpha^2}^{\infty} \frac{dt}{\sqrt{t}} \exp\left(- |\mathbf{r}_i - \mathbf{r}_j + \mathbf{R}|^2 t \right) \right]
\end{aligned}
\tag{A.17}
$$

$$
E_{\text{pb}}^{(12)} = \frac{\sigma_2}{\sqrt{\pi}} Q N_1 \int_{r=0}^{\infty} 2\pi r dr \lim_{\epsilon \to 0} \int_{\epsilon}^{\infty} \frac{dt}{\sqrt{t}} \exp\left(-r^2 t \right)
\tag{A.18}
$$

$$
E_{\text{bb}}^{(12)} = \frac{\sigma_1 \sigma_2}{2\sqrt{\pi}} \int_L \int_{r=0}^{\infty} 2\pi r dr \lim_{\epsilon \to 0} \int_{\epsilon}^{\infty} \frac{dt}{\sqrt{t}} \exp\left(-r^2 t \right).
\tag{A.19}
$$

If we now consider that the relation between the three-dimensional distance $\mathbf{r}$ and its two-dimensional projection $\mathbf{s}$, $r^2 = s^2 + h^2$, we obtain

$$
\begin{aligned}
E_{\text{pp}}^{(12)} &= \frac{1}{\sqrt{\pi}} Q^2 \sum_{i \in L_1} \sum_{j \in L_2} \sum_{\mathbf{R}} \left[\lim_{\epsilon \to 0} \int_{\epsilon}^{\alpha^2} \frac{dt}{\sqrt{t}} \exp\left(- |\mathbf{r}_i - \mathbf{r}_j + \mathbf{R}|^2 t \right) \right. \\
&\quad \left. + \int_{\alpha^2}^{\infty} \frac{dt}{\sqrt{t}} \exp\left(- |\mathbf{r}_i - \mathbf{r}_j + \mathbf{R}|^2 t \right) \right]
\end{aligned}
\tag{A.20}
$$

$$
E_{\text{pb}}^{(12)} = \frac{\sigma_2}{\sqrt{\pi}} Q N_1 \int_{r=0}^{\infty} 2\pi s ds \lim_{\epsilon \to 0} \int_{\epsilon}^{\infty} \frac{dt}{\sqrt{t}} \exp\left(-s^2 t \right) \left(-h^2 t \right)
\tag{A.21}
$$

$$
E_{\text{bb}}^{(12)} = \frac{\sigma_1 \sigma_2}{2\sqrt{\pi}} S_0 \int_{s=0}^{\infty} 2\pi s ds \lim_{\epsilon \to 0} \int_{\epsilon}^{\infty} \frac{dt}{\sqrt{t}} \exp\left(-s^2 t \right) \exp\left(-h^2 t \right).
\tag{A.22}
$$

We can transform the latter two terms using

$$
2\pi \lim_{\epsilon \to 0} \int_{\epsilon}^{\infty} \frac{dt}{\sqrt{t}} \exp\left(-h^2 t \right) \int_{s=0}^{\infty} s \exp\left(-s^2 t \right) ds = \pi \lim_{\epsilon \to 0} \int_{\epsilon}^{\infty} \frac{dt}{t^{3/2}} \exp\left(-h^2 t \right)
\tag{A.23}
$$

$$
= -2\pi^{3/2} h + 2\pi \lim_{\epsilon \to 0} \frac{1}{\sqrt{\epsilon}},
\tag{A.24}
$$

into

$$
E_{\text{pb}}^{(12)} = -\sigma_1 \sigma_2 \pi S_0 h + \sigma_1 \sigma_2 \sqrt{\pi} S_0 \lim_{\epsilon \to 0} \frac{1}{\sqrt{\epsilon}}
\tag{A.25}
$$

$$
E_{\text{bb}}^{(12)} = -2\sigma_2 Q N_1 \pi h + 2\sigma_2 Q N_1 \sqrt{\pi} \lim_{\epsilon \to 0} \frac{1}{\sqrt{\epsilon}}.
\tag{A.26}
$$

For the (pp)-term, we – as before – convert the first part of the integral into a reciprocal space summation (splitting off the $\mathbf{G} = 0$-term) and carry out the second integral. We

obtain

$$
\begin{aligned}
E_{\mathrm{pp}}^{(12)} &= \frac{Q^2}{\sqrt{\pi}} \sum_{i \in L_1} \sum_{j \in L_2} \left[\frac{\pi}{S_0} \lim_{\epsilon \to 0} \int_\epsilon^\infty \exp\left(-h^2 t\right) \frac{dt}{t^{3/2}} \right. \tag{A.27} \\
&\quad \left. + \frac{\pi}{S_0} \sum_{\boldsymbol{G} \neq 0} \exp\left(\imath \boldsymbol{G} \cdot \boldsymbol{s}_i\right) \exp\left(-\imath \boldsymbol{G} \cdot \boldsymbol{s}_j\right) \lim_{\epsilon \to 0} \int_\epsilon^\infty \exp\left(-h^2 t\right) \exp\left(-\frac{G^2}{4t}\right) \frac{dt}{t^{3/2}} \right] \\
&\quad + Q^2 \sum_{i \in L_1} \sum_{j \in L_2} \sum_{\boldsymbol{R}} \frac{1}{r} \mathrm{erfc}\left(\alpha r\right) \\
&= \frac{2\sqrt{\pi}}{S_0} N_1 N_2 Q^2 \left[-\sqrt{\pi} h \mathrm{erf}\left(\alpha h\right) - \frac{1}{\alpha} \exp\left(-\alpha^2 h^2\right) + \lim_{\epsilon \to 0} \frac{1}{\sqrt{\epsilon}} \right] \tag{A.28} \\
&\quad + \frac{\sqrt{\pi}}{S_0} Q^2 \sum_{\boldsymbol{G} \neq 0} \left[\sum_{i \in L_1} \exp\left(\imath \boldsymbol{G} \cdot \boldsymbol{s}_i\right) \right] \left[\sum_{j \in L_2} \exp\left(-\imath \boldsymbol{G} \cdot \boldsymbol{s}_j\right) \right] \lim_{\epsilon \to 0} \int_\epsilon^\infty \exp\left(-h^2 t\right) \exp\left(-\frac{G^2}{4t}\right) \frac{dt}{t^{3/2}} \\
&\quad + Q^2 \sum_{i \in L_1} \sum_{j \in L_2} \sum_{\boldsymbol{R}} \frac{1}{r} \mathrm{erfc}\left(\alpha r\right) \\
&= \frac{2\sqrt{\pi}}{S_0} N_1 N_2 Q^2 \left[-\sqrt{\pi} h \mathrm{erf}\left(\alpha h\right) - \frac{1}{\alpha} \exp\left(-\alpha^2 h^2\right) + \lim_{\epsilon \to 0} \frac{1}{\sqrt{\epsilon}} \right] \tag{A.29} \\
&\quad + \frac{\sqrt{\pi}}{S_0} Q^2 \sum_{\boldsymbol{G} \neq 0} \left[\sum_{i \in L_1} \exp\left(\imath \boldsymbol{G} \cdot \boldsymbol{s}_i\right) \right] \left[\sum_{j \in L_2} \exp\left(-\imath \boldsymbol{G} \cdot \boldsymbol{s}_j\right) \right] \frac{\sqrt{\pi}}{G} F\left(G, \alpha, h\right) \\
&\quad + Q^2 \sum_{i \in L_1} \sum_{j \in L_2} \sum_{\boldsymbol{R}} \frac{1}{r} \mathrm{erfc}\left(\alpha r\right),
\end{aligned}
$$

where we define

$$
F\left(G, \alpha, h\right) = \exp\left(-Gh\right) \mathrm{erfc}\left(\frac{G}{2\alpha} - \alpha h\right) + \exp\left(Gh\right) \mathrm{erfc}\left(\frac{G}{2\alpha} + \alpha h\right). \tag{A.30}
$$

We now collect all terms as described in the beginning of the section and sort them into real space contributions, reciprocal space contributions, constant contributions, and divergent terms. We can simplify the real space summation to

$$
E^{(r)} = \frac{1}{2} Q^2 \sum_{i=1}^N \sum_{j=1}^N \sideset{}{'}\sum_{\boldsymbol{R}} \frac{1}{r} \mathrm{erfc}\left(\alpha r\right). \tag{A.31}
$$

The reciprocal space contribution can be simplified to

$$
E^{(k)} = \frac{\pi}{S_0} Q^2 \sum_{\boldsymbol{G} \neq 0} \sum_{i=1}^N \sum_{j=1}^N \exp\left(\imath \boldsymbol{G} \cdot \boldsymbol{s}_i\right) \exp\left(-\imath \boldsymbol{G} \cdot \boldsymbol{s}_j\right) \frac{1}{G} F\left(G, \alpha, h\right) \tag{A.32}
$$

and the constant contributions to

$$E^{(c)} = -\frac{\sqrt{\pi}}{\alpha S_0} Q^2 \left(N_1^2 + N_2^2\right) - \frac{\alpha}{\sqrt{\pi}} Q^2 N \tag{A.33}$$
$$-\frac{2\pi h}{S_0} \left(\sigma_2 S_0 N_1 Q + \sigma_1 S_0 N_2 Q + \sigma_1 \sigma_2 S_0^2\right)$$
$$-\frac{2\pi h}{S_0} N_1 N_2 Q^2 \left[\mathrm{herf}\left(\alpha h\right) + \frac{1}{\sqrt{\pi}\alpha} \exp\left(-\alpha^2 h^2\right)\right].$$

Finally, the divergent terms add up to

$$E^{(\mathrm{div})} = \frac{\sqrt{\pi}}{S_0} \left[2\sigma_1 S_0 N_1 Q + \sigma_1^2 S_0^2 + N_1^2 Q^2 + 2\sigma_2 S_0 N_2 Q + \sigma_2^2 S_0^2 + N_2^2 Q^2 \right. \tag{A.34}$$
$$+2\sigma_1\sigma_2 S_0^2 + 2\sigma_2 S_0 N_1 Q + 2\sigma_1 S_0 N_2 Q$$
$$\left. +2N_1 N_2 Q^2\right] \lim_{\epsilon \to 0} \frac{1}{\sqrt{\epsilon}}$$
$$= \frac{\sqrt{\pi}}{S_0} \left[S_0\left(\sigma_1 + \sigma_2\right) + Q\left(N_1 + N_2\right)\right]^2 \lim_{\epsilon \to 0} \frac{1}{\sqrt{\epsilon}} \tag{A.35}$$
$$= (0) \lim_{\epsilon \to 0} \frac{1}{\sqrt{\epsilon}}, \tag{A.36}$$

i.e., the energy calculation converges as long as global electro-neutrality $S_0\left(\sigma_1 + \sigma_2\right) + Q\left(N_1 + N_2\right)$ is maintained.

A.1.3. Comments and numerical details

Most terms in the Ewald summation for the bilayer system are very similar to the ones obtained in the planar case. However, we would like to point out a significant difference in the reciprocal space terms: in contrast to the intra-layer terms, the double sum in the inter-layer term can not immediately be factorized into two single sums. However, since particles are located either in the first or the second layer, we can still split the double sum into three factorized single sums such that $|z_{ij}| = 0, h$

$$E^{(k)} = \frac{\pi}{S_0} Q^2 \sum_{\boldsymbol{G} \neq 0} \frac{1}{G} \left\{ \left[\sum_{i \in L_1}^{N} \exp\left(\imath \boldsymbol{G} \cdot \boldsymbol{s}_i\right)\right] \left[\sum_{j \in L_1}^{N} \exp\left(-\imath \boldsymbol{G} \cdot \boldsymbol{s}_j\right)\right] \mathrm{erfc}\left(\frac{G}{2\alpha}\right) \right. \tag{A.37}$$
$$+ \left[\sum_{i \in L_2}^{N} \exp\left(\imath \boldsymbol{G} \cdot \boldsymbol{s}_i\right)\right] \left[\sum_{j \in L_2}^{N} \exp\left(-\imath \boldsymbol{G} \cdot \boldsymbol{s}_j\right)\right] \mathrm{erfc}\left(\frac{G}{2\alpha}\right)$$
$$+ \left[\sum_{i \in L_1}^{N} \exp\left(\imath \boldsymbol{G} \cdot \boldsymbol{s}_i\right)\right] \left[\sum_{j \in L_2}^{N} \exp\left(-\imath \boldsymbol{G} \cdot \boldsymbol{s}_j\right)\right] F\left(G, \alpha, h\right)$$
$$+ \left. \left[\sum_{i \in L_2}^{N} \exp\left(\imath \boldsymbol{G} \cdot \boldsymbol{s}_i\right)\right] \left[\sum_{j \in L_1}^{N} \exp\left(-\imath \boldsymbol{G} \cdot \boldsymbol{s}_j\right)\right] F\left(G, \alpha, h\right) \right\}.$$

This is only easily doable because we have two possible values for the vertical position. At finite temperature, charges may also detach from the layers, thus their vertical position becomes continuous. The increased computational effort required by the double sum can become prohibitive for even medium sized systems.

A.2. Curriculum Vitae

Personal details

Name	Moritz Antlanger
Date of birth:	11 May 1987
Place of birth:	Linz, Austria
Nationality:	Austrian

Education

1993-1997	Primary school	Volksschule 14, Linz
1997-2005	High school	Akademisches Gymnasium, Linz
6/2005	Graduation with distinction	
2005-2006	Community service (alternative to military service)	Caritas of the Diocese Linz
2006-2010	Bachelor's studies in Technical Physics	Vienna University of Technology
4/2010	Graduation with distinction	
2010-2012	Master's studies in Technical Physics	Vienna University of Technology
6/2012	Graduation with distinction	
2012-2015	PhD studies in Physics (as part of a joint supervision)	Vienna University of Technology and Université Paris-Sud 11

Scientific publications

- *On the stability of Archimedean tilings formed by patchy particles* MA, G. Doppelbauer, and G. Kahl. Journal of Physics: Condensed Matter **23**:404206 (2011)
- *$Pt_3Zr(0001)$: A substrate for growing well-ordered ultrathin zirconia films by oxidation* MA, W. Mayer-Schmölzer, J. Pavelec, F. Mittendorfer, J. Redinger, P. Varga, U. Diebold, and M. Schmid. Physical Review B **86**:035451 (2012)
- *Wigner crystals for a planar, equimolar binary mixture of classical, charged particles* MA and G. Kahl. Condensed Matter Physics **16**:43501 (2013)
- *Crystal phases of soft spheres systems in a slab geometry* MA, G. Doppelbauer, M. Mazars, and G. Kahl. Journal of Chemical Physics **140**:044507 (2014)
- *Taking one charge off a two-dimensional Wigner crystal* MA, M. Mazars, L. Šamaj, G. Kahl, and E. Trizac. Molecular Physics **112**:1336 (2014)
- *The rich polymorphic behaviour of Wigner bilayers (working title)* MA, M. Mazars, L. Šamaj, G. Kahl, and E. Trizac. (in preparation)
- *Structures formed by two-dimensional ellipsoids with embedded linear quadrupole moment (working title)* T. Heinemann, MA, M. Mazars, G. Kahl, and S. Klapp. (in preparation)

Ce que nous connaissons est peu de chose,
ce que nous ignorons est immense.
Pierre-Simon Laplace